Optimization of MBE growth of a high quality 2-Dimensional Electron Gas in InAs/AlGaSb material system for pursuing a top-down approach towards realization of topological qubits

by

Ahmed Elbaroudy

A thesis
presented to the University of Waterloo
in fulfillment of the
the thesis requirement for the degree of
Master of Science
in
Physics (Nanotechnology)

Waterloo, Ontario, Canada, 2020

Author's Declaration

I hereby declare that I am the sole author of this thesis. This is a true copy of the thesis, including any required final revisions, as accepted by my examiners.

I understand that my thesis may be made electronically available to the public.

Abstract

Two-dimensional electron gas (2DEG) in InAs quantum wells grown on nearly lattice-matched GaSb substrates is an ideal platform towards the realization of topological quantum computing with Majorana fermions, due to its low effective mass, high mobility, strong spin-orbit coupling, and high Landé g factor. Sufficient electrical isolation from the substrate, high mobility (to ensure ballistic transport), and full depletion of the 2DEG using lithographic gates are the three key parameters for successful mesoscopic quantum transport experiments. However, these properties of 2DEG in InAs quantum wells on GaSb substrates are still elusive. A material with high charge carrier mobility is needed to favor the formation of Majorana Zero Modes (MZMs). Improving growth techniques and structure designs of InAs quantum wells can enhance their electron mobility. In this thesis, we study the Molecular Beam Epitaxy (MBE) growth of InAs/$Al_xGa_{1-x}Sb$ semiconductor heterostructures on undoped GaSb substrates with lattice-matched quaternary buffer ($Al_xGa_{1-x}As_ySb_{1-y}$), which ensured sufficient isolation from the substrate. This structure design is practically free of any threading dislocations, and exhibits very high electron mobilities. The quaternary buffer layer is investigated in terms of crystal structure using X-Ray Diffraction (XRD), and its influence on the electron mobility of overgrown quantum wells. We found that quaternary buffer with As mole fraction not equal or very close to 7% grown on GaSb substrates has a significant influence on carrier mobility inside the quantum well. A growth method for the quaternary buffer was developed to achieve the reproducibility of As composition in that buffer. Fabrication of the resulting heterostructures was carried out. The electrical properties of 2DEGs were investigated using magneto-transport measurements including quantum Hall effect and Shubnikov de-Haas oscillations.

Acknowledgements

First, I would like to thank my supervisor Prof. Zbig Wasilewski, whose unwavering support, eagerness enthusiasm, and encouragement to pursue my career and give my best effort.Thank you for being a wonderful mentor, and for guiding me to be a good researcher. Your constant enthusiasm for new ideas has shown me some of the most enjoyable aspects of research.

I would like to thank Prof. Dayan Ban and Prof. Jan Kycia for reviewing my thesis. The time you spent to read and revise my thesis is greatly appreciated.

I would like to thank Peyton Shi, who helped and guided me to learn everything about Molecular Beam Epitaxy and X-ray Diffraction techniques.

I would like to thank Emma Bergeron, who helped and guided me to learn different fabrication techniques in the cleanroom.

Finally, I would like to thank all the people who made this thesis possible.

Table of Contents

List of Figures

List of Tables

Chapter 1

Introduction

Quantum computing has gained much attention in recent years for its ability to utilize quantum mechanics to carry out data operations that were done inefficiently using classical computers. The quantum version of the classical bit is called the qubit, which is the building block of quantum information. Scientists still face many challenges in the physical realization of a quantum computer. An ideal qubit system suitable for a quantum computer should allow both easy coupling between qubits and strong decoupling of qubits from noise and dissipation. Nearly all of the proposed qubit systems can offer only one of these two attributes, such as ion trap qubits that can provide excellent coherence but are tricky to couple with one another [53] and semiconductor quantum dots that are very easy to couple to each other but also much more subject to decoherence [73].

An alternative approach to overcome this quandary is to develop a topological qubit. Topological degeneracy is defined as the discrete degeneracy of the ground state of a gapped infinitely large many-body system, separating the ground state from the excited states in a non-local manner, such that any local perturbations cannot lift this degeneracy. The ground states in such a system will show the non-Abelian geometric phase (and therefore non-Abelian exchange statistics), which can transform a ground state to a degenerate counterpart in a so-called topological operation. Topological quantum computing is restricted to the manifold of such ground states [50]. As an example, topological degeneracy can appear in defects or vortex cores in $p + ip$ superconductors [28]. If the degeneracy is two-fold and enumerated by fermion parity, then the ground states show Majorana exchange statistics [50], and the system hosts the so-called "Majorana Zero-Mode" (MZM) quasiparticle. If a large number of localized MZMs were realized in a system where it is easy to couple them to each other, this system will acquire an extensive ground-state degeneracy and be protected against decoherence. By utilizing this phenomenon, topological qubits are

protected against local decoherence, allowing topological quantum computation. Thus, it could become the ideal qubit system for a quantum computer. This thesis aims to develop material foundations to build a suitable platform for realizing such topological qubits.

Two-dimensional electron gases (top-down approach) and self-assembled nanowires (bottom-up approach) are the two major platforms for realizing topological qubits within semiconductor material systems. So far, there is no complete experimental proof of realizing MZMs. However, there is strong evidence of their existence [44]. The upcoming step for progress in this field includes the fabrication of sophisticated devices capable of quasiparticle braiding or fusion, which is difficult to be achieved with self-assembled nanowires but should be considerably easier with two-dimensional electron gases (2DEGs) in semiconductor wafers. A material with high charge carrier mobility is needed to favor the formation of MZMs as the mobility of charge carriers in 2DEGs is much higher than in self-assembled nanowires of the same material system. Additionally, when scaling up the number of topological qubits is considered, even in a small scale quantum computer (50-100 logical qubits), the case for pursuing a top-down approach towards realization topological qubits becomes compelling.

InAs has low effective mass, high carrier mobility, strong spin-orbit coupling, and high Landé g factor, making it one of the promising materials for the realization of topological qubits. Our target is to grow a high-quality 2DEG in InAs/AlGaSb materials system with no misfit dislocations on an undoped GaSb substrate using Molecular Beam Epitaxy (MBE). Thus, trying to eliminate scattering by threading dislocations, a robust scattering mechanism, within the quantum well. 2DEGs utilizing a simple GaSb buffer layer have successfully achieved high mobility. However, they don't have sufficient isolation from the GaSb substrate [70]. A quaternary alloy ($Al_xGa_{1-x}As_ySb_{1-y}$) with higher-band-gap is used as a buffer layer that can be lattice-matched to the GaSb substrate by accurate adjustment of its materials compositions. Sufficient isolation from the GaSb substrate has been achieved by using such a quaternary buffer. Growing a lattice-matched quaternary buffer is challenging due to the incorporation competition of group V atoms (As and Sb) on the surface, which strongly depends on growth conditions. The MBE growth of this material system and magnetotransport measurements on the resulting heterostructures are the subjects of this thesis.

The thesis is structured to describe these heterostructures' growth and measurements in separate chapters, but their development took place concurrently. In the chapter after this introduction, the theory of epitaxial crystal growth, electron behavior in crystals, and the employed semiconductors are covered. The third chapter details the experimental setup, with the molecular beam epitaxy system playing the central part along with characterization and measurement methods. Chapter four focuses on material growth and a full

description of the 2DEG system in InAs material. Experimental results of X-ray diffraction are presented starting from the fifth chapter, which investigates the buffer layer of different samples and describes their crystal parameters. The Hall bar design and cleanroom fabrication is the subject of chapter six. Chapter seven includes the magnetotransport data, and Hall measurements with the interpretation of the results obtained.

Chapter 2

Theory

A brief review of the theoretical foundations for the experimental chapters is presented here. This chapter does not contain a complete account of all the subjects involved but focuses on the topics necessary to attain a general understanding of the applied methods and the necessary knowledge to interpret the obtained measurements and results.

2.1 Crystals

The arrangement of atoms in a solid plays an essential role in defining its physical properties. According to the arrangement of atoms in a solid, it can be classified into crystalline, poly-crystalline or amorphous structure. Crystallography is the scientific process of studying the order of atoms in a crystal, and crystallization is the process of growing these crystal structures. When the atoms have a periodic arrangement in a solid, it is defined as a crystal. Crystal structures are characterized by a unit cell which is composed of one or more atoms in a specific spatial arrangement. Poly-crystal is composed of crystallites or grains which internally have periodic arrangement of atoms, but these crystallites are not in an ordered pattern. The amorphous structure is characteristic of glasses, where the atoms have no periodic arrangement [5].

2.1.1 Crystal lattices

Crystal lattices are the positions at which the atoms of a crystal are found, and a few vectors can define these positions due to the periodic arrangement of the atoms. For

example, the three vectors

$$\vec{a} = a\begin{pmatrix}1\\0\\0\end{pmatrix} = a\hat{i}; \qquad \vec{b} = b\begin{pmatrix}0\\1\\0\end{pmatrix} = b\hat{j}; \qquad \vec{c} = c\begin{pmatrix}0\\0\\1\end{pmatrix} = c\hat{k}, \tag{2.1}$$

are used for describing all lattice sites. Here "a" is the interatomic distance, also known as lattice constant. Any lattice site can be found by applying one of the lattice vectors to another lattice site. The primitive vectors $(\vec{a}, \vec{b}, \vec{c})$ can be used to describe a complete lattice; they do not have to be orthogonal or equal in length. Hence, there are three more angle parameters (α, β, γ) between these three vectors. These six parameters are called lattice constants or lattice parameters because they describe the complete lattice [34]. A unit cell of the lattice can be defined by the three vectors ($\vec{a}$, $\vec{b}$, $\vec{c}$), which form the parallelepiped shown in figure 2.1. By repeating this unit cell, the whole crystal can be constructed in all three dimensions.

2.1.2 The Bravais lattices

Simple cubic lattice is the simplest case, where the lattice is described by three vectors of equal length ($a = b = c$) orthogonal to each other ($\alpha = \beta = \gamma = 90°$). Each of the eight corners of the simple cubic lattice has one lattice site, and the atoms at each corner of the lattice are shared with seven adjacent cells. Thus, the number of atoms per unit cell in this crystal is one atom ($N = \frac{8}{8} = 1$), and this unit cell has one lattice site for the simple cubic lattice. Body-centered cubic (BCC) is another type of cubic lattices, where its unit cell has more than one lattice site. This additional lattice site is at the center of the unit cell. This lattice has two lattice sites, one at the corners and one at the unit cell center. The number of lattice sites or atoms in the unit cell of a BCC crystal is also two ($N = \frac{8}{8} + 1 = 2$). The third type of cubic lattice is a face-centered cubic (FCC), where its unit cell has additional lattice sites at the centers of the six faces of the unit cell. Each of these sites is shared with one adjacent unit cell; therefore, the total number of lattice sites in FCC is 4 ($N = \frac{8}{8} + \frac{6}{2} = 4$). The crystal structure of these three cubic lattice crystals is shown in figure 2.1. Hence, all the information needed to construct a lattice is the unit cell and the lattice vectors [34].

There are seven types of crystal systems that can be constructed concerning the six parameters (a, b, c) and (α, β, γ). If the three vectors are orthogonal ($\alpha = \beta = \gamma = 90°$) but one of them has different length from the others ($a = b \neq c$), this lattice is called Tetragonal lattice crystal. In the case that the three vectors are not equal ($a \neq b \neq c$) but

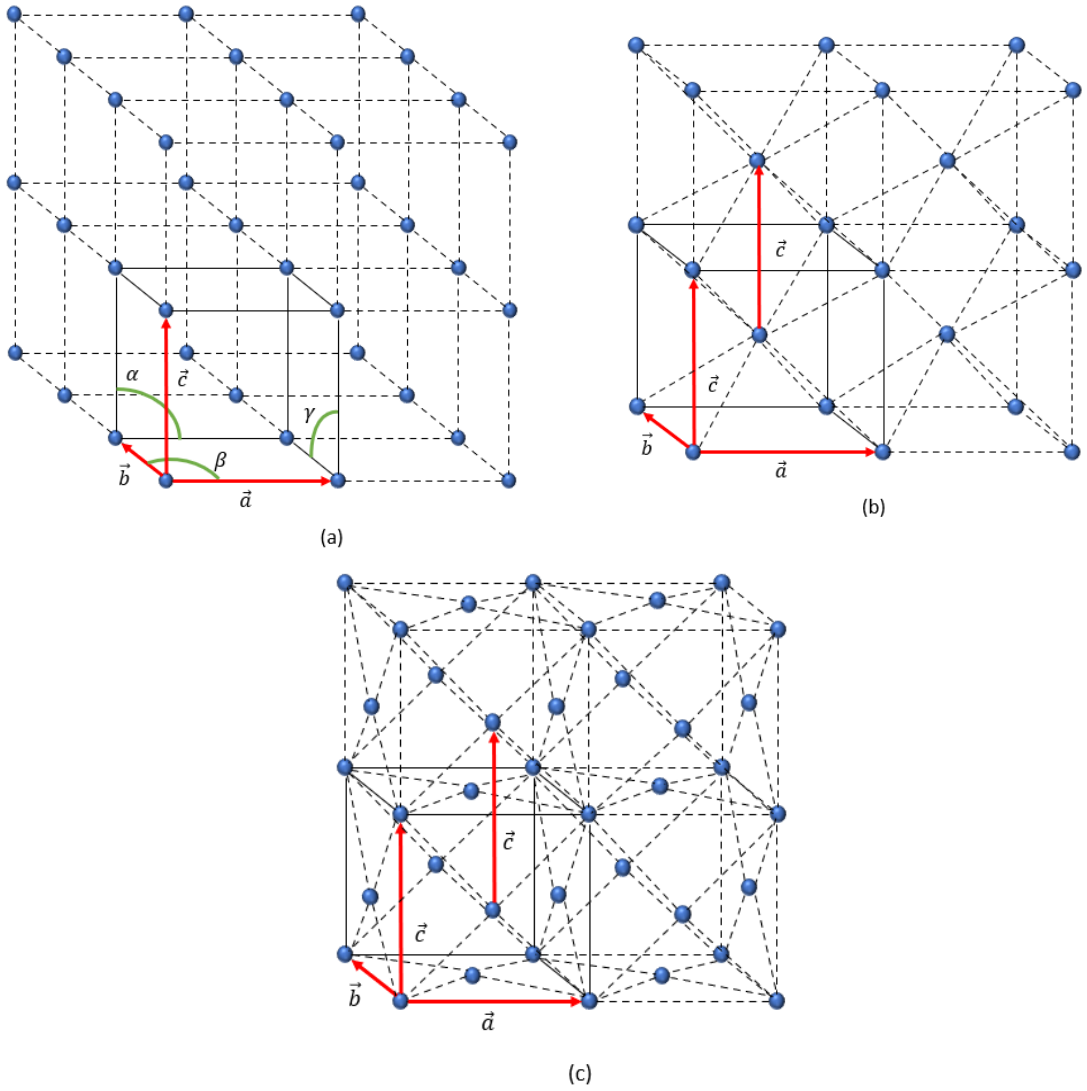

Figure 2.1: This figure shows (a) a simple cubic lattice, (b) a body centered cubic (BCC) lattice and (c) a face centered cubic (FCC) lattice. Any lattice site can be found by applying applying one of the lattice vectors to another lattice site.

are orthogonal to each other the lattice is called Orthorhombic lattice crystal. When the angles are different, three more crystal systems can be constructed. The first one is called Rhombohedral lattice structure, where the three lattice vectors are of the same length ($a = b = c$) and the angles are equal but not orthogonal ($\alpha = \beta = \gamma \neq 90°$). The second

one is a monoclinic lattice structure, where the vectors are equal in length but one of the angles only is not equal to 90° ($\alpha \neq 90°$, $\beta = \gamma = 90°$). If the lattice has different lengths and different angles not equal to 90° ($a \neq b \neq c$) and ($\alpha \neq \beta \neq \gamma \neq 90°$), it is called Triclinic. Finally, the last Bravias lattice is the hexagonal lattice, where ($\alpha = \beta = 90°$ and $\gamma = 120°$) and it has two different lattice parameters ($a = b \neq c$). The body-centered, face-centered, and base-centered modifications are found in these seven crystals, giving 14 different lattices called the 14 Bravais lattices. In 1850, the french crystallographer Auguste Bravais described these 14 point lattices, since then called Bravais lattices [12] [13].

2.1.3 Planes and directions in crystals

To describe a specific set of planes in a lattice, the points at which the plane intercepts the axes of the unit cell are obtained by Miller Indices, which are shown in figure 2.2a. Miller indices were introduced by the British mineralogist William Hallowes Miller in 1839 [47]. The plane's intercepts with the unit cell in the example shown in figure 2.2 are 1/4 with the x-axis, 1/2 with the y-axis, and 1 with the z-axis. The Miller indices of a plane must be integers. Therefore, we will multiple these intercepts by 4 to get the smallest integer values which are

$$\begin{aligned} h &= 4 \times \frac{1}{4} = 1 \\ k &= 4 \times \frac{1}{2} = 2 \\ l &= 4 \times 1 = 4 \end{aligned} \tag{2.2}$$

These values are called the Miller indices and demonstrated by these parentheses (hkl). Therefore, the Miller indices, for the example which is shown in figure 2.2, are (124). A bar above the number will be used as an indication of a negative index, for example, $(\bar{1}\bar{2}4)$. In case the plane is parallel to one of the crystal axes, the corresponding Miller index is zero, as the intercept will be at infinity. Due to the symmetry of the lattice, some of the planes are equivalent in a crystal. For example, the (100), (010), (001), $(\bar{1}00)$, $(0\bar{1}0)$ and $(00\bar{1})$ in a simple cubic lattice are indistinguishable and denoted as {100} family of planes. The directions are defined by following the same method used for planes in the crystal. The square brackets $[hkl]$ are used to define the Miller indices directions, which are orthogonal to the (hkl) planes, as shown in figure 2.2. The angle brackets denote the family of Miller indices directions as $< hkl >$.

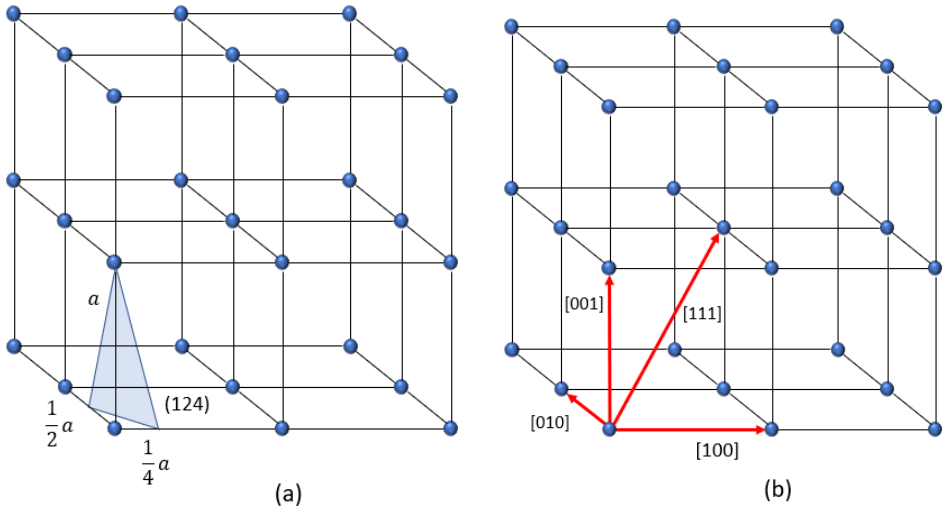

Figure 2.2: Miller indices of a plane and directions. (a) shows the derivation of Miller indices of a plane from the plane intercepts with the unit cell axes. (b) shows the derivation of different Miller indices directions.

It is crucial to distinguish directions and planes in a crystal as the physical properties of a crystal can be strongly anisotropic. The simple cubic lattice (100), (110) and (111) planes are shown in figure 2.3. For the planes shown in the figure, it is obvious that each of them may exhibit different properties, as the configuration of the atoms on these planes is fairly different. Each plane has certain lattice intercepts at regular intervals when it goes through the crystal lattice origin. As described in figure 2.3, it is considered that the lattice extends to infinity. Thus, there is a set of parallel planes to the original one, which

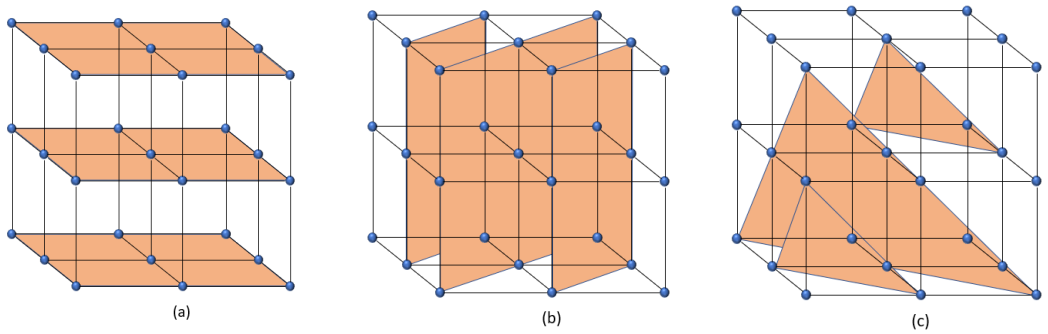

Figure 2.3: Planes (100), (110) and (111) in a simple cubic lattice.

is indistinguishable from each other.

2.2 Epitaxial Crystal Growth

The deposition of a crystalline layer on a crystalline substrate is known as Epitaxy, which means "ordering above". When the layer is deposited on a substrate that has the same crystal material, this process is called homo-epitaxy. In case the layer has different crystal material from the substrate, the process is called hetero-epitaxy. The epitaxial crystal growth can take place either close to thermodynamic equilibrium or away from it. In the latter case, the process is kinetically limited. The molecular beam epitaxy growth is mainly determined by kinetic processes. These processes can be visualized by a Kossel crystal model. The crystal is assumed to be formed from cubes stacked directly on top of and along with each other, with a terrace-step-kink (TSK) model at its foundation [76]. The bond strength of an atom to a crystal can be determined from the number of atoms surrounding it at its position. Different mechanisms can occur during the growth process, which can be seen in figure 2.4. The first mechanism is adsorption; an atom is adsorbed when it impinges on the surface, then it can diffuse along the surface. The kink site of a surface step is a site where an atom can bond on three sides. This is shown during incorporation process in figure 2.4. The Kink site is an important position because it is readily accessible and offers the strongest bonding location at surface terraces. The

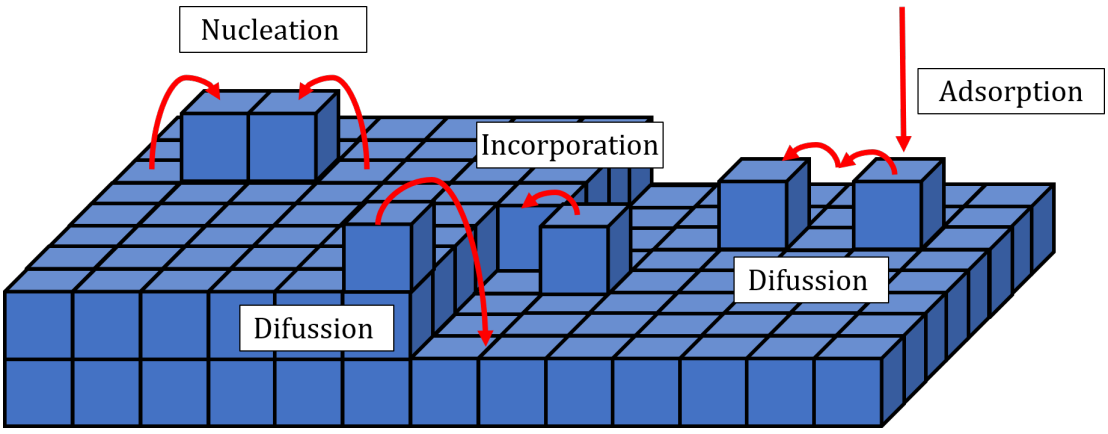

Figure 2.4: Schematic of different epitaxial growth mechanisms. Nucleation of several atoms, Impinging atom adsorption, Kink site Incorporation and diffusion on and across the surface.

substrates used for epitaxial growth can initially have surface steps which result from unintentional slight surface misorientation away from low-index crystal plane.

The growth model is referred to as step-flow growth when governed by an advancing series of surface steps. This growth model is similar to the ideal layer-by-layer Frank-Van der Merve growth mode. However, the growth can be hindered in case when the nucleation happened away from the kink sites. For screw dislocations outcrop on a crystal surface, the growth will proceed in a spiral mode around these dislocations. Volmer-Weber growth is another growth mode where atoms initially aggregate into multi-layer islands, which merge as they grow in size. It is the dominant growth mode for materials with high lattice mismatch, low surface mobility of adsorbed atoms, or high surface defect density. High-quality heteroepitaxial layers growth is the basis for the production of quantum well structures in III/V semiconductors. The Hetero-epitaxy of these materials is a very complex process. Some of the issues addressed in this thesis are compositional and strain control, which can be particularly challenging in materials containing more than one group V element, in this case, As and Sb.

2.3 Strain and lattice mismatch

In the case of epitaxial growth on a substrate with a different lattice constant from that of the epitaxial layer, the atoms in the epitaxial layer will try to align with the substrate atoms. Thus, the layer that is grown, and the substrate will have the same in-plane lattice constant. The strain will be induced in the grown layer due to this deformation. The relation between the strain in a cubic crystal structure and applied or resulting stress, known as Hooke's law, is given by [41] [68]:

$$\begin{pmatrix} \sigma_{xx} \\ \sigma_{yy} \\ \sigma_{zz} \\ \sigma_{xy} \\ \sigma_{yz} \\ \sigma_{xz} \end{pmatrix} = \begin{pmatrix} C_{11} & C_{12} & C_{12} & 0 & 0 & 0 \\ C_{12} & C_{11} & C_{12} & 0 & 0 & 0 \\ C_{12} & C_{12} & C_{11} & 0 & 0 & 0 \\ 0 & 0 & 0 & C_{44} & 0 & 0 \\ 0 & 0 & 0 & 0 & C_{44} & 0 \\ 0 & 0 & 0 & 0 & 0 & C_{44} \end{pmatrix} \begin{pmatrix} \epsilon_{xx} \\ \epsilon_{yy} \\ \epsilon_{zz} \\ \epsilon_{xy} \\ \epsilon_{yz} \\ \epsilon_{xz} \end{pmatrix} \tag{2.3}$$

where σ_{ij} are the components of the stress tensor, ϵ_{ij} are the components of the strain tensor, and C_{ij} are the stiffness coefficients of the material under stress. Stiffness coefficients of some III/V semiconductors are given in the table 2.1.

The definition of strain components in the i crystal direction is given by

$$\epsilon_{ii} = \frac{a_i^L - a_0^L}{a_0^L} \tag{2.4}$$

where a_i^L is the strained lattice constant in i direction, and a_0^L is the native, i.e., strain-free, the lattice constant of the layer. When the epitaxial film and its substrate are oriented along [001] direction, biaxial stress applied due to a substrate with the lattice constant a_0^S in the x and y directions will be

$$a_x^L = a_y^L = a_0^S = a_\parallel \longrightarrow \epsilon_{xx,yy} = \epsilon_\parallel = \frac{a_0^S - a_0^L}{a_0^L} \tag{2.5}$$

And Hooke's law will be reduced to

$$\begin{pmatrix} \sigma_\parallel \\ \sigma_{zz} \end{pmatrix} = \begin{pmatrix} C_{11} + C_{12} & C_{12} \\ 2C_{12} & C_{11} \end{pmatrix} \begin{pmatrix} \epsilon_\parallel \\ \epsilon_{zz} \end{pmatrix} \tag{2.6}$$

In this case, the epitaxial layer is free to expand vertically, the stress component in growth direction σ_{zz} is zero and the corresponding strain component ϵ_{zz} is given by

$$\sigma_{zz} = 2C_{12}\epsilon_\parallel + C_{11}\epsilon_{zz} = 0, \qquad where \quad \epsilon_{zz} = \epsilon_\perp = \frac{a_z^L - a_0^L}{a_0^L} \tag{2.7}$$

where a_z^L is the out-of-plane lattice constant of the layer. By the substituting the definitions of $\epsilon_\parallel$ and $\epsilon_\perp$ in the equation of perpendicular stress component σ_{zz} 2.7, the out-of-plane lattice constant of the layer can be calculated from

$$a_z^L = a_\perp = a_0^L - \frac{2C_{12}}{C_{11}}(a_\parallel - a_0^L) \tag{2.8}$$

III/V semiconductors	C_{11}	C_{12}	C_{44}
AlAs	12.02	5.7	5.89
GaAs	11.9	5.34	5.96
InAs	8.3	4.5	4.0
AlSb	8.77	4.08	4.34
InSb	6.67	3.65	3.02
GaSb	8.83	4.02	4.32

Table 2.1: Stiffness coefficients of some III/V semiconductors taken from [3], all values are in 1×10^{10} Pa.

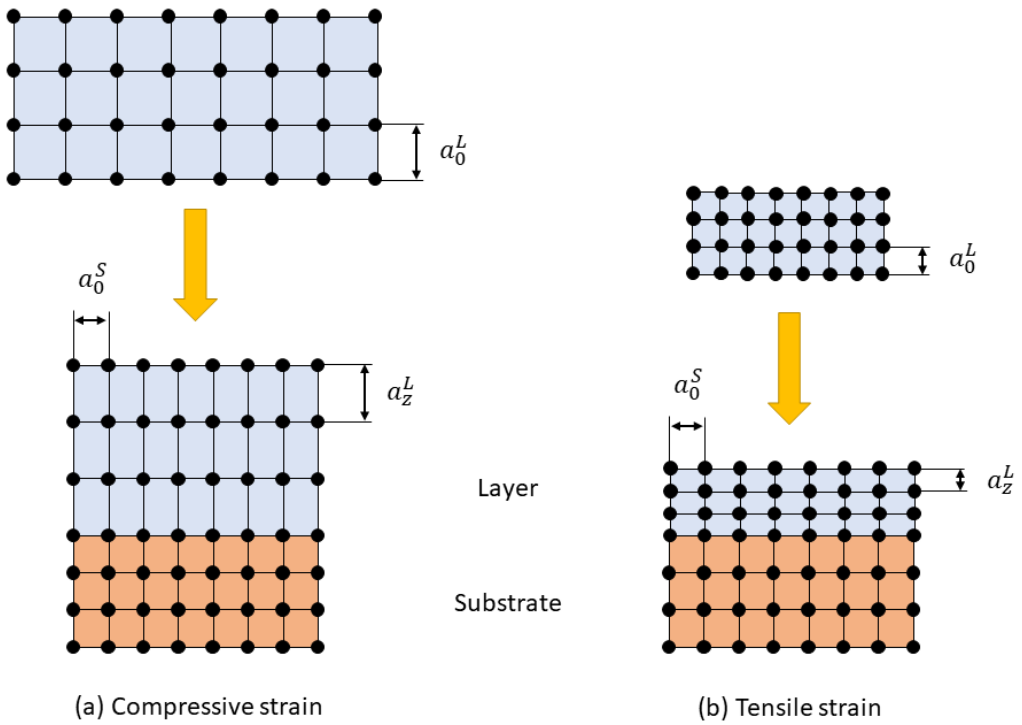

Figure 2.5: The demonstration of compressive and tensile strain. (a) An epitaxial layer with native lattice constant larger than that of the substrate producing compressive strain. (b) An epitaxial layer with native lattice constant smaller than that of the substrate producing tensile strain.

Since $a_x^L = a_y^L \neq a_z^L$, the cubic crystal will be distorted into a tetragonal crystal structure due to the biaxial stress applied to the epitaxial layer as a result of the lattice mismatch with the substrate. Such an epitaxial layer is referred to as pseudomorphic with this type of distortion. The situation is demonstrated in figure 2.5. When an epitaxial layer has a native lattice constant a_0^L larger than the lattice constant a_0^S of the substrate on which the layer was deposited, compressive stress will be induced in the epitaxial layer. Hence, the in-plane lattice constant will be compressed to match the substrate lattice constant while its out-of-plane lattice constant will be extended. On the other hand, if an epitaxial layer with a native lattice constant smaller than that of the substrate on which the layer was deposited, tensile stress will be induced in the epitaxial layer. The opposite situation will

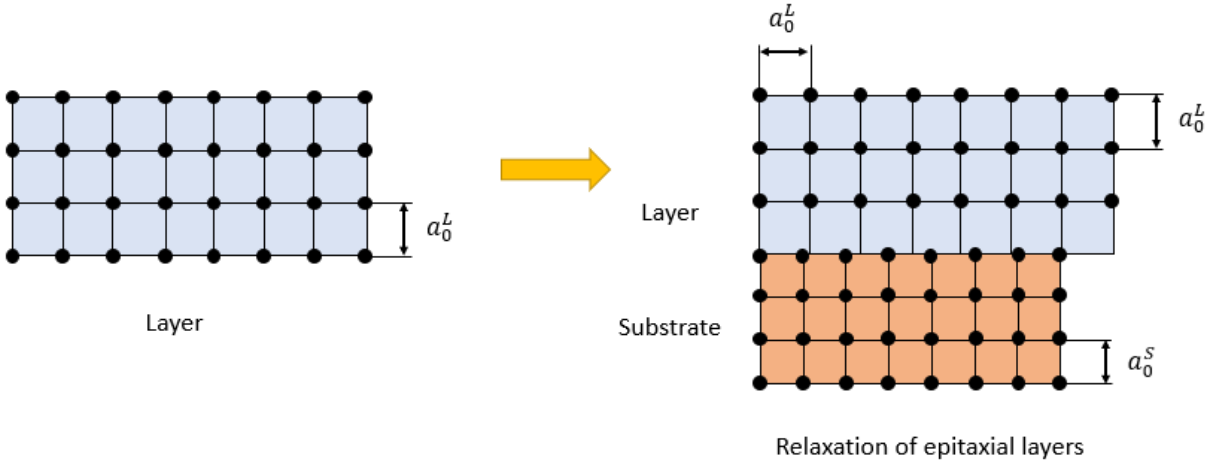

Figure 2.6: Demonstration of relaxed epitaxial layer.

happen, the in-plane lattice constant of the layer will be extended to match the substrate lattice constant, while the out-of-plane lattice constant will be compressed. Therefore, the crystal structure of the epitaxial layer will be distorted into a tetragonal lattice structure due to the strain-induced. In the case of epitaxial layers relaxation, the epitaxial layer lattice constant does not change when deposited on a substrate with a different lattice constant from that of the epitaxial layer, as shown in figure 2.6.

Strain energy will be introduced into the epitaxial layer due to the distortion in the crystal, which is also known as "coherency" energy associated with strain in the epitaxial layer [68]. This strain energy per area is given by

$$u_{coh} = \frac{E}{A} = 2\, h_l\, \mu\, \epsilon_{\parallel}^2\, \frac{1+\nu}{1-\nu} \tag{2.9}$$

where h_l the epitaxial layer thickness, μ is the shear modulus which is defined as the ratio between applied shear stress and shear strain under pure shear, and ν is the Poisson's ratio which is defined as the negative ratio between lateral and longitudinal strains when the structure is under stress along the axis of the unit cell in cubic materials, and it is given by

$$\nu = \frac{C_{12}}{C_{11} + C_{12}} \tag{2.10}$$

After doing some simple calculations by substituting equation 2.10 into equation 2.8, the native lattice constant a_0^L of unstrained material layer can be written as

$$a_0^L = \frac{1-\nu}{1+\nu} a_\perp + \frac{2\nu}{1+\nu} a_\parallel \tag{2.11}$$

These two equations 2.10 and 2.11 are playing an essential role in the upcoming characterization chapter.

For a given lattice mismatch, we can see from equation 2.9 that the areal strain energy density increases linearly with increasing the layer thickness. Therefore, there is a limit to the layer's thickness to avoid the relaxation of this pseudomorphic layer. This thickness limitation is called the critical thickness h_c, which is the thickness at which the strain in the layer starts to relax by forming dislocations. The formation of these dislocations can only occur when the areal strain energy density exceeds the energy needed to form a dislocation. The formation of these dislocations leads to a reduction in the areal strain energy density and plastically relaxes the stress in the layer. The prediction of a pseudomorphic layer relaxation was developed by Matthews and Blakeslee [48]. The paper implies that the critical thickness can be calculated analytically by a transcendent formula. Dislocations in a perfect crystal are formed from perfectly crystalline structure domains but tilted or twisted with respect to each other. The dislocations density in the crystal is characterized by the size of these domains, and crystals known as mosaic. The roughness of a layer increases with increasing the density of dislocations since they are many crystalline regions with slightly different orientations.

The composition of different materials in ternary and quaternary alloys influences the critical thickness. The critical thickness can be strongly reduced if the ideal material composition for lattice matching was not achieved. For example, GaAs and AlAs have small lattice mismatch, $Al_xGa_{1-x}As$ relatively thick layers can be grown for large Al mole fractions. On the other hand, for $Ga_xIn_{1-x}As$, $GaAs_{1-x}Sb_x$ and $AlAs_{1-x}Sb_x$ ternary alloys the compositions have to be accurate to a few tenths of a percent to avoid relaxation of thick structures.

2.4 III/V Semiconductors

Semiconductors have two types, elemental semiconductors, found in the fourth group of the periodic table such as Si, Ge, and Sn. The second type is the compound semiconductors, composed of elements from groups III and V, II and VI, or IV and VI. We focus on compound semiconductors consisting of elements from groups III and V in this work. III/V semiconductors consist of one or more group III elements, like Al, Ga, and In and one or more elements of group V, like N, P, As, Sb, and Bi. III/V semiconductors crystallization

results in a Zinc blende crystal structure or hexagonal crystal structure. InAs and GaSb are examples of the III/V semiconductor materials that crystallize in zinc blende crystal structure. The epitaxial layers will acquire the same crystal structure of the substrates they are grown upon [2]. Zinc blende structure constructed from two face-centered cubic sublattice shifted by one-quarter of its lattice constant in [111] direction. The unit cell of the zinc blende consists of four atoms from each main group III and V. The schematic structure if zinc blende crystal is shown in figure 2.7.

Each sublattice in the zinc blende is specified for elements from one of the two groups. However, for ternary and quaternary alloys, the atom species from the same group can be mixed. The energy bandgap versus lattice constants plus the bandgap type information of some selected III/V semiconductors are shown in figure 2.8. As seen in the figure, the binary alloys are indicated by circles and the lines connecting these binary alloys, which have one common material indicating the ternary alloys. The substrates made from binary alloys are the most common substrates used for epitaxy growth as they are available in high-quality wafers. The bandgap energy and lattice constants of ternary alloys are found from the line connecting their binary alloys. For example, $Al_xGa_{1-x}Sb$ is indicated by the line connecting AlSb and GaSb and $In_xGa_{1-x}As$ is indicated by the line connecting InAs and GaAs. Quaternary alloys are indicated by the shape that is enclosed by these lines connecting binary alloys. These quaternary alloys are composed of the binary alloys found

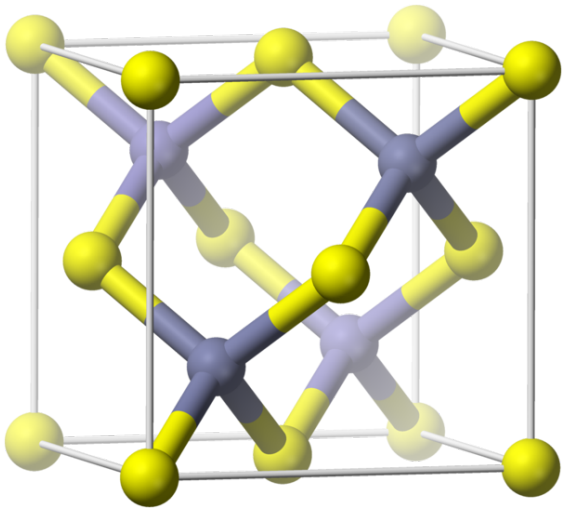

Figure 2.7: The III/V semiconductor zinc blende crystal structure.

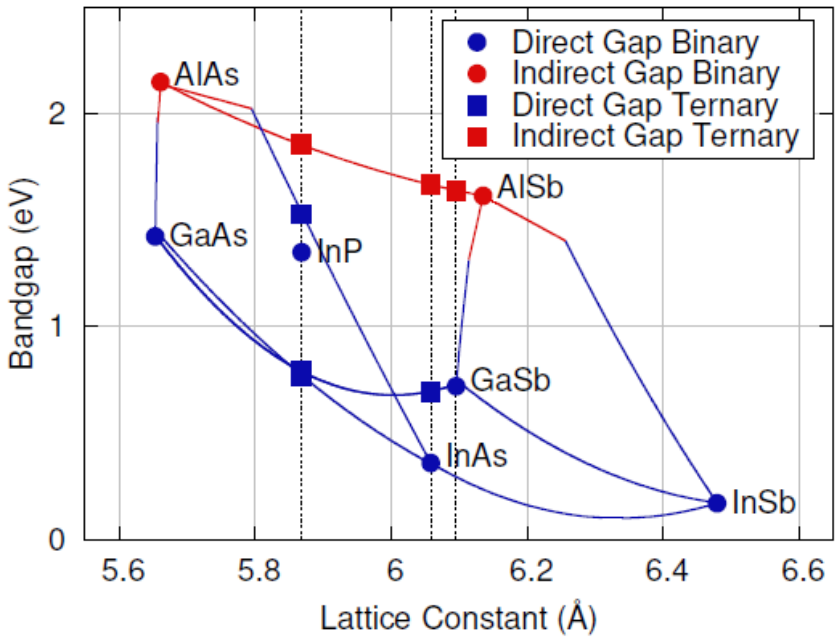

Figure 2.8: Energy Band gap versus lattice constants of some selected III/V semiconductors. Circles indicating Binary alloys. The lines connecting binaries indicating ternary alloys. Faces or shapes which are enclosed by ternary alloys are quaternary alloys [23].

at the corners. For example, $Al_xGa_{1-x}As_ySb_{1-y}$ is formed from the four binary alloys GaSb, AlSb, AlAs, and GaAs. Therefore, the shape enclosed by the four lines connecting these four binary alloys is used to find the energy bandgap and lattice constants of the quaternary alloy $Al_xGa_{1-x}As_ySb_{1-y}$. Vegard's law defines properties of a particular ternary or quaternary alloy by simple linear combinations of the binary alloys involved [18]. The lattice parameters of a specific alloy can be found from Vegard's law by using the chosen mole fraction of each martial in that alloy. When there is a lack of information about an alloy materials system, Vegard's law is a good approximation for deriving alloy's lattice constant. However, not all the compositions obey the linearity rule of Vegard's law; there are some exceptions [3]. Vegard's law for quaternary alloys is discussed in more detail in the upcoming chapters.

2.4.1 Band Structure

Combining and altering crystal lattices in different ways can change the electrons' properties in these crystal lattices. These electrons' features are the building blocks of electronics and exotic quasi-particles for cutting-edge fundamental research. The band structure of the material can describe the energies of these electrons in a solid. The dispersion relation $E_n(\mathbf{K})$ is describing the energies an electron can have for any given wave vector $\mathbf{K}$ in the Brillouin zone for a specific band index n. The electrons obey Schrödinger equation in the case of free-electron approximation as [15]

$$\left[-\frac{\hbar^2}{2m_0}\nabla^2 + V(r)\right]\psi(r) = E\psi(r) \tag{2.12}$$

where m_0 is the electron mass and $V(r)$ the periodic potential energy particular to the crystal, which can be written as $V(r) = V(r + R)$, when it is shifted by vector $\mathbf{R}$ the lattice is reproduced. The motion of electrons in periodic potential within a crystal lattice can be very different from their motion in vacuum, leads to a modified mass of electrons, which is known as effective mass (m^*). In this case, the wave function of electrons can be described as a product of a plane wave and a periodic function with the same periodicity as the crystal, which is known as Bloch's theorem. Therefore, a Bloch wave function for a given $\mathbf{K}$ vector is given by

$$\psi_{\mathbf{K}}(r) = e^{i\mathbf{K}\mathbf{r}}u_{n\mathbf{K}}(r) \tag{2.13}$$

with $u_{n\mathbf{K}}(r) = u_{n\mathbf{K}}(r+\mathbf{R})$, where it is periodic over the the crystal lattice. The whole wave function $\psi_{\mathbf{k}}(r) = \psi_{\mathbf{k}+\mathbf{K}}(r)$ will be periodic in the reciprocal space, where K is a reciprocal lattice point. The energy bands $E_n(K)$ are collectively formed from the multiple eigenvalue solutions of the Schrödinger equation and are classified by the index n. The calculated band structure of InAs semiconductor is shown in figure 2.9 [15]. Band structure determines the energies that electrons could have, but determining whether a particular energy level is occupied with electrons or not, the Fermi level should be used. Fermi level is the energy level where the probability of states being occupied is 50%. For metals at zero kelvin temperature, all energy states below the Fermi level are filled with electrons, while the states above it are empty. In contrast, the Fermi level in semiconductors is found in the energy gap between the conduction and valence bands, where there are no states. An energy band has a limited number of electrons due to the Pauli exclusion principle and the finite density of states.

Energy gaps are ranges of energy with no density of states, and they have no solutions of Schrödinger equation. The conductivity of a specific material is controlled by these energy gaps. Suppose a particular material has a band with free states where the electron occupation could be rearranged, the electrical conductivity can occur by applying an electric field. When the Fermi level at equilibrium in an energy band where the charge transport is allowed, it indicates a metallic conductance. In an insulator, the Fermi level is inside a large bandgap, typically much more than one electron volts away from both conduction and valence bands. For a semiconductor, which is the scope of our work, the energy gap is moderate, where thermally excited electrons can occupy the states above the bandgap, and the material starts to conduct. In semiconductors, the conduction band, which is the band above the energy gap, contains a few electrons, and the valence band, which is the band below the energy gap, contains a few electrons missing leaving free states to conduct. These missing electrons are denoted with positive electric charge and are called holes.

The ability to control the conductivity in semiconductors is a crucial feature for many

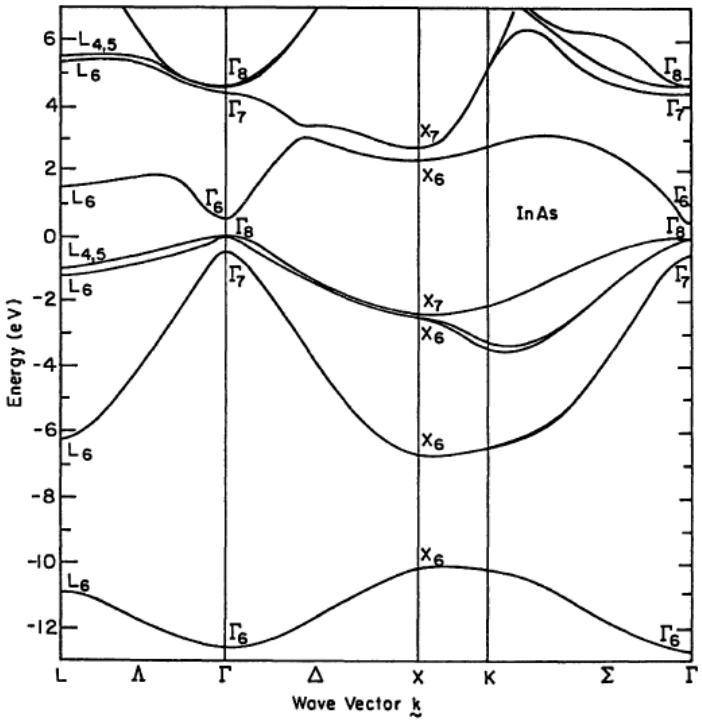

Figure 2.9: InAs Band structure reprinted from Cohen and Chelikowsky[15]. The point k=0 is determined by Γ and the zero energy is defined by the valence band maximum.

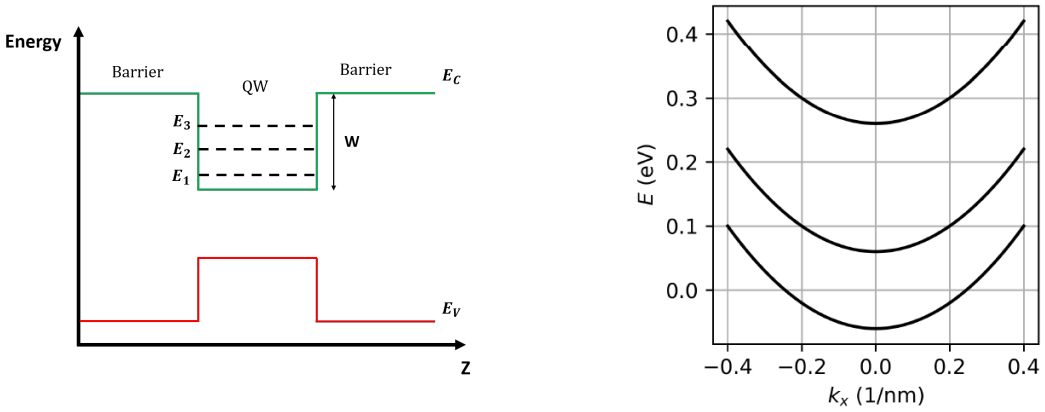

Figure 2.10: Left: A quantum well schematic built by sandwiching the quantum well between two semiconductors with larger band gaps. The conduction and valence bands are denoted by E_C and E_V, respectively. W is the band offset and E_1, E_2 and E_3 are some electron subbands at k=0. Right: Shows electron dispersion in a quantum well split into subbands according to Equation 2.15. Retrieved from [57]

applications and research interests. Controlling of the conductivity in semiconductors takes place by gating with electric fields or by doping. Doping introduces electronic states close to the conduction band (donors) or close to the valence band (acceptors) within the forbidden gap and shifting the Fermi level accordingly. These states would be populated by electrons (donors) or holes (acceptors) at very low temperatures, but the carriers will be released into the bands upon increasing the temperature. When semiconductor materials with different wave functions are in contact, the charge carriers will redistribute due to the work function difference. The charge carriers transfer will continue until the Fermi levels of semiconductors are aligned. This alignment of the relative energetic position of bands in different layers will result in band bending close to the interfaces and may lead to useful electronic properties.

2.4.2 Two-Dimensional Systems

Now the topic is broadened to the band structure of various materials combined as a heterostructure instead of the band structure of a single material. In this thesis, we are investigating two-dimensional systems of electrons called two-dimensional electron gas (2DEG). The electronic devices based on 2DEGs are considered one of the most significant developments in the semiconductors field. In these devices, the motion of the electrons is limited

to two dimensions and confined in a potential well. Quantum wells are a special case of these structures which are formed from heterostructures. A quantum well is constructed by a semiconductor layer sandwiched between two layers of semiconductors with a larger energy band gap, as shown in figure 2.10. The surrounding semiconductors provide the electron confinement in the vertical direction while allowing free movement in the 2D plane of the well.

As a result of this quantum confinement, the conduction and valence bands split into subbands, as shown in figure 2.10. If a quantum well of a specific material has a parabolic dispersion with nearly infinite barriers, the energies of such subbands can be written as

$$E(k_{xy}) = E_n + \frac{\hbar^2 k_{xy}^2}{2m^*} \tag{2.14}$$

where m^* is the effective mass of the quantum well material. The second term in the summation describes the energy of motion in xy-plane. E_n is the subband energy with index n and given by [15]

$$E_n = \frac{\hbar^2}{2m^*}\left(\frac{n\pi}{L}\right)^2 \tag{2.15}$$

where L is the thickness of the quantum well. From this formula, it is obvious that as the quantum well gets wider, the spacing between the subbands decreases. In reality, the wave functions of the confined charge carriers can penetrate the barriers with different effective masses as the potential barriers are not infinitely high.

Chapter 3

Experimental Setup

3.1 Molecular Beam Epitaxy

Epitaxial growth of semiconductors, metals, or oxides thin films on a particular substrate is performed by Molecular Beam Epitaxy (MBE) technique. MBE is a highly sophisticated physical vapour deposition technique, where crystal growth is carried out under kinetically limited conditions far from thermal equilibrium. The growth is performed by directing molecular beams onto a heated substrate surface. In 1966, the first known crystal growth using molecular beams of silicon was performed by Joyce and Bradley [36]. In MBE, the crystal growth occurs in the Ultra High Vacuum (UHV) environment to ensure that the unwanted impurity atoms' arrival rate from the vacuum ambient is negligible compared with that from the molecular beams. Besides, UHV-compatible surface characterization techniques are involved in the growth process. These precise surface characterization techniques and the dilute molecular beams allow atomically precise control of layer thicknesses, and low growth rates of 1 $\mathring{A}$/sec are typically used [30]. MBE is considered an ideal technique for low-dimensional structures because of its ultra-pure environment and its ability to create high-quality heterostructures.

All the samples presented in this thesis were grown using a Veeco GEN 10 MBE system in our laboratory. A top view of its schematic is shown in figure 3.1. This system is composed of four modules a Growth Module (GM), a Preparation Module (PM), a Cluster Tool module (CT), and a Load Lock module (LL). The materials effusion cells are attached to the GM side-bottom, including two cracker cells for As and Sb. The process of epitaxial crystal growth with these four modules are the subject of this chapter.

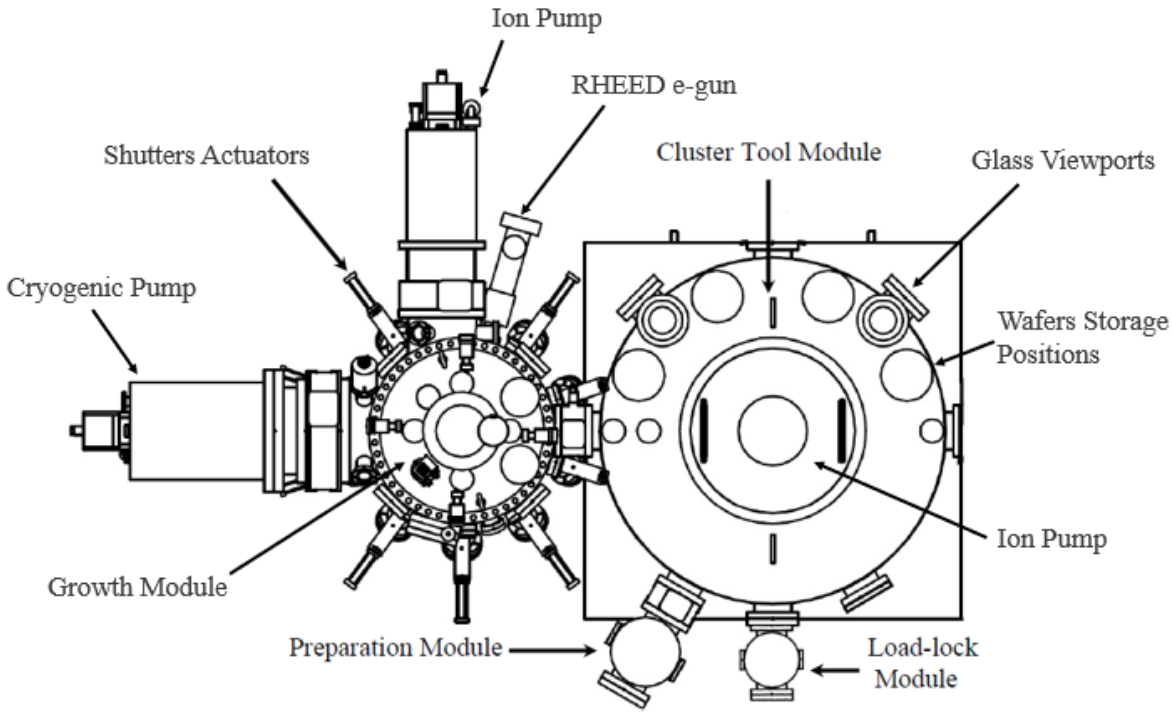

Figure 3.1: A top view of a Veeco GEN 10 MBE System. Retrieved from [79]

3.1.1 Load Lock module (LL)

Load Lock module is the only part in the system regularly opened to air. The wafers are manually loaded on and removed from a movable cassette, which has eight shelves. A motor is attached to the LL bottom, which moves the shelves up and down inside the LL. After the LL exposure to atmospheric air, a turbomolecular pump attached to the top of the LL is used to pump down the LL. Then, the LL is heated up to 200 °C using fixed heating filaments to remove moisture and reach a pressure of 10^{-8} Torr. This outgassing process takes around 4 hours. The LL module is connected to the cluster tool (CT) through a gate valve. After the LL outgassing, a robot arm attached to the bottom of the CT module is used to transfer the new wafers into the CT and move the wafers from the CT to the LL after growth for characterization and processing without breaking the UHV. To monitor the pressure inside the LL, an ion gauge is used and a convectron gauge located beside the port of pumping/venting to measure the pressure on the pump side.

3.1.2 Cluster Tool module (CT)

The Cluster Tool is designed for module-to-module transfers of wafers using the robot arm attached to the bottom of the CT. It has two shelves designed for the wafers storage; each one of these shelves has eight places for holders containing the wafers. The pressure inside the CT is maintained at around 10^{-11} Torr by using an ion pump that is placed on the top of the CT.

3.1.3 Preparation Module (PM)

Preparation Module is used for wafers outgassing and cleaning at high temperatures. Each sample holder can be baked individually on a heating station inside the PM before entering the growth module. The temperatures in PM can reach around 600 °C. In addition, the wafers can be optionally cleaned by hydrogen plasma inside the PM. The pressure inside the PM is maintained by a large turbomolecular pump placed on its side. This arrangement of chambers ensures a high and stable vacuum quality inside the growth chamber and enables the loading/unloading of samples without exposing the main modules to air.

3.1.4 Growth Module (GM)

Growth Module (GM) is the most sophisticated and critical module among all other modules because it is where the epitaxial growth occurs. The schematic of our GM is shown in figure 3.2. The substrate is placed on a manipulator with a heater mounted above to adjust the substrate temperature in the GM. This manipulator can be rotated during the growth. The substrate temperature can be estimated using a thermocouple mounted behind the sample holder on the manipulator or more accurately measured via contactless measurements through viewports facing the wafer with Band Edge Thermometry (BET), Integrated Spectral Pyrometry (ISP), or Reflectance Compensated Pyrometer. A beam flux monitor (BFM) can be placed below the manipulator exactly where the materials' molecular beams would impinge on the substrate for accurate measurements of the materials fluxes. Our GM has two Residual Gas Analyzer (RGA) systems. One is located at the top of the growth chamber and is used to monitor the residual gases in the chamber, and the other one is directed at the wafer surface to monitor the growth chemistry. The GM consists of ten effusion cells at the side-bottom of the chamber to generate the molecular beams of heated materials directed towards the substrate. Each of these effusion cells has its shutter plate to block or let the molecular beams to enter the chamber. Additionally,

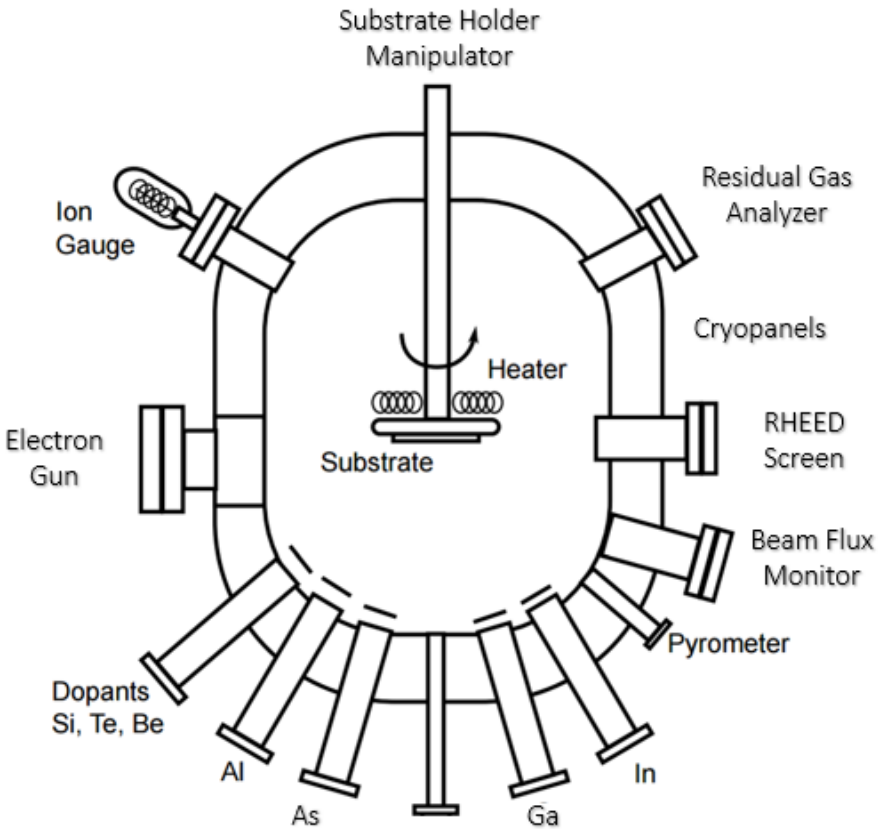

Figure 3.2: The schematic view of growth chamber in MBE system. Retrieved from [75]

the main shutter can be positioned below the substrate to allow the molecular beams to reach the substrate or block them. A RHEED system is used in our system to characterize the sample surface, and it is composed of an electron gun directed towards the substrate at a small angle and a fluorescent screen on the opposite side of the chamber.

GM Ultra High Vacuum

A crucial parameter for high purity MBE growth is that the path in which the molecules have to travel to reach the substrate must be less than the mean free path of these molecules in the molecular beam, and the amount of unwanted atoms is as small as possible [30]. Therefore, to accomplish the UHV environment in the GM, ultra-pure material sources are needed besides a vacuum as clean as possible to prevent contamination and oxidation of

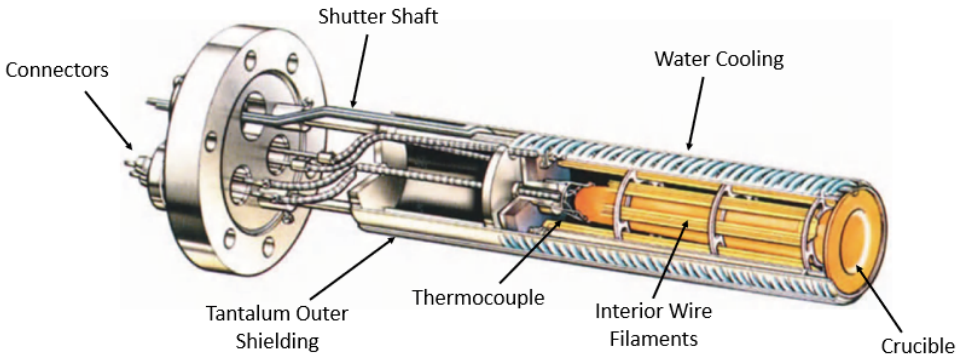

Figure 3.3: Cross-section view of a standard effusion cells used in MBE system. Reprinted from Ref. [31]

material sources.

As shown in figure 3.2, the GM wall is composed of cryo panels through which liquid nitrogen (LN2) is circulated, its purpose is to cool the surfaces down in order to prevent cross-contamination of the source cells, condense water vapor, and to catch molecules that missed or did not stick to the substrate. The GM is mainly pumped down using a CT-10 cryopump, and it has a very cold surface to condense molecules, its temperature is around 10 K to be able to pump also nitrogen, hydrogen, and helium gases. The GM is made out of stainless steel to minimize the outgassing of the chamber material itself; also, it is thoroughly baked after system openings. In addition, all the components inside the GM must be made out of UHV compatible materials like molybdenum, tantalum, or pyrolytic boron nitride (PBN), and they have to be baked out either in the GM or preferably in the PM. To seal windows and ports to the GM, gaskets made of oxygen-free copper are used. They have to be replaced if one of the ports was opened during maintenance. With all these parameters and the continuous pumping of GM, the base pressure inside the GM reaches around 10^{-11} Torr which allows a highly pure crystal growth.

3.1.5 Source Cells

There are two different types of cells for the III/V semiconductors growth, apart from the doping cells like silicon or beryllium. For group III materials special Veeco SUMO effusion cells are used, the schematic structure of an order style effusion cell is shown in figure 3.3. The effusion cell holds a crucible in which the source materials are placed. This crucible is made out of Pyrolytic Boron Nitride (PBN), which is UHV compatible.

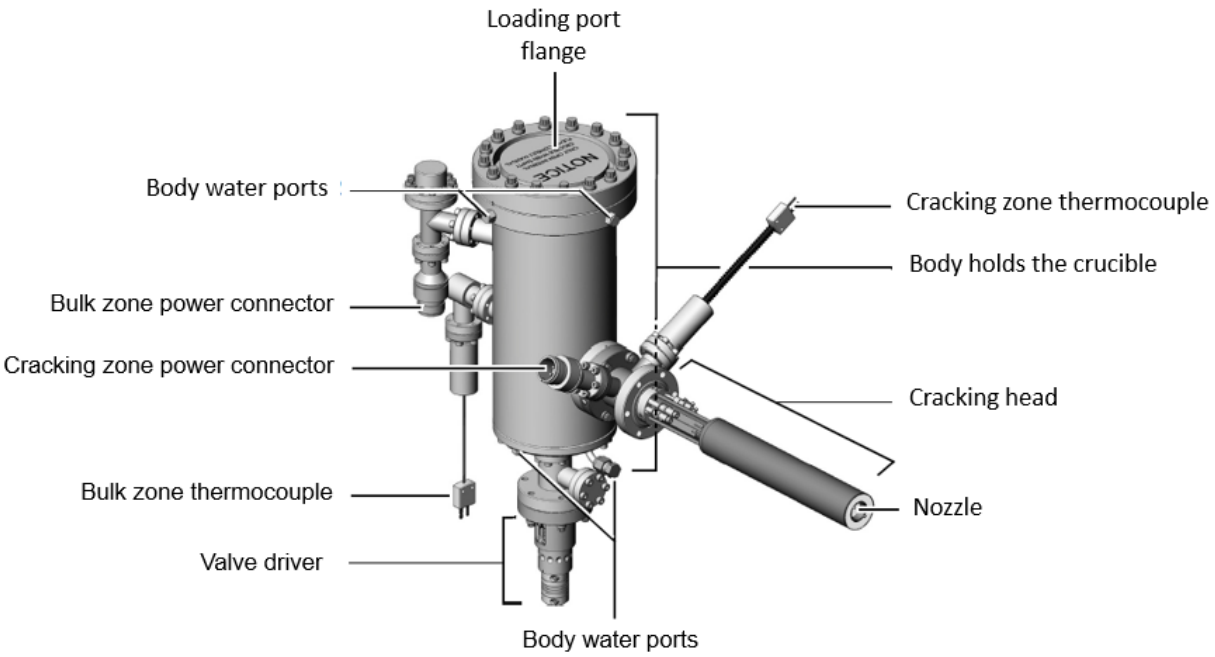

Figure 3.4: The configuration of the Arsenic valved cracker cell (Mark V 500cc) in its port. Reprinted from Ref. [74].

Crucibles have many components designed for creating a uniform flux profile with stable intensity directed at the substrate. The crucible is surrounded by a heater made out of tungsten wire filaments to heat the source materials. The evaporation rate of material from a particular cell is controlled by the source material temperature. The effusion cell temperature is controlled by two-wire filaments, one at the tip of the crucible and one at its base, to have better temperature distribution along with the source material. In our system, Gallium (Ga) and Indium (In) cells temperatures are controlled by using these two filaments, but for Aluminum (Al) cell the tip filament is disconnected to avoid the overflow of Al material from the crucible since Al is wetting PBN crucible and has the tendency to creep up towards higher temperature surface. The temperatures of effusion cells are monitored by using thermocouples for both tip and base temperatures. For Ga and In cells, a SUMO type crucible is used, which has a smaller opening than its inner diameter. Therefore, for a particular crucible temperature, a stable equilibrium pressure is ensured in the crucible. The cell is surrounded by a water jacket for heat extraction. The atomic beams are enabled or blocked by computer-controlled movable PBN or Tantalum shutters.

Another type of effusion cell is used for group V materials such as Arsenic and Antimony.

Group V materials sublimate as tetramers (As_4 and Sb_4) from the source materials. The tetramers of these materials are not as reactive as their dimers (As_2 and Sb_2) or monomers (As and Sb) [30]. Therefore, valved cracking cells are used for As, and Sb materials, where the evaporated materials pass through a cracking zone to be reduced from tetramers into dimers, and hence less cracking has to be done on the substrate surface which benefits their incorporation in the growth. The cracking zone can be heated up to 1400 °C; the proportion of cracked down molecules depends on the temperature of this cracking zone. The cell is designed to have a bulk body with heated filaments, which is the first stage for evaporating the materials then the evaporated beams pass through the cracking zone. The bulk temperatures for As and Sb are kept constant during the growths done in this project at 370 °C and 530 °C, respectively. Despite the high heat of the cracking zone, a gradual accumulation of Antimony can occur on the tip of the cell, which needs to be regularly outgassed. This type of cell also has a shutter to block the molecular beam flux from reaching the substrate. These cells are also equipped with special valves that regulate the flux without changing the bulk evaporator temperature. As an example, the configuration of the As valved cracker cell in its port is shown in figure 3.4. The valve is located inside the body near the exit of the crucible holds the source material.

There is an additional beam collimating aperture that covers the cracking cell port, which minimizes deposits of As and Sb on the cryo panel. The reproducibility of the valve opening in As cells is a crucial parameter in our growths, which will be investigated in the next chapter. In III/V semiconductors growth, the growth rates are determined solely by group III materials, and group V overpressure was used during the growth. The group V/group III flux ratios were adjusted before each growth with the group V overpressure, a slightly higher than 1:1 ratio was used in all our growths.

3.2 In-situ Characterization Tools

In this section, the surface characterization tools inside the GM, which are being used for adjusting the growth conditions, are presented. There are different tools to measure low-pressure regimes and indicate vacuum quality. In our system, we mainly use nude Bayard–Alpert ionization gauges and residual gas analyzer tools. Both of these systems are located in different places in the GM and the pre-chambers to have accurate monitoring of atomic fluxes and vacuum quality within the system.

3.2.1 Beam Flux Monitor (BFM)

An ionization gauge is used with a Beam Flux Monitor (BFM) that can be brought into the path of molecular beams coming from the cells. It is mounted at the side of the GM on a movable UHV compatible arm that can move the gauge below the substrate holder. The ion gauge mechanism is based on a constant flow of negative electrons with a well-controlled rate, is emitted from heated Thoria-coated iridium (ThO_2.Ir) filament (cathode) to ionize the gas molecules. These electrons are accelerated toward a positively charged wire grid (anode) and pass into the space between the grid and a grounded collector wire. In this space, positive ions are produced from the collision of electrons with gas molecules. Then, the grounded collector wire collects the positive ions produced, which is placed along the axis of the cylindrical grid. The density of molecules (pressure) in the space for pressures below 1×10^{-3} Torr is directly proportional to the rate of positive ions formation at a constant filament to grid voltage and electron emission current. A calibrated micro-ammeter in pressure units is then used to indicate the strength of the ion current.

Ion gauges can measure pressures down to 10^{-14} Torr, which allows the measurement of very low beam fluxes. The molecular beam fluxes are measured before each growth using the BFM to adjust the temperature of the cells and achieve the targeted fluxes for a specific growth rate. For each material cell, the flux measurements are saved with the corresponding cell temperature before and after each growth to be used in the cell temperature calibrations for the following growths. The source material within each cell is gradually depleting during each growth. Therefore, cell temperature may have to be changed for new growths to give the same molecular fluxes needed for a specific growth rate. The main shutter can be used to protect the substrate during the flux measurements. In our growth recipe, the BFM is extended to measure the As fluxes in the middle of the growth, which is a critical measurement for our growths.

3.2.2 Residual Gas Analyzer (RGA)

The second instrument used to monitor vacuum quality in our MBE system is the Residual Gas Analyzer (RGA), also known as Quadrupole Mass Spectrometry. It utilizes the difference in the mass-to-charge ratio of ionized molecules or atoms to differentiate between them. An IFICON Transpector MPH Residual Gas Analyzer is placed at the bottom of the GM. Another RGA, an SRS 200, is placed at the top of the GM.

The RGA is composed of a quadrupole mass filter with a range of 1-200 amu equipped with an electron multiplier. The quadrupole mass filter consists of four metal rods arranged

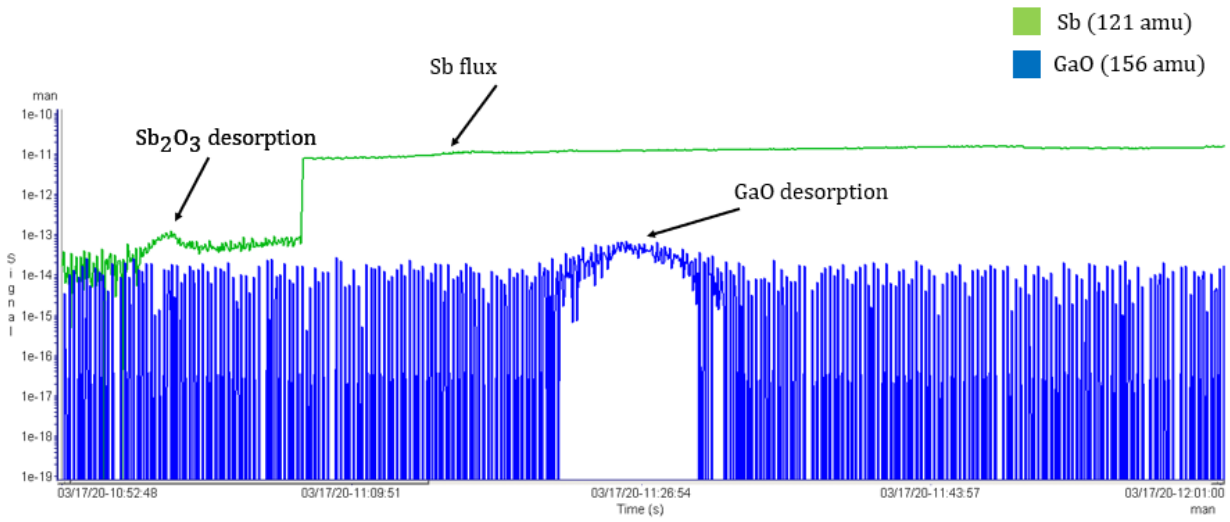

Figure 3.5: The RGA data of oxide desorption process of GaSb substrate used in our growths.

in parallel. Two opposite rods have an applied slightly oscillating potential (DC + AC voltages), and the other two rods also have a slightly oscillating potential of the same magnitude but opposite sign. The trajectory of traveling ions down the space centered between the four rods is influenced by the applied voltages. Depending on the oscillating and non-oscillating voltage applied to the rods, only ions of a particular mass-to-charge ratio pass through the quadrupole filter while the rest is thrown out of their original path. Then, a photomultiplier is used to amplify the signal of the filtered ions. A mass spectrum is obtained by monitoring the ions passing through the quadrupole filter as the rods voltages are changed. Therefore, RGA is useful for quantifying molecules or atoms and the molecules' chemical and structural information.

Figure 3.5 shows two different masses were monitored overtime during the oxide desorption process of the GaSb substrate used in our growths. The green line corresponds to the Sb signal while the blue line is for the GaO signal. The peak in the Sb signal appeared at substrate temperature around 360 °C; after that, the Sb shutter is opened for GaO desorption, where its peak appeared at around 540 °C substrate temperature. The interpretation of the spectrum can be difficult sometimes because the RGA measurement depends on the mass to charge ratio, and ions can be multiply charged. RGA is also being used for vacuum leaks tests as it can be tuned to Helium (He) mass. It also can be used to

test the leakage for new sealed flanges. By spraying helium around the flanges, the increase in He partial pressure would indicate a leak that has to be eliminated.

3.2.3 Substrate Temperature Measurement

The growth temperature of our InAs 2DEG structure is a critical parameter that can affect its electrical and optical properties besides the materials fluxes and the interfaces between the metamorphic buffers in the structure. Therefore, substrate temperature plays a crucial rule during growth, which must be carefully controlled and monitored. As explained before, in chapter two that the molecules during growth can either stick to the surface and migrate there or desorb. They can also be cracked on the surface from tetramers to dimers to monomers and contribute to building the crystals. The substrate temperature can profoundly affect the kinetics and surface chemistry of these processes, impacting the resulting layer quality. A thermocouple is mounted behind the substrate holder measuring its temperature using the Seebeck effect. However, its measurement may be highly inaccurate, if the thermal contact between the substrate holder and the substrate is not perfect or uneven across the wafer. The thermocouple is not in contact with the wafer, so it does not measure wafer temperature, but some intermediate temperature between the heater and the wafer. The wafer and its holder are heated primarily radiatively, while the thermocouple is positioned between the heater and the wafer center. So that different substrate holders can give significant differences in temperature measurements even with the same holder design. This measurement type can give a rough estimation of the substrate temperature with the right calibrations, but we cannot rely on its readings during growth. Substrate temperature can be measured remotely by detecting black body radiation either with pyrometer equipped with bandpass filter or infrared spectrometer, as described below, for more details see Ref. [54, 56].

Reflectance Compensated Pyrometry

Pyrometry is the simplest and most popular non-contact measurement technique for in-situ substrate temperature monitoring during MBE growth. However, this technique has several difficulties. Pyrometry can only be used with opaque wafers, or transparent wafers indium-mounted on opaque wafers like Molybdenum. Because its measurement mechanism relies on simultaneous reflectance at a spectral range where the wafer is fully opaque, therefore, pyrometry wavelength is a crucial parameter in this technique. Reflectance compensated pyrometry (SVT IS4K model) is used in our system for substrate temperature measurements. A light source with wavelength 950 nm is directed towards the substrate,

then thermal emission from the wafer is measured using a narrow band-pass filter. The interference of light in thin films affects the simultaneous reflectance at this wavelength. By measuring this reflectance, the correct thermal emission described by Planck law can be extracted. This method is applicable only for substrates or epitaxial layers, which are fully opaque at 950 nm. The emitted power from the substrate is exponentially decreasing with decreasing wafer temperature. Thus, the lowest temperature can be reliably monitored with this instrument is approximately 400 °C.

Integrated Spectral Pyrometry (ISP)

An integrated spectral pyrometry (ISP) technique is developed in our group for monitoring small bandgap semiconductors temperature during MBE growth [66]. An InGaAs array spectrometer from Control Development, Inc., with a range from 900 nm to 1700 nm, is used, which is usually employed for Band-Edge Thermometry. In this technique, the emitted thermal radiation power from the wafer is integrated over a spectral range where the wafer is opaque to heater radiation. Instead of fitting to the blackbody radiation equation, Separate calibration is made by our group [66]. Before heating the substrate, background scattered radiation signal from all other heat sources within the system is collected. As the signal is integrated over a wide spectral range, the oscillations due to light interference in thin layers are averaged out and do not influence the temperature readings. Therefore, the thermal radiation signal received is coming from the wafer within this wide range. The temperature of wafers can be monitored down to about 200 °C using this method. GaSb is a narrow bandgap semiconductor (opaque substrate); therefore, ISP was successfully used for monitoring its temperature during our growths.

Band Edge Thermometry (BET)

The same ISP spectrometer is being used with the Band Edge Thermometry (BET) in our system. From the temperature dependence of the semiconductor bandgap, the BET can determine the substrate temperature. A light source is directed towards the substrate with an energy larger than the semiconductor bandgap, this light will be absorbed by the sample creating an edge or kink in the spectrum produced. This absorption edge position in wavelength corresponds to the substrate temperature for the respective material. The method works very well for semi-insulating GaAs and InP substrates because their bandgap absorption edge is within the spectral range of the spectrometer. The shape of the absorption edge, which depends on doping, may be altered during the measurements of doped substrates resulting in less accurate measurements for doped wafers or epitaxial

layers. This method is not suitable for materials with an absorption edge beyond the spectrometer range, or the epitaxial layers that strongly absorb in the spectral range of the instrument. Therefore, this method cannot be used with GaSb substrates because its absorption edge is beyond the spectrometer range, and the ISP method is used instead.

3.2.4 Reflection High Energy Electron Diffraction (RHEED)

Reflection High Energy Electron Diffraction (RHEED) is an in-situ characterization technique for characterizing crystalline material surface during the growth. It provides useful information on the current surface that will be buried later under some other layers that are not available after the growth to be characterized. RHEED is composed of an electron gun mounted on one side of the growth chamber facing a photoluminescent detector screen on the opposite side, as shown in figure 3.2. A narrow electron beam (E-beam) is directed towards the substrate holder with a glancing angle of incidence onto the sample, and magnetic deflection coils are used to adjust the angle of incidence of the E-beam. The diffraction pattern from the sample is then detected by the photoluminescent screen, which is transferred to the computer via a camera. This screen is protected by a large shutter to prevent the deposition of materials on the screen when it is not in use. The substrates used for growths have native oxides (Amorphous surfaces), which appear as a diffuse RHEED image. However, a diffraction pattern can appear with RHEED for the surfaces with crystalline order. The diffraction pattern from the crystalline surface can be either spots or streaks, which gives a rough estimation over the smoothness of the surface. In most cases, a rough surface can exhibit a spotty pattern. However, the smoothest surfaces will also show a spotty pattern but distribute in a shape of arcs instead of rectangular patterns like in Transmission Electron Microscope (TEM) [35]. During our growths, we restrain the RHEED measurements to reduce the deposition of Arsenic and Antimony on the photoluminescent screen. RHEED is mostly observed during the oxide desorption of GaSb substrate and during critical transitions like the interfaces for InAs quantum wells, which is presented in the next chapter.

3.3 Ex-situ Characterization Tools

Two ex-situ Characterization techniques are used for characterizing the samples after the growth to investigate the morphology and the crystalline structure. The first one is the optical microscopy presented here, and the second is X-Ray Diffraction, which will be explained in detail in chapter five.

3.3.1 Nomarski interference contrast microscope

Nomarski is an optical microscope which is also known as Differential Interference Contrast (DIC) Microscope. It is used for surface features investigation on typical MBE samples. The crosshatches or oval defects on the surface of the sample can be visible through the DIC microscope. It has better visibility among other optical microscopes of surface features with a smaller height difference. DIC microscope consists of a Nomarski prism on which orthogonal linearly polarized light wave-fronts are split at slightly different angles. These waves are then reflected from the sample surface and recombined by the same Nomarski prism. If a point on the sample surface is higher or lower than its surrounding area, an optical path difference is produced in the reflected waves. A light intensity variation at recombination will be produced due to this optical path difference revealing a topographical profile of the sample surface. Additionally, very flat surfaces can be visible with a DIC microscope. DIC provides a useful and fast assessment of the sample surface without processing. It is a well-tuned instrument that can reveal surface features just a few nanometers tall. Some Nomarski photos for our samples are shown in figure 7.7 in chapter seven.

Chapter 4

MBE growth of InAs-based two-dimensional electron gas

The two-dimensional electron gas (2DEG) in InAs quantum wells has been studied due to its potential applications for mesoscopic physics experiments utilizing its high carrier mobility, strong spin-orbit coupling, and high Landé g factor. In recent years, 2DEG in InAs quantum wells is considered as a new prospect for realizing a topological superconducting phase supporting Majorana fermions when combined with s-wave superconductors [67, 60, 17]. Majorana fermion is defined as a fermion that is its own antiparticle, it was hypothesized by Ettore Majorana in 1937 [45]. Qubit is the quantum analog of the classical bit, which is the basic building block of a quantum computer. Many of the current implementations of qubit systems that encode the information in the particles themselves, such as ion trap qubits and superconductors, are highly susceptible to noise and decoherence [53, 44]. As mentioned before, topological qubits can offer a way out of this problem. A system may host the so-called "Majorana Zero-Modes" (MZMs) quasiparticles, when the degeneracy is two-fold, and enumerated by fermion parity, then the ground states show Majorana exchange statistics [50]. It is the most interesting property of MZMs because it means that exchanging the position of MZMs corresponds to a non-trivial transformation within the degenerate ground-state manifold and represents a non-commutative operation, which does not depend on the method or details of its execution [44]. Therefore, such an operation is topologically protected and may be used to implement quantum gates. In such a scheme, the information is encoded not in the quasiparticles themselves, but in how they interact and are braided [78]. A few realizations of mesoscopic devices have been reported that experimentally revealed evidence of Majorana zero modes. For example, top-down lithography and gating were used to define a hybrid semiconductor-superconductor wires in

a two-dimensional InAs/Al heterostructure where the behaviour of zero-bias conductance peaks of these devices is consistent with the emergence of MZMs as seen in individual nanowires studies [65, 52]. These observations are considered as robust evidence of the MZMs existence by using the top-down approach for mesoscopic devices. For all these devices, a high crystal quality with a low disorder, indicated by high electron mobility, is of significant importance to explore novel topological states and mesoscopic phenomena.

The carrier mobility of InAs quantum wells has been confined for a long time to regions below 1×10^6 cm^2/Vs, for example, the carrier mobility of 1×10^6 cm^2/Vs was achieved in composite quantum wells of InGaAs/InAs grown on semi-insulating (100) InP substrates where the InAs quantum wells were a 120 nm far from the top surface [77, 29]. However, InP substrates are not the perfect candidate for growing InAs quantum wells as the lattice mismatch between InP and InAs compounds are around 3.5%. Therefore, thick graded buffer layers must be used with InP substrates, which can modify surface morphology due to the dislocations introduced. In addition, GaAs quantum wells have reached mobility values above 3×10^7 cm^2/Vs despite its higher effective mass [55], which implies that there is a room for improving growth techniques and structure designs of InAs quantum wells to enhance the electronic properties of InAs 2DEG. Undoped quasi-lattice matched (100) GaSb substrates has been recently used for growing InAs quantum wells, where the lattice mismatch between InAs and GaSb is nearly -0.61%. The 2DEG mobility has reached $\mu \sim 2.4 \times 10^6$ cm^2/Vs at carrier density $n \sim 1 \times 10^{12}$ cm^{-2} of InAs quantum wells buried 25 nm from the top surface grown on GaSb substrates [67, 70], thus, the defects generation has been reduced in these structures. Additionally, $Al_xGa_{1-x}Sb$ is used as the lower and top barriers for the InAs quantum well; they increased the electron wave-function confinement within the quantum well [67].

This chapter details the growth of 2DEG in InAs quantum wells by going through each layer starting at the buffer layer up to the capping layer, optimizing the structural design parameters according to X-Ray Diffraction measurements and magnetotransport data. We use these measurements and the material properties extracted from them to identify the effect of growth conditions on the electrical properties of the fabricated devices.

4.1 Growth of InAs Quantum Wells

All the studied samples were grown on undoped quasi-lattice matched (100) GaSb substrates. The material structure of the presented samples is shown in figure 4.1 with the associated band structure, which is inspired by Ref. [67]. A quaternary buffer layer $Al_xGa_{1-x}As_ySb_{1-y}$ with thickness 800nm, is used for all the samples, the influence of this

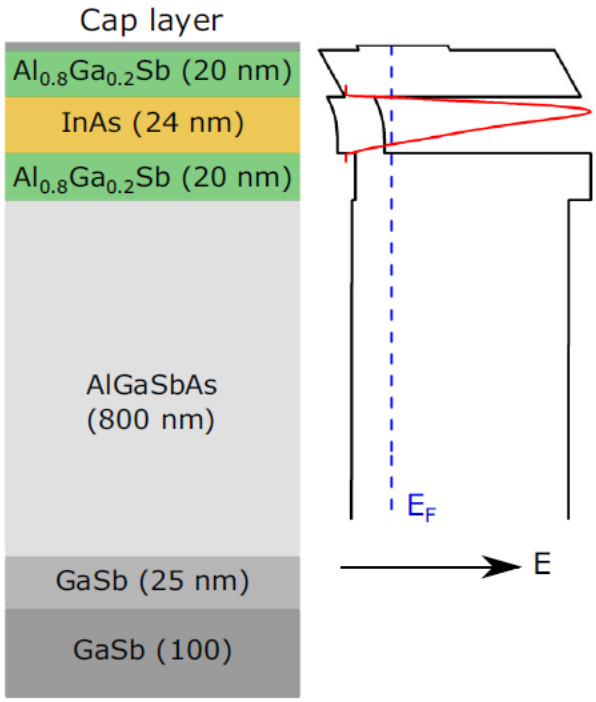

Figure 4.1: Schematic structure of the InAs quantum wells used in this study with the associated band structure. The conduction and valence bands are represented by the black bands at the Γ point. Fermi level (E_F) is the dashed blue line. The red curve corresponds to the wave function of the two-dimensional electron system. Reprinted by permission from Ref. [67]

buffer and substrate type on sample quality is going to be discussed in this chapter. The dependency of the buffer quality on the group five materials Arsenic (As) and Antimony (Sb) incorporation will be discussed, and how it affects the electron mobility and density. Besides, we will take a closer look at the dependency of electron mobility and density on growth strategies for the barriers and interfaces surrounding the quantum well, the capping layer, and the quantum well itself. The mobility and density values are presented in chapter six with the Quantum Hall effect measurements and magnetotransport data for almost all the samples presented here.

4.1.1 Quanternary Buffer Design

Buffer systems are defined as a series of layers grown between the substrate and the quantum well region in the crystal structure. The main purpose of these buffers is to provide a smooth surface for the quantum well to be grown upon and to confine crystal defects propagating through the structure such as threading dislocations below the quantum well region. In addition, buffer systems in lattice-matched structures should provide insulating layers between substrate and quantum well to prevent current leakage from the electrostatic back gate into the quantum well. The quaternary buffer $Al_xGa_{1-x}As_ySb_{1-y}$ is proved to provide better isolation between the GaSb substrate and InAs quantum wells than the simple GaSb buffer layer [67, 62] due to its higher bandgap energy. A smoothing layer of 25nm GaSb was grown directly before the quaternary buffer; this layer is essential to smoothen the substrate surfaces after oxide desorption because these surfaces are far from being atomically at that point and are not suitable to grow quantum wells after oxide desorption directly. The native antimony oxide (Sb_2O_3) of the GaSb substrate was removed at 380 °C substrate temperature without Sb flux. Then, to remove Ga_2O_3, the substrate temperature was increased to 540 °C with Sb flux. The oxide desorption was monitored during the growth using Residual Gas Analyzers (RGA) for all samples presented.

The growth of this quaternary buffer with high quality was not an easy task due to the presence of two group five materials in the buffer that creates a non-trivial growth environment. The AlGaAsSb material system was first introduced as a promising material system for heterojunction transistors and optoelectronics systems [81]. It has been successfully grown on InP and GaAs substrates. However, the accuracy and the reproducibility of the (As, Sb) composition is challenging to achieve due to the dynamic competition between them on the surface during the growth which depends critically on growth conditions, since both of them do not have a sticking coefficient equals to one and are function of substrate temperature and group III fluxes [58]. Another reason is the wide miscibility gap in $Al_xGa_{1-x}As_ySb_{1-y}$ which affects the major range of Sb concentration [27]. Specifically, when $Al_xGa_{1-x}As_ySb_{1-y}$ is grown on InP substrates, to achieve the lattice matching between them, the composition y should be around 50%. However, providing the same amount of both As and Sb on the surface during the growth can lead to different interactions on the surface, which result in a modification of the incorporation process of each species. Therefore, the group five materials composition is difficult to be controlled due to the tendency to be either As-rich or Sb-rich, relying on which species has the best sticking coefficient [25, 4].

Many studies were conducted on the incorporation of (As, Sb) materials in a particular layer. The effect of the growth rate on incorporating (As, Sb) is still subject to debate.

A linear relation was reported by Almuneau et al. [4] for $Al_xGa_{1-x}As_ySb_{1-y}$ between Sb flux and the Sb mole fraction in the layer. These results concluded that the incorporation of Sb has to be close to unity. In a research paper by Semenov et al. [59], authors reported that, with increasing the fluxes of group III, the As mole fraction has increased in $Al_xGa_{1-x}As_ySb_{1-y}$ and $GaAs_xSb_{1-x}$ with constant group V fluxes. It indicates that the higher growth rates will result in a shortage of Sb and the excess As will fill the unoccupied lattice sites. Other authors have stated the opposite. Sun and co-workers [64], reported that if the growth is performed at high growth rates, the dependence of the composition on the growth rate can be eliminated. The authors assumed that there are plenty of Ga sites available with the high growth rates, which prevent the desorption of Sb. As a result, the incorporation efficiency is increased since the dissociation of the Sb species is promoted due to the Ga sites available on the growing surface [64]. Additionally, Selvig et al. investigated the growth of $Al_xGa_{1-x}As_ySb_{1-y}$ and $GaAs_xSb_{1-x}$ on GaSb substrates with Sb compositions up to 0.2 [58]. It was observed that at lower growth rates the Sb incorporation is decreased, and their study concluded that if the $GaAs_xSb_{1-x}$ is grown at a lower growth rate, the lower composition of Sb is found in the layer because at the growing surface exchange of As-for-Sb reaction takes place. Additionally, it was found that the As composition in $Al_xGa_{1-x}As_ySb_{1-y}$ does not depend on the Al mole fraction (x). Therefore, they concluded that unintentional variations in the growth conditions are the reason for different As composition in each growth and the most probable reason is the group III fluxes [64].

The substrate temperature during the growth is another crucial factor that can affect the incorporation of group V materials, as was first demonstrated by Klem et al. [37]. Researchers generally agreed on the inverse relation between the substrate temperature of the growth and the incorporation of Sb in $GaAs_xSb_{1-x}$ and $Al_xGa_{1-x}As_ySb_{1-y}$ [64, 82, 58]. Since the As composition is a function of four parameters (growth rate, As flux, Sb flux, and substrate temperature), in order to achieve the desired As fraction in our samples, the growth rate, Sb flux, and substrate temperature were held constant for all the samples and the only variable we had every time was the As flux.

A new method is developed in this thesis to control As composition in $Al_xGa_{1-x}As_ySb_{1-y}$ buffer layer by using ex-situ measurements with X-ray diffraction (XRD) to achieve the lattice matching between the buffer and the GaSb substrate. This method depends on calculating the As composition of each buffer layer using Vegard's law by extracting the in-plane, and the out-of-plane lattice constants of the buffer layer from the symmetric and asymmetric reciprocal space maps scans by X-Ray Diffraction. The details of the XRD scans are presented in chapter five.

4.1.2 MBE growth of $Al_xGa_{1-x}As_ySb_{1-y}$ buffer layer

All the parameters mentioned before were held constant during the growth of our samples, while the As flux was the only variable during the buffer layer growth. Different parameters of $Al_xGa_{1-x}As_ySb_{1-y}$ growth in our samples are shown in table 4.1. The fluxes mentioned in this table were measured using Beam Flux Monitor (BFM) in-situ before starting the growth. The Sb flux is held constant by first measuring it by BFM then adjusting the Sb valve opening to achieve the Sb flux needed. The molecular fluxes of group III elements were also measured by BFM before growth, and their cell temperatures were adjusted to achieve the flux needed for each element. As the growth rate is controlled by group III elements, by holding their fluxes the same for each growth, the growth rate would always be the same, which was 2 $\mathring{A}$/sec ($\sim$ 0.33 Monolayer/sec). The substrate temperature (T_g) was measured by Integrated Spectral Pyrometry (ISP) during the growth and was held at 500 °C for all the layers in the material structure shown in figure 4.1. The substrate temperature was controlled by adjusting the substrate heater power. The cracker temperatures used for Sb and As were 950 °C and 1000 °C, respectively. So that by keeping these parameters constant, As flux was the only variable in all growths.

For an accurate measurement of As flux, the growth chamber was first saturated with As for 10 minutes with a large valve opening of 300, and then the valve opening was decreased to the needed value, and the As flux reading was taken by the BFM after reaching the steady-state. The As saturation period and As flux steady state are shown in figure 4.2. In the beginning, the procedure of growing $Al_xGa_{1-x}As_ySb_{1-y}$ buffer layer was as follows:

1. Before starting the growth and after the saturation of growth chamber with As, the As valve was opened to a certain value, and the corresponding As flux was measured.

2. The previous step was repeated many times until a steady state of As flux was reached with the As flux value that was going to be used during the growth of the buffer, figure 4.2.

Growth Rate	2 $\mathring{A}$/sec
Al flux	2.80×10^{14} $cm^{-2}s^{-1}$
Ga flux	6.99×10^{13} $cm^{-2}s^{-1}$
Sb flux	1.54×10^{6} $cm^{-2}s^{-1}$
T_g	500 °C

Table 4.1: The growth parameters of $Al_xGa_{1-x}As_ySb_{1-y}$, where T_g is the substrate temperature during the growth.

3. The valve opening value was recorded, then the As valve and shutter were closed to start the oxide desorption of the substrate.

4. After oxide desorption and the growth of 25nm of GaSb smoothing layer, the As valve and shutter were opened with the recorded As valve opening value to start the growth of $Al_xGa_{1-x}As_ySb_{1-y}$ buffer layer.

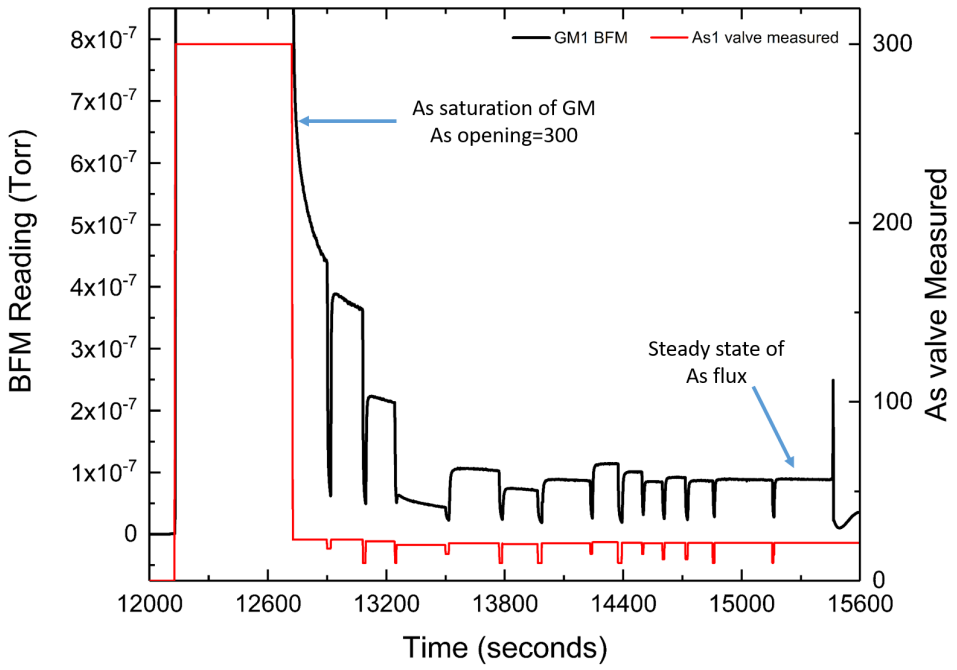

Figure 4.2: The BFM measurments of As flux (Black line) and the corresponding As valve opening values (Red line). The As saturation of the growth chamber (GM) and the As flux steady state are shown.

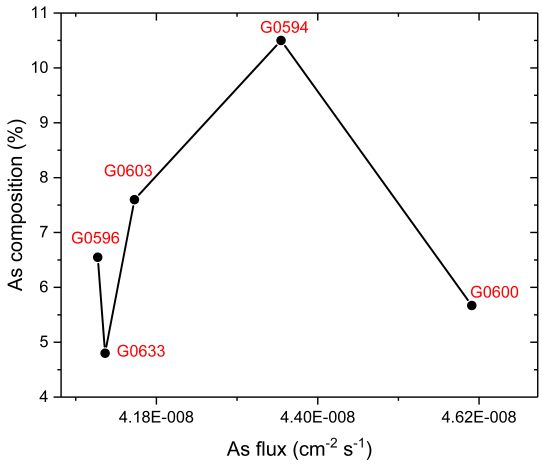

Figure 4.3: Plot for As composition versus As flux.

Sample ID	As flux	As composition %
G0594	4.35×10^{-8}	10.5 %
G0596	4.10×10^{-8}	6.6 %
G0600	4.61×10^{-8}	5.7 %
G0603	4.15×10^{-8}	7.6 %
G0633	4.11×10^{-8}	4.8 %

Table 4.2: The As composition and As flux of the samples grown using the first method of growth.

The As compositions of the samples grown with this method are shown in table 4.2 with a plot of the results for comparison 4.3. This method failed to reproduce the same As composition for the same As flux. The reason behind that is the lack of valve opening reproducibility. Upon closing and opening the valve to the same valve value, the As flux produced is different.

In order to have a good reproducibility of As composition, the procedure of the buffer growth was changed as follows:

1. After measuring the fluxes of all materials (Al, Ga, and Sb) except As the substrate temperature is raised for oxide desorption followed by the smoothing layer growth.

2. After growing the GaSb smoothing layer, the substrate temperature is decreased to 350 °C with Sb flux.

3. When the substrate temperature reaches 350 °C, the main shutter below the substrate and Sb shutter are closed, and the BFM is extended under the substrate to measure the As flux.

4. The As flux is measured exactly like point 2 in the previous method, and the As flux is recorded for next growths.

5. The As shutter and valve are kept open with the valve opening value chosen from the measurements.

6. The Sb shutter and main shutter are opened, then the substrate temperature is raised again to 500 °C to start the growth of $Al_xGa_{1-x}As_ySb_{1-y}$ buffer layer.

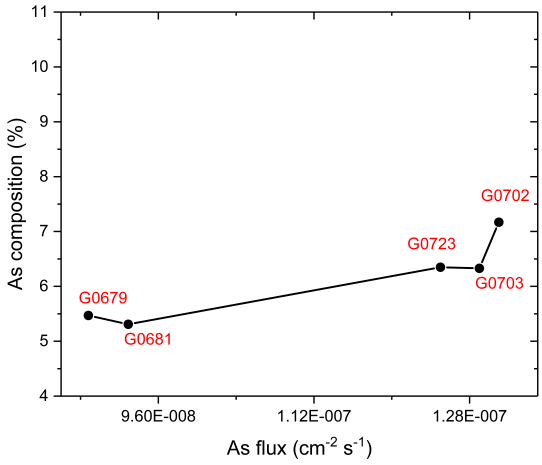

Figure 4.4: Plot for As composition versus As flux.

Sample ID	As flux	As composition %
G0679	8.88×10^{-8}	5.5 %
G0681	9.29×10^{-8}	5.3 %
G0702	1.31×10^{-7}	7.2 %
G0703	1.29×10^{-7}	6.3 %
G0723	1.25×10^{-7}	6.4 %

Table 4.3: The As composition and As flux of the samples grown using the first method of growth.

This method of buffer growth has successfully achieved the reproducibility of As composition, as shown from the results in table 4.3 with a plot of the results 4.4. It can be seen that the As flux is consistent with the corresponding As compositions achieved in each $Al_xGa_{1-x}As_ySb_{1-y}$—all As compositions were calculated using the XRD model that will be explained in the next chapter.

In conclusion, we succeeded in achieving reproducibility using the second method of growth. An attempt to leave the As valve opened with its shutter closed before starting the growth and after measuring the As flux could have been done. However, it was found that As flux can reach the substrate with the As shutter closed and As valve opened due to its small sticking coefficient to the walls, and it can incorporate in the GaSb smoothing layer growth replacing Sb atoms [33]. Therefore, As valve must not be open during the growth of the GaSb smoothing layer to avoid growing GaAsSb instead of GaSb. On the other hand, the Sb valve was kept open during the whole growth, and its shutter was only closed during the growth of InAs layers because Sb cannot reach the substrate surface because it sticks 100 % to chamber walls [33]. That was the reason behind closing the As valve and shutter during the oxide desorption and GaSb layer growth and measuring the As flux directly before the growth of the buffer layer. Additionally, the variations of As compositions in the buffer layer are found to affect the carrier charge density and mobility in InAs quantum wells. The results and discussion of carrier density and mobility measurements are presented in chapter 7.

4.1.3 Origin of Charge Carriers

Commonly, to introduce charger carriers into quantum wells, doping with acceptor or donor atoms is used. One or more doping layers are usually placed in the barrier layers away from the quantum well to reduce scattering by the subsequently ionized acceptor or donor atoms. In our growths, the InAs/$Al_xGa_{1-x}Sb$ quantum wells are not intentionally doped; however, they have high electron sheet concentrations. Electron concentrations have been achieved in the range from less than 3×10^{11} cm^{-2} to more than 15×10^{11} cm^{-2} for InAs quantum wells by variation of barrier thickness. The deep donors in the $Al_xGa_{1-x}Sb$ barrier are thought to be a major source of electrons, which would drain into the very deep well [71]. These deep donors' origins may be antisite defects like anion-site Al_{Sb} in the barriers or oxygen impurities incorporated during growth, and their contribution depends on the purity of the growth as proposed by Ref. [24].

The surface states from the cap layer is another vital source of electrons in the quantum well. Transfer of electrons from these surface states to the quantum well will occur until the

surface states are pulled down to the same energy as the Fermi level inside the quantum well by the electric field generated from the charge transfer. Therefore, the amount of electrons introduced in the quantum well from the cap layer depends strongly on the distance between them. By varying the thickness of the upper barrier, the charge density inside the quantum well can be tuned. A thin layer of GaSb is commonly being used as a cap layer because of its high ability to enhance this effect as opposed to an InAs cap layer. The source of difference between these two cap layers lies in the energy at which the Fermi level is pinned at the surface, where the GaSb cap layer pulls the conduction band much further down compared to the InAs cap layer, leading to generally higher densities [51].

The cap layer has to be carefully chosen as it can also significantly impact scattering in the 2DEG. It was found by Thomas et al. [67] that thin InAs cap layer facilitates the full depletion of the 2DEG with gating, however, it does not sufficiently screen the 2DEG from surface defect scattering which can affect the mobility in the quantum well. On the other hand, the GaSb cap layer appears to have the ability to screen the 2DEG from the surface charge, enhancing mobility, but it prevents the full depletion of the 2DEG with gating. In this context, the InAs cap layer has proved to be favored over GaSb because it has enabled the full depletion of the 2DEG with the least possible residual side wall conduction [70, 62]. In our growths, a thin InAs cap layer is used with $Al_xGa_{1-x}Sb$ as an upper barrier of 20 nm thickness. We believe that this cap layer is the dominating source of electrons in the InAs quantum well.

4.1.4 Barriers

The most common barriers for InAs quantum wells are made of AlSb because it has the largest bandgap in the 6.1 $\mathring{A}$ semiconductor family (InAs, GaSb, and AlSb). Thus, it provides a huge conduction band offset to InAs, which is 1.35 eV. It provides good confinement for the InAs QW; however, it increases the built-up strain energy of the crystal. Alloying these barriers with Gallium decreases the electron wave-function confinement in the InAs QW but significantly reduces the strain energy in the structure [67]. Due to the lattice mismatch to GaSb substrate and InAs QW is reduced with decreasing the Aluminium content in the $Al_xGa_{1-x}Sb$ barrier.

Alloying the lower barrier with Ga can also significantly increase mobility with slightly lower carrier density. However, the valence band energy of the barrier will rise relative to the conduction band energy of the quantum well. Reducing the Al fraction below x=0.3 in $Al_xGa_{1-x}Sb$ layer pushes the valence band of the barrier above the conduction band of the well. In this case, some holes can be induced in the $Al_xGa_{1-x}Sb$ layer due to the

transfer of electrons from the $Al_xGa_{1-x}Sb$ valence band to the InAs conduction band [43]. In addition, lower confinement energy can increase alloy scattering as a result of a larger fraction of the electron wave function being inside the upper barrier. Therefore, we chose a mole fraction of x=0.8 for the $Al_xGa_{1-x}Sb$ barriers in our structures because it increases the electron wave-function confinement in the QW due to its large bandgap (1.41 eV).

The upper barrier width plays a crucial role in the electron density within the 2DEG, as explained in section 4.1.3. Most of the electrons come from fermi level pinning by surface states and deep ionized donors in the barriers. Increasing the upper barrier thickness increases the distance between these surface states and the quantum well. The greater distance results in a less pulled-down of the InAs band edge due to the reduction in the electric field strength at the quantum well, leading to a lower electron density. In most cases, higher intrinsic mobility results from the increased carrier density. Therefore, a narrow upper barrier of 20 nm was grown for our InAs quantum wells, to compensate that effect and keep the density in a range that can achieve high mobility. Decreasing the upper barrier thickness would not guarantee higher mobility because the closer surface is also likely to increase remote impurity scattering [70].

4.1.5 InSb-like and AlAs-like Interfaces

Group III elements (Al, Ga, and In) and group V elements (As and Sb) will all influence the interface between the InAs quantum well and the $Al_xGa_{1-x}Sb$ barriers. There are two different ways of forming these interfaces, as shown in figure 4.5. In this figure, the

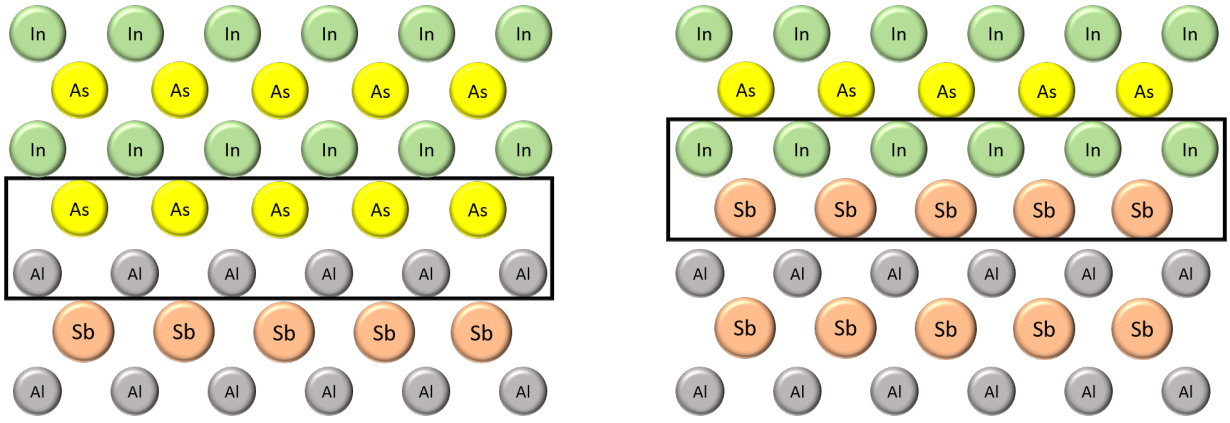

Figure 4.5: Left: schematic of an AlAs-like interface. Right: schematic of an InSb-like interface. Highlighted areas are the respective interfaces.

transitions are illustrated for AlSb barriers with InAs quantum well, but similar transitions will occur with $Al_xGa_{1-x}Sb$ barriers. The first transition happens when the $Al_xGa_{1-x}Sb$ is terminated with its group III element Aluminium and then continued with arsenic, which is the group V element in the quantum well, resulting in an AlAs-like transition. The $Al_{0.8}Ga_{0.2}Sb$ barrier is more likely to be terminated with Al more than with Ga due to the small mole fraction of Ga in the barrier layer. Another transition happens when the $Al_xGa_{1-x}Sb$ barrier terminates with antimony and is continued with indium from the quantum well, resulting in an InSb-like interface. With appropriate shutter sequences, a particular transition can be forced. It was found by Tuttle et al. [72] that at the lower interface, the InSb-like interface enhances the mobility of the corresponding quantum well more than the AlAs-like interface. They postulated that Al_{As} antisite defects could appear with an AlAs-like interface, where As atoms replace Al atoms in some sites in the lattice while the AlSb barrier surface is exposed to arsenic flux. These antisite defects can act as charged impurities adjacent to the quantum well when they become ionized due to the large band-offset, which may increase electron densities but significantly decrease electron mobilities. Also, the AlAs-like interface is indeed rougher than the InSb-Iike interface, which introduces large interfacial scattering into the quantum well, which can be the reason behind most of the mobility reduction [72]. There was an insignificant effect observed for the interface type between the quantum well and the upper barrier, where Al_{As} antisite defects can not form because during AlAs-like transition from InAs to AlSb there would be no long period exposure of As on Al-containing layer [72].

The process we used to force InSb-like interfaces is derived from Tuttle et al. [72] for the lower and upper interfaces. For a lower InSb-like interface, all group III fluxes are turned off after growing $Al_xGa_{1-x}Sb$ lower barrier while the Sb flux is kept on to generate Sb rich surface. This process can be observed in RHEED, where $Al_xGa_{1-x}Sb$ has (1×3) reconstruction changes to (1×5) reconstruction for Sb rich surface [10] (figures 4.6a and 4.6b). Sb flux is closed once Sb-rich reconstruction is observed, after which an indium monolayer is deposited. The 500 °C growth temperature may be too high, and we may lose this InSb interface before growing InAs. It may explain lower mobility than expected. A complete indium monolayer growth can also be checked using RHEED, where the reconstruction should change completely (figure 4.6c). After that, the As valve is opened to proceed with InAs growth (figure 4.6d). Our observed RHEED reconstructions are similar to those observed in Ref. [69].

InSb-like transition growth temperature is crucial for the quality of the interface and electron mobility. For higher temperatures, Sb antimony rich surface decomposes faster. It was found by Tschirky et al. [69] that the ideal growth temperature of InSb is around 435 °C. Therefore, the substrate temperature should be lowered during the InSb-like transition.

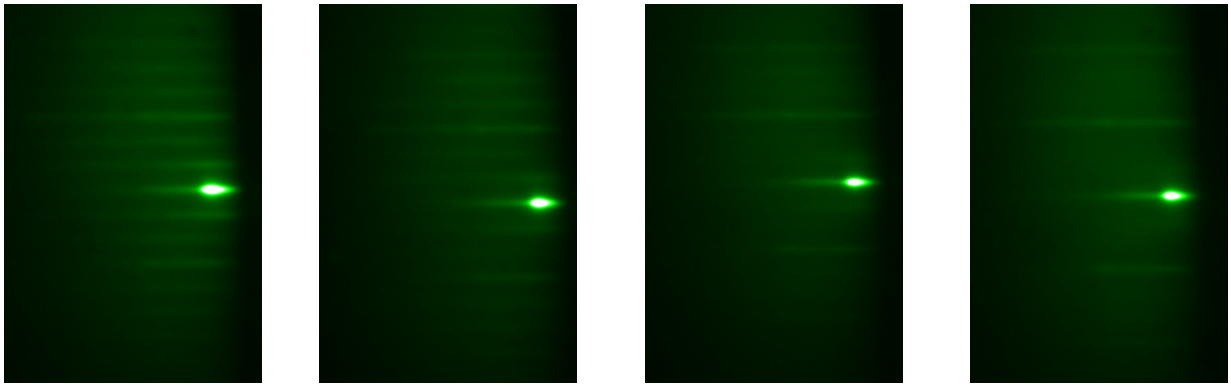

(a) $Al_{0.8}Ga_{0.2}Sb$ (b) Sb rich surface (c) In Monolayer (d) InAs Growth

Figure 4.6: Captured RHEED patterns of the InSb-like transition at the lower interface between $Al_xGa_{1-x}Sb$ and InAs.

At these temperatures, the samples achieved a very reproducible density and mobility. This temperature was used during the growth of the InSb-like interface in some of our samples, but they were unsuccessful attempts. For the InSb-like upper interface, the sequence of shutter and valve is reversed. The upper interface temperature was not of significant importance due to the stability of In in the terminated layer, which is more than Sb like in the lower interface. Therefore, it was grown with the same temperature of the proceeding InAs growth.

4.1.6 InAs Quantum Well

InAs quantum well is the most important part of our material structure, which lies between the two interfaces described previously. Growth of InAs quantum well has three critical growth parameters, the group III to group V materials ratio, the InAs growth temperature, and the quantum well width. Arsenic flux lower than 2×10^{-6} Torr can influence the electron mobility in the InAs quantum well [69]. For our samples, an As flux of around 7.5×10^{-6} Torr was used with a constant indium growth rate of 2 $\mathring{A}$/sec. Increasing the As flux more than that value would not enhance the mobility, but only it can increase the group V intermixing probability in the upper barrier [69]. An effective As-to-In ratio of a slightly higher than one was used for the InAs growth to avoid the void defects associated with the etching of InAs during processing, which can be formed in the $Al_xGa_{1-x}Sb$ layer underneath [67].

As stated before, the substrate temperature used for InAs growth in our samples is 500

°C. It was found by Kuze et al. [40], the highest electron mobilities in InAs quantum wells were achieved for a range of temperatures from 460 °C to 490 °C and the optimal growth temperature for quaternary buffer $Al_xGa_{1-x}As_ySb_{1-y}$ was around 500 °C. Additionally, a substrate temperature of 500 °C was used for the material structure in figure 4.1 by Thomas et al. [67]. At this temperature, mobilities of around 2×10^6 cm^2/Vs were achieved in InAs quantum wells [67].

The last growth parameter that influences the mobility in InAs quantum well is its width thickness. Decreasing well width causes a reduction in mobility as a result of increased interface roughness scattering as discussed by Bolognesi et al. [8, 7]. They found that the mobility keeps increasing for quantum wells wider than 15 nm, where the widest sample with 24 nm has achieved a mobility of around 1.8×10^6 cm^2/Vs at a carrier density of 8×10^{11} cm^{-2}. However, it was also found that, when the thickness of InAs quantum wells exceeds 15 nm, the mobility starts to decrease [8]. The reason behind this reduction is either the InAs critical thickness being exceeded inducing misfit dislocations or the early beginning of intersubband scattering due to smaller subband energy spacing in wider quantum wells [69]. In our case, the electrons will not be able to populate the second subband due to the low intrinsic density in our samples with the 24 nm thick InAs quantum well. Growing InAs quantum wells on nearly lattice-matched GaSb substrates will eliminate the threading dislocations and make it possible to grow wider InAs quantum wells and further enhance the mobility by reducing the interface roughness scattering. It is supported by our XRD scan shown in figure 5.8 in chapter five, which shows the InAs peak being strained and no signs of relaxation for the InAs layer with 24 nm thickness.

The increase in mobility with wider quantum wells can be attributed to the increase in distance between the lower barrier and the wave function. The surface states electric field is always drawn the lower barrier to the surface, leading to an increase in interface roughness scattering. By moving the lower barrier away from the wave function, the number of electrons being at the interface or in the lower barrier is decreased, reducing the interface roughness scattering and enhancing the mobility [42]. It was found by Tschirky [69], the increase of mobility flattens with well width from 21 nm to 24nm, and a further increase in the width will not result in higher mobility. In our samples, the InAs quantum well thickness is 24 nm to utilize the high carrier mobility of the wider wells.

Chapter 5

Characterization of the Quaternary buffer layer using X-Ray Diffraction

5.1 Introduction

X-ray diffraction is a powerful tool to characterize the structure of crystalline materials. A highly monochromatic X-Ray beam with a well-defined wavelength and a low angular divergence is directed onto a crystalline material. The angle at which the X-Ray beams are diffracted from the crystalline material provides useful information about its crystal structure. Max Von Laue was the first one to study the interaction between X-Rays and crystals in 1912 [20]. He discovered that the periodic arrangement of atoms in a crystal would cause an interference pattern of the X-Ray beams diffracted. The mean positions of atoms in a crystal and their crystallographic disorder can be determined from the angles and intensities of these diffracted beams. Later, W. H. Bragg and W.L. Bragg postulated the conditions for which the diffraction will occur, and it is well-known as Bragg Law [11].

5.2 High Resolution X-Ray Diffraction

All metals, when excited with a high-energy electron beam, will exhibit characteristics X-Ray lines at different wavelengths. However, to examine semiconductor crystals, the wavelength of the radiation has to be of the same order of magnitude as the lattice constant of their crystal. Therefore, the most commonly used radiation line for the analysis of III/V semiconductor crystals is the Kα_1 characteristic line of copper, which has a wavelength of

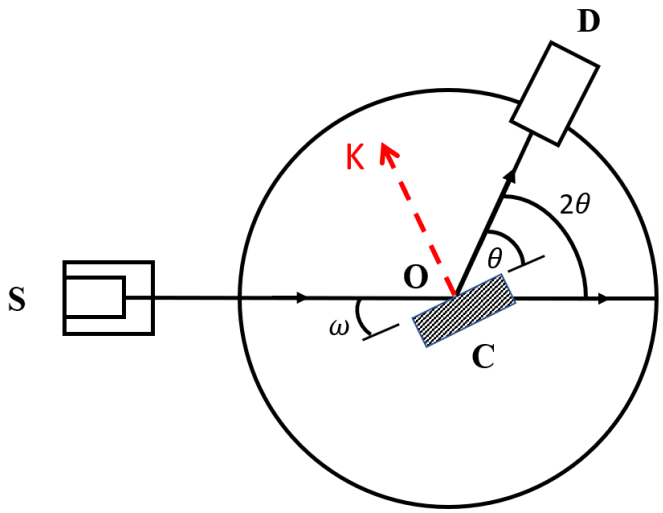

Figure 5.1: High-Resolution X-Ray Diffraction Setup. Reprinted from [16]

1.5418 $\mathring{A}$. Thus, a monochromator beam source is used in the X-ray diffraction to provide a conditioned beam. The High-Resolution X-Ray Diffraction (HRXRD) setup is shown in figure 5.1, which shows the typical configuration of a single crystal diffraction experiment. High angular resolution is needed in HRXRD because the widths of diffraction peaks and fringes will be typically in the arc second range (3600 arcsec = 1 deg), therefore the details examined will be at the arcsecond scale and the substrate peak can be used as an angular reference [9]. X-rays are emitted from the source S and directed onto the crystalline sample C, mounted on a sample holder. The crystal can be rotated about an axis through O, as shown in figure 5.1, which allows the crystal to be set at any desired orientation. The angle ω is the incident angle of the X-Ray beams with respect to a particular set of crystal planes. The detector D can also be rotated around an axis through O. X-Ray diffraction (XRD) theory, and related equations are explained by the Bragg law, which determines the angles at which scattered x-ray beams will interfere constructively. In general, X-rays can also be absorbed, transmitted, reflected, refracted, and scattered incoherently when interacting with matter [9].

For such constructive interference, X-Ray beams will be diffracted by the atoms of a crystal structure, as shown in figure 5.2. Assuming that we have a plane wave of monochromatic X-rays with a wavelength λ which is incident on a crystal surface at an angle θ, the incident rays will be scattered by the atoms in the crystal at the same angle θ as shown in figure 5.2. The rays scattered from the next row of atoms will travel slightly longer distances, which depends on the spacing between the rows and the incident angle [16].

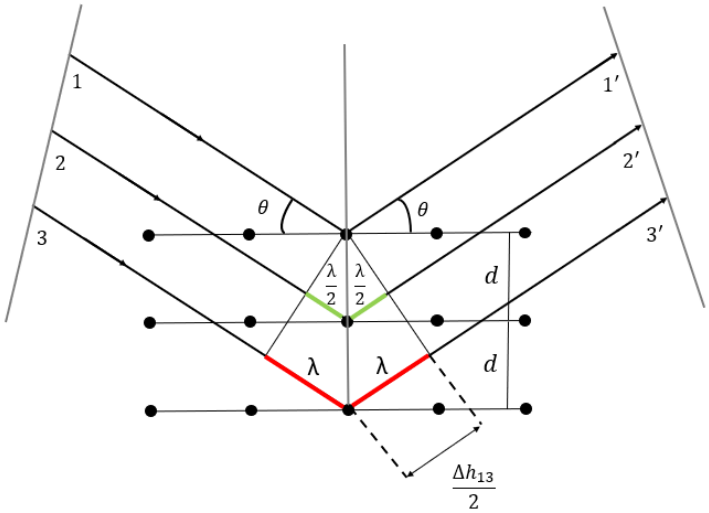

Figure 5.2: X-Ray beams scattered from parallel planes of a crystal. Rays 1,2 and 3 are incident on the crystal with an angle θ. Rays 1', 2' and 3' scattered from the crystal with the same angle.

The path difference between the x-ray beams is given by

$$\begin{aligned} \Delta h_{12} &= 2d\ sin(\theta) \\ \Delta h_{13} &= 4d\ sin(\theta) = 2\ \Delta h_{12} \\ \Delta h_{23} &= 2d\ sin(\theta) = \Delta h_{12} \end{aligned} \tag{5.1}$$

where Δh_{ij} is the path difference between ray i and j, and d is the spacing between the planes of atoms. For any two rays to interfere constructively, the path difference between them has to be equal to λ or an integral number of the wavelength, nλ. When such conditions are met, these rays will interfere constructively, and the signal will be enhanced at the detector. The constructive interference between rays will happen at an angle given by

$$n\lambda = 2d\ sin(\theta) \tag{5.2}$$

which is known as Bragg's Law. The angle θ, which is known as the Bragg angle, depends on the spacing between the atomic planes and the radiation wavelength, for which the condition is fulfilled. Therefore, for a given wavelength, the plane spacing (d) of a crystal structure can be measured by finding the Bragg angle.

For larger angles θ, the constructive interference can take place, as long as the path difference Δh_{ij} is an integer multiple of the wavelength λ. The Bragg angle θ at which the diffraction from a particular set of parallel planes takes place in a crystal lattice can be calculated from

$$\theta = arcsin\left(\frac{\lambda}{2d_{hkl}}\right) \tag{5.3}$$

where d_{hkl} is the interplanar spacing between a specific set of planes. As mentioned before in the theory chapter, (hkl) are the Miller indices of a certain family of planes in a crystal. Each crystal structure from the Bravais lattices has a different equation to calculate the interplanar spacing d_{hkl} for a particular (hkl) planes. For example, if the crystal structure is an orthorhombic crystal, the interplanar spacing is given by

$$\frac{1}{d_{hkl}^2} = \left(\frac{h}{a}\right)^2 + \left(\frac{k}{b}\right)^2 + \left(\frac{l}{c}\right)^2 \tag{5.4}$$

where a and b are the in-plane lattice parameters, and c is the out-of-plane lattice parameter for an orthorhombic crystal. If the structure is reduced to a tetragonal crystal, a and c lattice parameters only will remain, and the interplanar spacing equation will be reduced to

$$\frac{1}{d_{hkl}^2} = \frac{h^2 + k^2}{a^2} + \frac{l^2}{c^2} \tag{5.5}$$

where a is the in-plane lattice parameter, and c is the out-of-plane lattice parameter of the tetragonal structure. For a cubic lattice crystal, the equation of d_{hkl} will have only the lattice parameter a.

5.2.1 Different scan techniques in HRXRD

The scattered X-ray intensity is always measured as a function of Omega and/or 2-theta in the HRXRD. As mentioned before, Omega (ω) is the incident angle, and 2-Theta (2θ) is the diffracted angle, which is the angle between the incident beam and detector. The vector K is known as the diffraction vector and is perpendicular to the plane at which the diffraction occurs. These parameters are shown in figure 5.1. There are three types of scans which are typically used [63]:

- Rocking curve is a plot of x-ray intensity as a function of Omega.
- Detector scan is a plot of x-ray intensity as a function of 2-Theta without changing Omega.
- Coupled scan is a plot of scattered x-ray intensity as a function of 2-Theta with changing Omega. Nevertheless, the changing of Omega is connected with the 2-Theta changing.

Defects in crystals like dislocations, misorientation, mosaic spread, and curvature can be studied using Rocking curves. Additionally, Rocking curves are a good scan approach to be used with lattice-matched thin films to study layer thickness, strain, ternary composition, and relaxation [9]. A coupled scan can be used to determine the Bragg diffraction angle. In coupled scans, the Bragg peak position could be changed as a result of lattice mismatch or change in composition. For a detailed analysis of the layer thickness, superlattice period, and composition, multiple coupled scans will be required. Reciprocal space mapping is the best approach to be used, to get a full amount of necessary information for the analysis of strained films, which is explained later in this chapter. For the measurements of different crystallographic directions, the sample should be tilted to determine the Bragg peak positions. For a symmetric scan, the Omega angle must be equal to the Theta angle. Thus, the diffraction vector K will be orthogonal to the sample surface, such as [004] symmetric scan. For an asymmetric scan, the sample must be tilted about Theta angle, where 2-Theta should be equal to twice the Omega angle plus or minus the tilt such as [115] asymmetric scan. There are two ways to tilt the sample, the first method is to tilt the sample towards a lower omega value which is called Grazing incidence $(-)$, and the second approach is to tilt the sample towards a higher omega value which is called Grazing exit $(+)$. The symmetric and different asymmetric scans configurations are shown in figure 5.3 [63, 9].

During Omega-2Theta coupled scan, the diffraction vector does not change because of Omega and 2-theta change in coupled means. Therefore, the plane direction under measuring will not change during the scan. The interplanar spacing (d) is determined from the Bragg peak position. Composition, strain or relaxation can change the lattice parameter of the unit cell of crystal layer, which can also be determined from the change in peak position in a coupled scan. In case that the composition and lattice parameters of a particular crystal layer are unknown, multiple coupled scans in symmetric and asymmetric reflection directions are required to calculate both values. The layer thickness can be measured from the width of the Bragg peak of the layer. In addition, the distance between interference fringes can be another method to quantify the layer thickness.

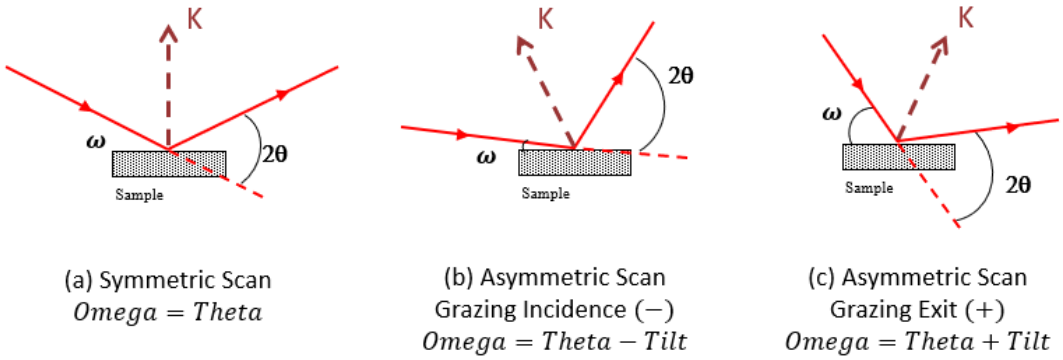

Figure 5.3: The symmetric and asymmetric scans configurations. (a) Shows the symmetric scan while (b) and (c) show asymmetric grazing incidence and asymmetric grazing exit scans, respectively. Reprinted from [63].

High-Resolution X-Ray Diffraction has two instrumental configurations, double-axis, and triple-axis configurations. The difference between the two experiments is shown in figure 5.4. The detector surface is relatively large unless a collimator is used with it. It may not distinguish between different 2-Theta diffraction angles; therefore, the peaks from different layers can be seen in the rocking curve by using this approach. The incident angle is changing by the rotation of the sample around its omega axis, and the x-ray intensity is

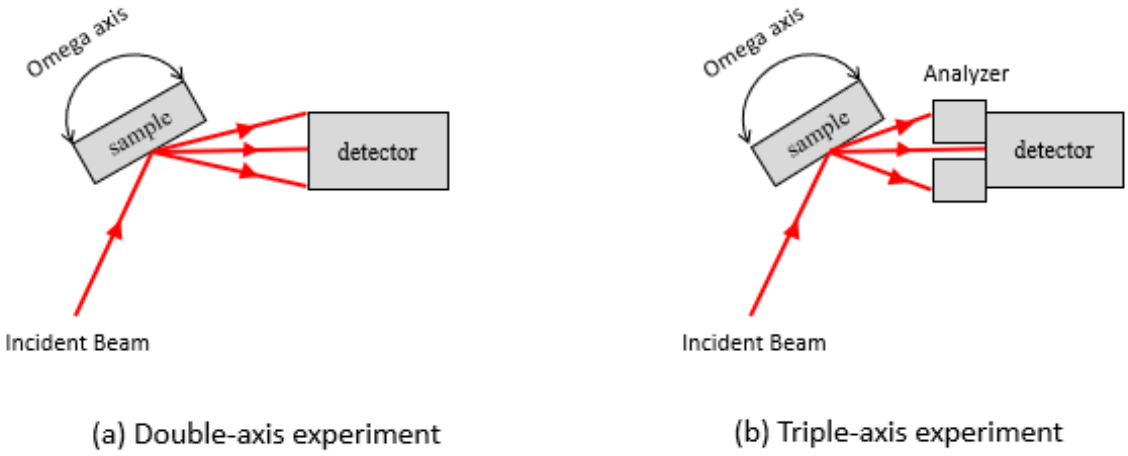

Figure 5.4: High Resolution X-Ray Diffraction (a) double-axis experiment and (b) triple-axis experiment. Reprinted from [63].

produced as a function of Omega in the double-axis experiment. A slit or analyzer crystal is used in the triple-axis experiment to restrict the angular detector acceptance. The most common scan used with the triple-axis experiment is the coupled scan as the detector is rotated at twice the rate of rotating the sample about the Omega axis producing a coupled Omega-2Theta scan. The analyzer in the triple-axis experiment constrains the detector to just one 2-Theta angle corresponding to a particular material layer. Typically, even for fully elastically strained layers, the Bragg peaks in the triple-axis experiment have a smaller peak width than in the double-axis experiment of the same layer [80, 9].

5.2.2 Reciprocal Space Map

Reciprocal Space Map (RSM) collects many Omega-2Theta coupled scans as a function of the sample tilt (Omega). First, the definition of the reciprocal lattice will be explained through mathematical statements. By using the axes of the direct lattice from figure 2.1, the reciprocal lattice vectors are given by [26]

$$\begin{aligned} \vec{a^*} &= 2\pi \frac{\vec{b} \times \vec{c}}{\vec{a} \cdot \vec{b} \times \vec{c}} = 2\pi \frac{\vec{b} \times \vec{c}}{V} \\ \vec{b^*} &= 2\pi \frac{\vec{c} \times \vec{a}}{\vec{a} \cdot \vec{b} \times \vec{c}} = 2\pi \frac{\vec{c} \times \vec{a}}{V} \\ \vec{c^*} &= 2\pi \frac{\vec{a} \times \vec{b}}{\vec{a} \cdot \vec{b} \times \vec{c}} = 2\pi \frac{\vec{a} \times \vec{b}}{V} \end{aligned} \tag{5.6}$$

where $\vec{a^*}$, $\vec{b^*}$ and $\vec{c^*}$ are the reciprocal axis vectors, and V is the corresponding volume of the unit cell in direct space, these vectors are shown in figure 5.5. Additionally, by using these reciprocal axes vectors scalar products with the real angles α, β, and γ used in the direct lattice, the reciprocal angles α^*, β^*, and γ^* can be calculated. The calculations of these angles can be found in this Ref. [26]. It can be seen that a reciprocal unit cell can be defined with $\vec{a^*}$, $\vec{b^*}$ and $\vec{c^*}$ axes as well as each reciprocal lattice point represents a set of parallel planes. Therefore, a three-dimensional network of points indicated by the Miller indices hkl can be constructed for all possible planes, as shown in figure 5.5. Reciprocal lattice vector g_{hkl} is the vector drawn from the origin 000 of the reciprocal unit cell lattice to a particular reciprocal lattice point hkl, and it is perpendicular to the parallel planes with the same hkl indices. Reciprocal lattice vector g_{hkl} which is also known as the scattering vector is defined as

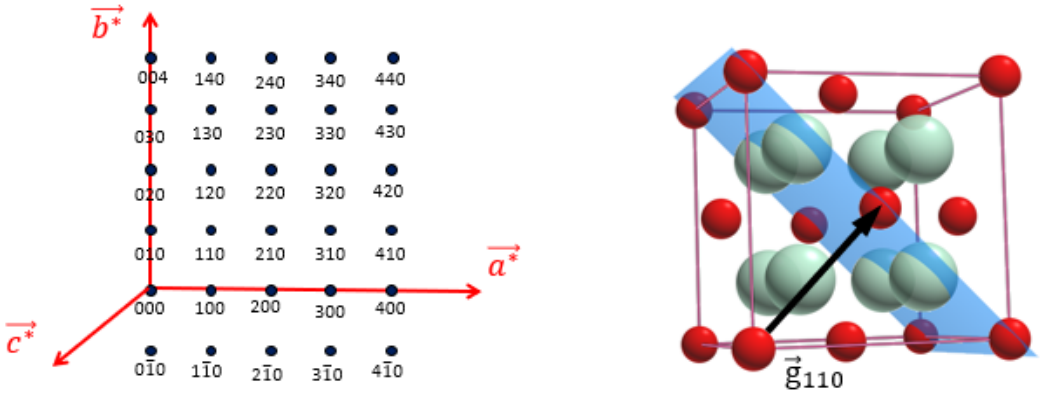

(a) Reciprocal axis vectors

(b) Reciprocal vector $\vec{g}_{110}$

Figure 5.5: The reciprocal lattice space configuration. (a) shows the reciprocal axis vectors $\vec{a^*}$, $\vec{b^*}$ and $\vec{c^*}$. (b) Interplanar reciprocal space vector g_{110} for the set of planes (110). Reprinted from [63].

$$\mathbf{g}_{hkl} = \frac{1}{d_{hkl}} = ha^* + kb^* + lc^* \tag{5.7}$$

Reciprocal Space Maps (RSMs) are collected using several scans because some effects like strain can shift the reciprocal lattice points, making it impossible to collect the data with only one scan. The Omega-2Theta coupled scans of the RSMs are collected at different Omega offsets, where 2-Theta angle will be equal to twice Omega angle minus the offset. Thus, 2-Theta is moving at twice the rate as the rotation of the sample. It can allow the measurement of diffuse scattering and separate the effects of strains and tilts. Additionally, with these multiple scans in the RSM, the epitaxial layer and substrate peaks can be observed in the data collected.

A set of planes can be examined by reciprocal space if they are oriented in a specific direction. It can be explained by the Ewald sphere, which has been used to observe the construction of a diffraction pattern from a crystal. Ewald sphere was introduced by Paul Ewald in 1912, who also showed the reciprocal lattice [21]. The formation of the Ewald sphere is shown in figure 5.6. From this figure, it can be seen that, if we have radiation beam **A** diffracted by a set of planes in the sample where the diffracted beam is denoted by **R**. Then, constructing a sphere where its center is at the meeting point of the incident

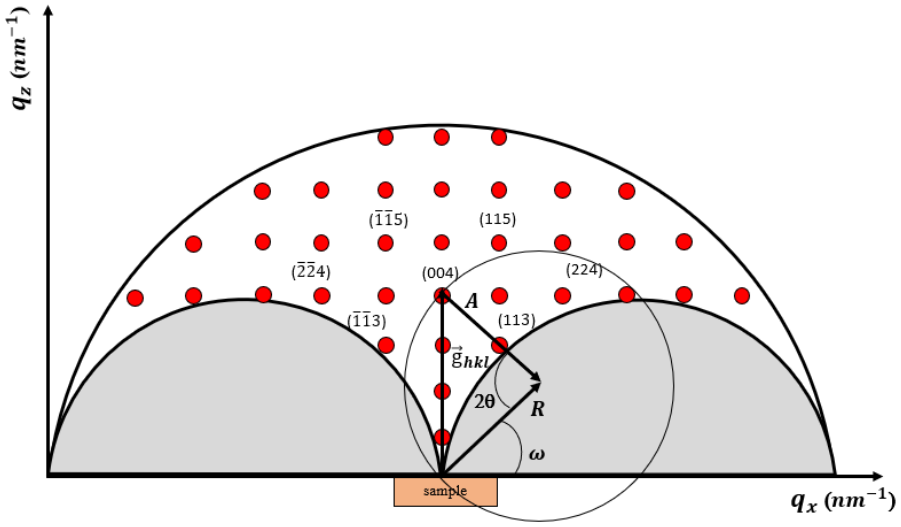

Figure 5.6: Ewald sphere configuration. $\mathbf{g}_{\mathrm{hkl}}$ is the reciprocal lattice vector or scattering vector, A is the incident beam and R is the diffracted beam.

and diffracted beam and the circumference of the sphere is at the sample surface. It is the so-called sphere of reflection or Ewald sphere. The incident and diffracted beams will have a 2-Theta angle in between and meet the reciprocal lattice vector $\mathbf{g}_{hkl}$ at the same point as the circumference meets the sample which perpendicular to a set of planes with the same hkl indices. Suppose that the intersection point happens to meet with the reciprocal lattice point hkl for the set of planes, and the result is a right-angled triangle [26]. Therefore, we can get the Bragg's law as

$$sin(\theta) = \frac{\mathrm{g}_{hkl}}{4\pi\lambda} = \frac{\lambda}{2d_{hkl}} \tag{5.8}$$

where λ is the radiation wavelength. It means that the Bragg's law is obeyed when a reciprocal lattice point is found on the surface of the Ewald sphere and the diffracted beams from the crystal will be at an angle 2θ. On the other hand, any reciprocal lattice point that does not lie on the Ewald sphere, then the diffraction will not occur because the set of planes are not in the correct orientation. It can be seen from figure 5.6 that the d-spacing can be found from the position in q_z of the peak, and the tilt of planes can be found from q_x position of the peak. To separate between the tilts and strain, a symmetric reciprocal space map should be used. However, to separate between composition/mismatch and strain, an asymmetric reciprocal space map is needed. The reciprocal lattice units q_x

and q_z, which are shown in figure 5.6, presenting a reciprocal space map can be calculated from

$$q_x = q_{\parallel} = \frac{2}{\lambda} sin(\theta) cos(\phi)$$
$$q_z = q_{\perp} = \frac{2}{\lambda} sin(\theta) sin(\phi) \tag{5.9}$$

where θ is the angle of incidence, and ϕ is the tilt angle of a set of planes with respect to the crystal surface.

A comparison between (a) a 100% strained and (b) a 100% relaxed layers in reciprocal space maps is shown in figure 5.7. The relaxed layer has a cubic crystal ($a_{\perp}^{L}$=$a_{\parallel}^{L}$); therefore, both its in-plane and out-of-plane reciprocal space coordinates differ from that of the substrate. The diffraction orders are shifted both vertically and horizontally with respect to the substrate. For a strained layer, the in-plane lattice constant of the layer is equal to that of the substrate. Therefore, their in-plane reciprocal space coordinates are the same, and the diffraction orders of the layer are shifted only vertically with respect to those of the substrate. Depending on the degree of relaxation, the diffraction peak of the layer will appear anywhere between the two extremes shown in figure 5.7. More details about the Ewald sphere and reciprocal space mapping can be found in these references [26, 80, 9, 22].

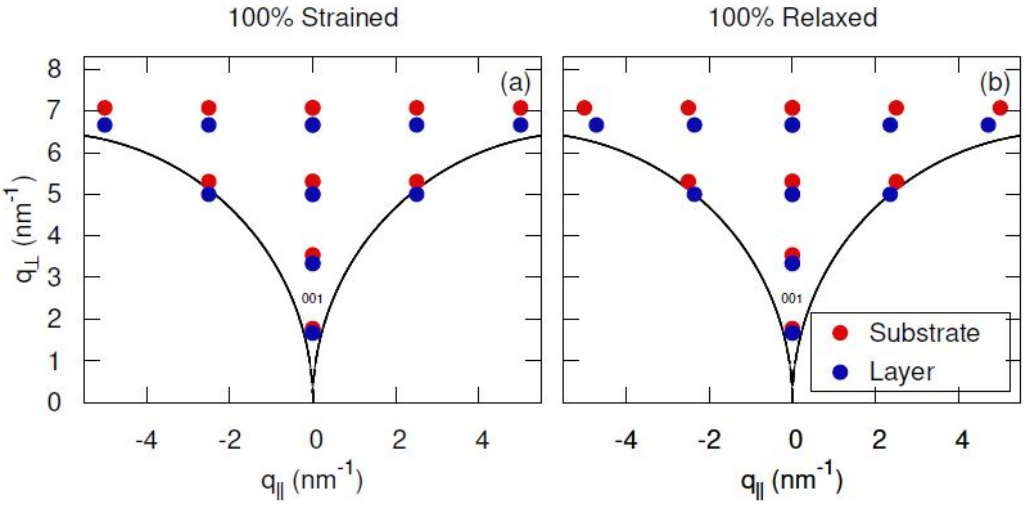

Figure 5.7: Comparison between (a) a 100% strained and (b) a 100% relaxed layers deposited on a particular substrate using reciprocal space lattice.

InAs cap 2nm
$Al_{0.8}Ga_{0.2}Sb$ barrier 20nm
InAs QW 24nm
$Al_{0.8}Ga_{0.2}Sb$ barrier 20nm
$Al_{0.8}Ga_{0.2}As_{0.07}Sb_{0.93}$ buffer 800nm
GaSb buffer 25nm
GaSb undoped (001)

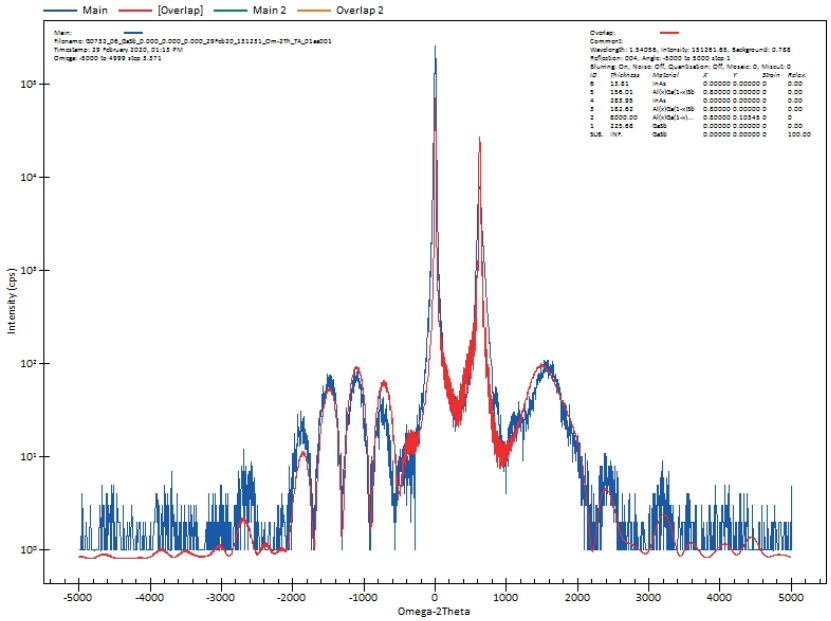

Figure 5.8: Figure (a) shows the material structure under diffraction. (b) Symmetric coupled Omega-2Theta scan around the GaSb (004) diffraction peak using Triple-axis configuration, it shows the Omega-2Theta (x-axis) as a function of x-ray intensity (y-axis). The scan was taken from -5000 to 5000 arcsecs range to include all layers in the structure.

5.2.3 HRXRD of heteroepitaxial layers

We have seen before that it is possible to grow layers of different III/V materials on top of each other. These materials can be distinguished in HRXRD, as they show different diffraction peaks at different Bragg angles due to their different lattice parameters. A symmetric scan (004) around the GaSb (004) reflection is shown in figure 5.8. It shows a coupled Omega-2Theta scan in 004 direction of our InAs/AlGaSb material structure, which is also shown in the same figure 5.8. The peak with the highest intensity indicates the GaSb substrate; the first peak to the right of the substrate peak is due to a layer of quaternary buffer $Al_xGa_{1-x}As_ySb_{1-y}$ with thickness 800nm. From the analysis of this scan, it can be seen that the quaternary buffer layer is under tensile strained because its lattice constant is smaller than that of the substrate. The rest of the peaks with a lower intensity due to their small thicknesses correspond to the rest of the material layers in the structure, which are $Al_{0.8}Ga_{0.2}Sb$ for lower and upper barriers, and InAs for the quantum well and cap layers.

The lattice constant of the ternary and quaternary alloys depends on the composition of the materials. In our material system, the quaternary buffer $Al_xGa_{1-x}As_ySb_{1-y}$ is used. As seen before that this buffer layer can be lattice-matched to the GaSb substrate by controlling the composition of materials in the buffer, especially group five materials Arsenic (As) and Antimony (Sb). Therefore, measuring the lattice constant can provide information on the composition of a layer. The As amount can be measured for each sample, and then by relating this As amount with the As flux measured by BFM during the growth of the buffer layer, we can detect the exact As flux corresponding the 7% of As in the quaternary buffer. Since the quaternary buffer with these material compositions $Al_{0.8}Ga_{0.2}As_{0.07}Sb_{0.93}$ will be lattice-matched to the GaSb substrate, this means its in-plane lattice constant $a_{\parallel}^{L}$ is equal to the lattice constant of the substrate a_0^s. If the As amount in the buffer is greater than 7% by a small amount, the buffer layer will be under tensile strain. In this case, the in-plane lattice constant $a_{\parallel}^{L}$ is strained to match the lattice constant of the substrate a_0^S. Thus, its out-of-plane lattice constant $a_{\perp}^{L}$ got shrunk to compensate for the tensile strain induced in the buffer layer. On the other hand, if the As amount in the buffer is less than 7% by a small amount, the buffer layer will be under compressive strain. The in-plane lattice constant $a_{\parallel}^{L}$ of the buffer layer is compressed to match the lattice constant of the substrate a_0^s. Therefore, its out-of-plane lattice constant $a_{\perp}^{L}$ got stretched to compensate for the compressive strain induced in the buffer layer. To measure the in-plane and the out-of-plane lattice constants of the buffer in all samples, a symmetric RSM (004) scan, and an asymmetric RSM (115) scan was taken for each sample.

5.3 Stiffness coefficients and Poisson's ratio of the Quaternary buffer $Al_xGa_{1-x}As_ySb_{1-y}$

In the theory chapter, equations 2.11 and 2.10 were introduced. These equations have two unknowns the native lattice constant of the buffer and its Poisson's ratio. The stiffness coefficients depend on the compositions of the materials in the alloy; therefore, they were calculated here as a function of As composition (y). Thus, equation 2.11 can be written as a function of As composition (y), and by using the native lattice constant of the quaternary buffer in Vegard's law, we will end up with one equation has only one unknown which is the As composition (y). For a given alloy-substrate system, the two composition parameters of a quaternary alloy allow the energy band gap E_g and lattice parameter a to be selected independently. An interpolation scheme is used in our model, and it is based on using the material parameters of binaries related to the quaternary alloy used here. Therefore, we started with the binaries constituent then gradually moved on to alloys. During

Parameter	GaSb	$Al_xGa_{1-x}As_ySb_{1-y}$	$Al_{0.8}Ga_{0.2}As$
Elastic stiffness constant C_{ij} $(X10^{11} dyn/cm^2)$			
C_{11}	8.838	8.838+3.154y	11.992
C_{12}	4.027	4.027+1.609y	5.636
C_{44}	4.320	4.32+1.58y	5.9

Table 5.1: Elastic parameters for $Al_xGa_{1-x}As_ySb_{1-y}$ lattice matched to GaSb and elastic parameters of $Al_xGa_{1-x}As$ at 300 K.

the epitaxial growth of these alloys, the structural, electronic, and mechanical properties of semiconductor alloys are modified because spontaneous ordering happens during the growth, which can be classified as a self-organized process [3]. The quaternary material $A_xB_{1-x}C_yD_{1-y}$ is thought to be constructed from four binaries: AC, AD, BC, and BD. By using this linear interpolation scheme, the quaternary parameter $Q(x, y)$ can be derived from the Binaries as [3]

$$Q(x,y) = xyB_{AC} + x(1-y)B_{AD} + (1-x)yB_{BC} + (1-x)(1-y)B_{BD} \tag{5.10}$$

where Q(x,y) represents the quaternary parameter which can be the lattice constant, the energy bandgap of the alloy or stiffness coefficients, x, and y are the compositions of the materials, and B_{ij} represents the binary alloys from which the quaternary alloy is formed. As we have seen before, the lattice constant a obeys Vegard's law well, which means that it varies linearly with composition. Therefore, if we know the native lattice constant of the quaternary buffer, we can get y composition from equation 5.11 if x composition is known. There are many studies about the elastic properties of the III–V binaries; however, there is a lack of information about their alloys. Some recent studies suggested that the elastic properties of alloys can be obtained by averaging the binary endpoint values [39, 32]. By using this method, the elastic stiffness C_{ij} and compliance constants S_{ij} for some III–V ternary and quaternary alloys with zinc blende and wurtzite structures were calculated with a good approximation in [1, 2, 3] by using equation 5.11. The stiffness coefficients C_{ij} for quaternary buffer $Al_xGa_{1-x}As_ySb_{1-y}$ is calculated by using the same interpolation scheme that was used before for $In_{1-x}Ga_xAs_yP_{1-y}$ by S. Adachi in [1]. The results of these calculations are shown in table 5.1. The stiffness coefficients C_{ij} of the ternary alloy $Al_{0.8}Ga_{0.2}As$ in table 5.1 were calculated from [3]

$$T(x) = xB_{AC} + (1-x)B_{BC} \tag{5.11}$$

Binary materials	lattice parameter ($\mathring{A}$)
GaSb	6.0959
GaAs	5.6533
AlSb	6.1355
AlAs	5.6614

Table 5.2: Lattice parameters for binary materials

By substituting the stiffness coefficients from table 5.1 in equation 2.10 we can get the Poisson's ratio as a function of As composition y. Then, substituting the Poisson's ratio in equation 2.11, it will be a function of As composition y. Finally, we have Vegard's law for the native lattice constant as a function of y by substituting the binary lattice parameters from table 5.2 in equation 5.11 as

$$a_{Al_{0.8}Ga_{0.2}As_ySb_{1-y}} = (0.8)yB_{AlAs} + (0.8)(1-y)B_{AlSb} + (0.2)yB_{GaAs} + 0.2(1-y)B_{GaSb} \tag{5.12}$$

where $a_{Al_xGa_{1-x}As_ySb_{1-y}}$ is the nattive lattice constant of this quanternary alloy and B_{ij} is the lattice constant of the corresponding binary alloy. After simplification,

$$a_{Al_{0.8}Ga_{0.2}As_ySb_{1-y}} = 6.1276 - 0.4678y \tag{5.13}$$

Finally, we have two equations as a function of As composition y, which are equations 2.11 and 5.13 and only one value of y will satisfy both equations so that we can solve them together to get y. The only remaining parameters we need to find in order to calculate the As composition y are in-plane ($a_{\parallel}$) and out-of-plane ($a_{\perp}$) lattice parameters of the quaternary buffer layer grown on the GaSb substrate. These lattice parameters are found experimentally from (004) symmetrical RSM and (115) asymmetric RSM. From the (004) symmetric map, the lattice mismatch in the (001) growth direction can be deduced by [14]

$$\left(\frac{\Delta a}{a_0^S}\right)_{\perp} = -\frac{\Delta q_z^{004}}{\frac{4}{a_0^S} + \Delta q_z^{004}} \quad where, \left(\frac{\Delta a}{a_0^S}\right)_{\perp} = \left(\frac{a_{\perp} - a_0^S}{a_0^S}\right) \tag{5.14}$$

where Δq_z^{004} is the peak splitting measured in [004] direction, and a_0^S is the substrate lattice parameter. A 90° rotation of the sample ([110] and $[1\bar{1}0]$) would give the same results. The parallel lattice mismatch measured along [110] or $[1\bar{1}0]$ is given by

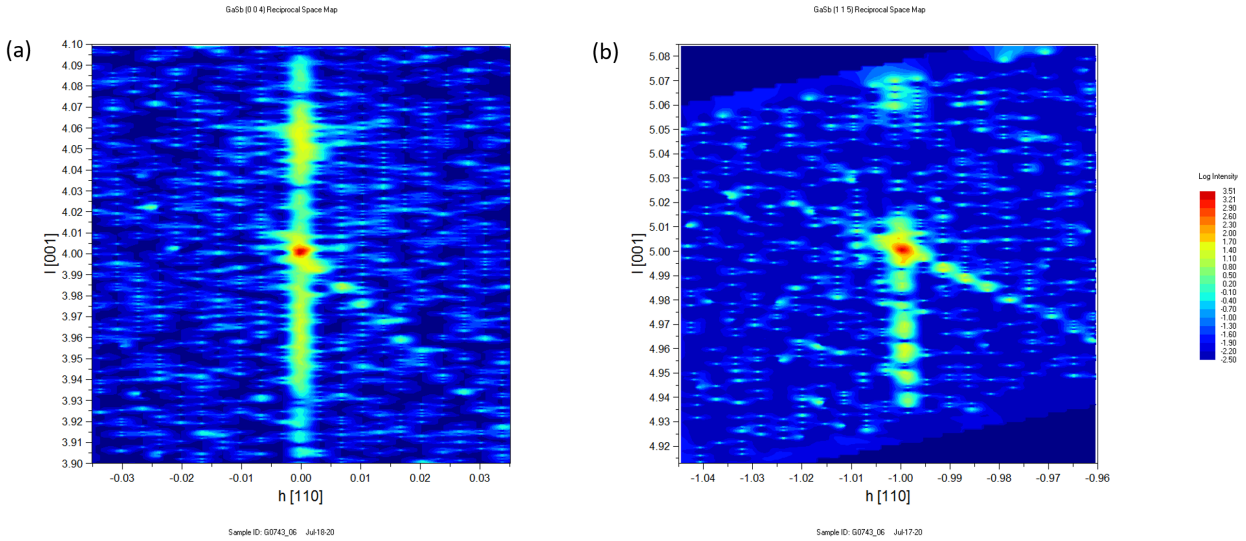

Figure 5.9: The symmetric and asymmetric scans of a sample ID G0743, Triple-axis approach were used in these scans (a) shows the (004) RSM in and (b) shows the (115) RSM in hkl units

$$\left(\frac{\Delta a}{a_0^S}\right)_{\parallel} = -\frac{\Delta q_x^{115}}{\frac{\sqrt{2}}{a_0^S} + \Delta q_x^{115}} \quad where, \left(\frac{\Delta a}{a_0^S}\right)_{\parallel} = \left(\frac{a_{\parallel} - a_0^S}{a_0^S}\right) \tag{5.15}$$

where Δq_x^{115} is the peak splitting measured on [115] RSM in the <110> directions.

5.4 Calculations of the lattice parameters and Arsenic composition

In this section, the calculation results of lattice parameters and As compositions of the quaternary buffer layers in some samples are presented. All the sans in this study were taken by the QC3 High-Resolution Diffractometer developed by Jordan Valley Semiconductors UK Ltd. An example of the symmetric (004) and asymmetric (115) reciprocal space map scans taken for one of our samples are shown in figure 5.9. In this study, all the (115) RSM was taken using the Glancing Incidence configuration. This sample (G0743) has the structure of the same material as the one shown in figure 5.8. In both scans, the red

Sample ID	out-of-plane lattice parameter ($\AA$)	in-plane lattice parameter ($\AA$)
G0679	6.1085	6.09591
G0683	6.1088	6.09574
G0695	6.0663	6.09599
G0702	6.0924	6.09578
G0703	6.1005	6.09519
G0732	6.0642	6.09601
G0737	6.0719	6.09601
G0738	6.0907	6.09598
G0743	6.0934	6.09593
G0745	6.1055	6.09519

Table 5.3: Calculated lattice parameters of the buffer layer in different growths. First column is showing the sample ID and second and third columns are showing the out-of-plane lattice parameters and the in-plane lattice parameters of each buffer layer, respectively.

regions represent the Bragg peaks from the substrate and the buffer layer. In both (004) and (115) RSMs, the peaks of the substrate and the buffer layer are overlapped, which indicates lattice matching between the layer and the substrate, and the 7% is successfully achieved in the quaternary buffer in this sample. The yellow peaks shown in both scans indicate smaller x-ray diffraction intensity; these peaks correspond to the rest of the layers in the materials' structure under diffraction. The results of lattice parameters calculations for ten samples, having the same material structure, are shown in table 5.3. As previously mentioned, after calculating the in-plane and out-of-plane lattice parameters of the quaternary buffer, equation 5.13 and 2.11 are used to estimate the As composition in each buffer layer, the results are shown in table 5.4. If the As amount in the buffer layer is less than 7%, the compressive strain will be induced in the buffer layer. Furthermore, if the As amount in the buffer layer is greater than 7%, the tensile strain will be induced in the buffer.

Threading dislocations can be formed as a result of the induced strain in the buffer layer leading to a decrease in carrier mobility of the Quantum well due to different scattering mechanisms, and also they can introduce parallel conduction channels in the buffer layer. Therefore, our target here is to achieve an Arsenic composition in the quaternary buffer as close as possible to 7%. The As amount is then related to its corresponding As flux measured during the growth of the buffer layer, then by linear regression of these dependent variables was done. From this linear regression, the exact As flux that will achieve the 7% As composition in the quaternary buffer can be calculated. The process started by

Sample ID	As composition (y)
G0679	5.5 %
G0683	5.4 %
G0695	9.9 %
G0702	7.3 %
G0703	6.4 %
G0732	10.2 %
G0737	9.4 %
G0738	7.5 %
G0743	7.0 %
G0745	5.7 %

Table 5.4: Calculated As composition y in the quaternary buffer of each growth.

growing a calibration growth to estimate the As flux range that will achieve the 7% As. The structure of this growth and its reciprocal space map are shown in figure 5.10. The first layer of this structure is a 25nm of GaSb, which is a smoothing layer, then four different quaternary buffer layers were grown with thickness 500nm each. Finally, the structure ended up with a 5 nm cap layer of GaSb. Different As fluxes were used for each quaternary buffer. Then, by finding the As amount in each layer and related to the As flux, we were able to find an estimated value of the As flux that will achieve the 7% of As in the quaternary buffer. From using the symmetric 004 RSM and the asymmetric 115 RSM, the lattice parameters were found, and the As amount was calculated for each buffer layer in the structure, the calculation results are shown in table 5.5. After that, the As amount is related to the As flux measured during the growth, the data measured is shown in table 5.6. Using linear fitting of the four data points of the As flux and As amount in each layer, the As flux corresponds to the 7% was found to be 1.84×10^{-8} Torr. The next step was to grow the main material structure in figure 5.8 and use the As flux found from the calibration growth during the growth of the quaternary buffer in the main structure.

Four growths of the main structure were done after the calibration growth in order to achieve the 7%. The first growth after the calibration growth was not successful in achieving the 7% of As amount, and it had a 10.21% of As. The As flux was decreased for the second growth, but it had 9.45% of As. The third growth was successful with decreasing the As flux more, and it had 7.45% of As. A linear fitting was done from these three growths to estimate the most accurate As flux that will achieve the 7% of As. This linear regression is shown in figure 5.11. Moreover, the data of the first three growths used in the linear regression is shown in table 5.7. The linear equation of the fitting line is

GaSb cap 5nm
$Al_{0.8}Ga_{0.2}As_ySb_{1-y}$ buffer 500nm
$Al_{0.8}Ga_{0.2}As_ySb_{1-y}$ buffer 500nm
$Al_{0.8}Ga_{0.2}As_ySb_{1-y}$ buffer 500nm
$Al_{0.8}Ga_{0.2}As_ySb_{1-y}$ buffer 500nm
GaSb buffer 25nm
GaSb undoped (001)

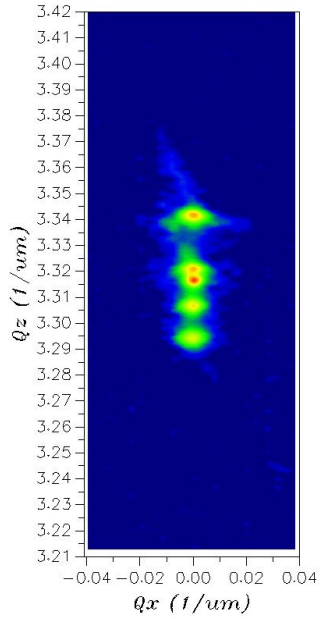

Figure 5.10: The material structure of the calibration growth with the symmetric 004 reciprocal space map from which the lattice parameters were calculated with the 115 reciprocal space map.

$Al_{0.8}Ga_{0.2}As_ySb_{1-y}$	$a_{\parallel}$ Å	$a_{\perp}$ Å
First Layer	6.0961	6.1427
Second Layer	6.0956	6.1122
Third Layer	6.0957	6.0899
Fourth Layer	6.0889	6.0578

Table 5.5: The lattice parameters of the calibration growth.

$$y = (1.3264 \times 10^{-6}) \quad x \tag{5.16}$$

where y represents the As flux needed, and x represents the corresponding As amount. By replacing x by the 0.07, the As flux was found. By using this As flux in the fourth growth with sample ID G0743, we succeeded in achieving a 7% of As amount in the buffer, as shown in table 5.4. The results of the out-of-plane and in-plane lattice parameters are shown in table 5.3. This procedure was followed for all samples to achieve the 7% of As

$Al_{0.8}Ga_{0.2}As_ySb_{1-y}$	As composition (y)	As flux (Torr)
First Layer	1.5 %	4.85E-09
Second Layer	4.8 %	1.35E-08
Third Layer	8.5 %	2.07E-08
Fourth Layer	13.3 %	4.95E-07

Table 5.6: The Arsenic amount in each layer of the calibration growth and the corresponding Arsenic flux.

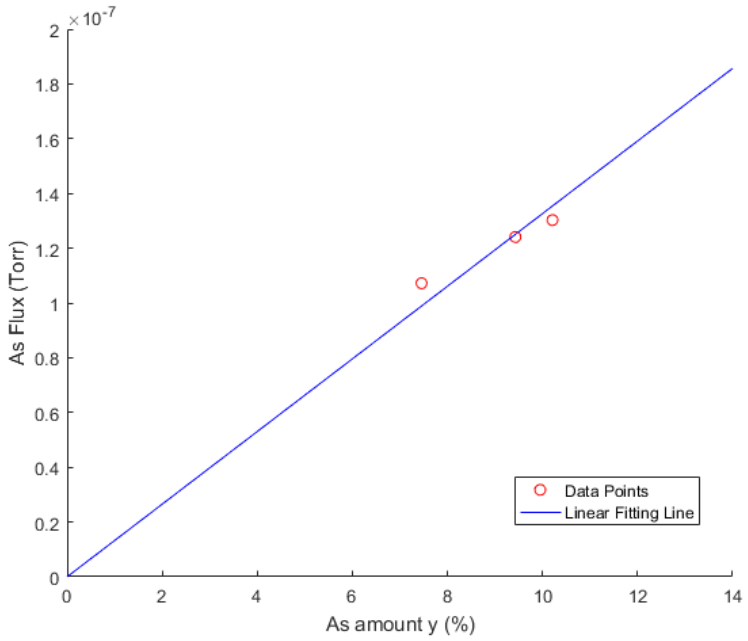

Figure 5.11: The linear regression of the data for the three growths G0732, G0737 and G0738.

for all samples.

In conclusion, by using the X-ray diffraction model introduced in this chapter, the 7% of As was achieved in the quaternary buffer $Al_xGa_{1-x}As_ySb_{1-y}$. The procedure started by finding the lattice parameters of the quaternary buffer layer. Then, the As composition was calculated in each buffer layer for all samples. Then, by finding the relation between the As amount and As flux measured during the growth of the buffer layer, we managed to estimate the As flux needed to achieve the 7% of As and achieve the lattice-matched

Growth Number	As composition (y)	As flux (Torr)
G0732	10.2 %	1.30E-07
G0737	9.4 %	1.24E-07
G0738	7.5 %	1.07E-07

Table 5.7: The data of the three growths G0732, G0737 and G0738 used in the linear regression.

condition between the GaSb substrate and the quaternary buffer layer. Upon achieving the 7% of As or close to 7%, the quaternary buffer will be lattice-matched to the substrate, and the dislocation density will be reduced. As the dislocation density decrease in the sample, the carrier mobility and density increase in the InAs quantum well. The effect of the As composition and strain on the carrier mobility and density is shown in the Hall measurements chapter. Simulations were performed to estimate the error in As composition calculations method introduced in this chapter. The main error in the calculated As composition comes from the uncertainty in group III fluxes during the growth of the quaternary buffer. Typical stability of group III fluxes during the growth is better than approximately $\pm 2\%$, which will result in an error on 'x' in $Al_xGa_{1-x}As_ySb_{1-y}$ of about ± 0.01. Induced by this change in strain will result in an error of calculated As composition 'y' of approximately ± 0.001, or $\pm 0.1\%$. Finally, we concluded that to have a quaternary buffer with As composition close to 7%, when other structures were grown in the chamber before returning to this project, we have to sacrifice two or three growths before achieving the target. The reason behind that is the small variations occur in the growth chamber condition over time, such as changes in the sticking coefficient of As to the chamber surfaces, due to coating by materials used in previous growths.

Chapter 6

Device design and fabrication

6.1 Introduction

Cleanroom processing for gated and un-gated devices was done with the collaborations of Ph.D. student Annelise Bergeron and Associate Prof. Francois Sfigakis from Prof. Jonathan's Baugh group. The fabricated inverted High Electron Mobility Transistors (HEMTs) are utilized in this work. Takashi Mimura was the first one to introduce the idea of High Electron Mobility Transistors in 1979 [49]. HEMT is described as a 2DEG falling between two semiconductor materials, having different bandgaps from the 2DEG material. The quantum well is usually buried away from the surface in HEMT. However, in the inverted HEMTs, quantum wells are located very close to the surface. Therefore, surface defects are a dominant factor in the inverted HEMTs, influencing the intrinsic electron mobility inside the quantum well. In this chapter, techniques used for fabricating our heterostructures into Hall bars are presented. All the samples fabricated in this project have the same materials' structure shown before in figure 4.1. The difference between samples fabricated is just the As mole fraction in the quaternary buffer.

6.2 Hall bar

6.2.1 Hall bar design

Fabrication processes of InAs heterostructures are well-developed, however it still open for further developments. The standard photo-lithography techniques have been used in hall

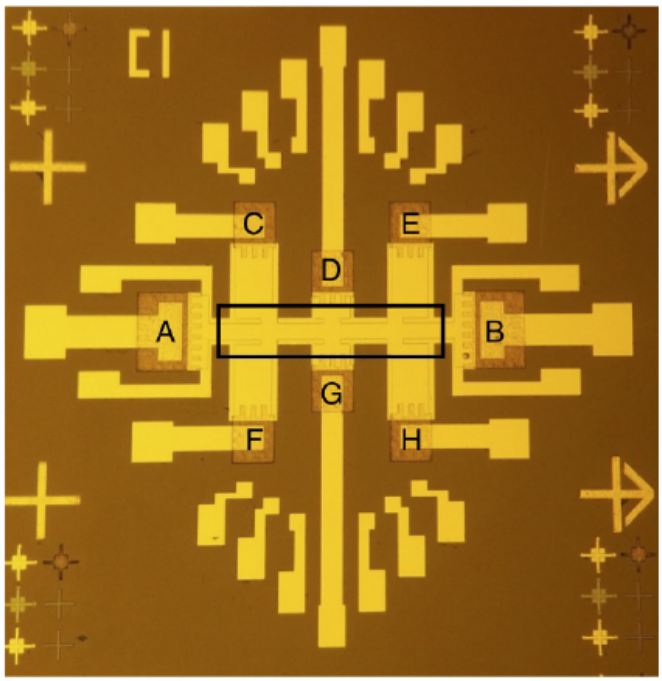

Figure 6.1: Gated Hall bar device taken by an optical microscope. Yellow colored regions are the Ti/Au deposition while orange colored regions the off-mesa etched regions. It consists 8 Ohmic contacts indicated by letters. The region in the black box is where the top gate is deposited. Printed with permission from Ref. [6].

bars fabrication. Different electrical properties of 2DEGs are measured using Hall bars, such as carriers mobility, charge density, and parallel conduction through the substrate. The design of our fabricated hall bar is shown in figure 6.1. Each side of the mesa has three lateral Ohmics denoted by different letters, while each end side of the mesa has only one Ohmic contact (A and B). An electric current is applied on the two end Ohmics to flow through the entire length of the hall bar. Using different combinations of the six lateral Ohmics during the voltage measurements, allow us to measure different electrical properties of the hall bar. The top gate is used to regulate the charge density in the 2DEG underneath by applying a voltage on its contacts. The main branch of the mesa is designed to have a specific length-to-width ratio for quantifying the 2DEG uniformity. In our Hall bar design, the length of the mesa is eight times its width. To ensure the uniformity of the 2DEG, the resistivity of each long side of the Hall bar should be equal to that of each half of the Hall bar. Therefore, it is better to have six lateral Ohmics instead of four to facilitate these measurements. In the case of different resistivity values

(non-uniform 2DEG), the most probable reason is the defects induced during fabrication or the impurities in the 2DEG. The carrier mobility and density of the wafer also could be affected by these impurities and fabrication defects. Sometimes a bad ohmic contact could be the reason for that; it can be very resistive and/or includes some reactance giving spatially non-uniform 2DEG. A top gate is deposited on top of an oxide layer known as the gate oxide, this layer is usually 40 nm of HfO_2 layer, to prevent the leakage between the metallic gate and the surface 2DEG. The deposition of the top gate takes place on the middle central part of the hall bar, as shown in figure 6.1. By applying a voltage to the top gate, the current density within the 2DEG can be controlled. Therefore, the carriers can be accumulated or depleted in the quantum well via applying different voltages to the top gate. Additionally, it is obvious from figure 6.1 that the hall bar consists of large Ti/Au bond pads off-mesa, to ensure easier device bonding to chip carriers, to which the Ohmic region of the hall bar is contacted.

6.2.2 Mesa fabrication

Photolithography techniques, dry and wet etching have been used in the fabrication of the mesa pattern. Typically, the first step in our fabrication process is cleaning the substrates using acetone and 2-propanol and then removing the native oxide using hydrofluoric acid. The first stage of the photolithography process is coating the sample with a photoresist using a spin coater. In the second stage, a photo-mask patterned with chrome is used for ultraviolet (UV) light exposure of the sample. Chrome material absorbs the UV light; thus, the areas below glass parts will be exposed to UV while the areas underneath the Chrome material will not. The UV light changes the structure of the hardened polymer, and it will be easily removed using a UV developer. Positive and negative photoresists have been used in our photolithography process. For the positive photoresist, the long-chain polymers in the resist exposed to UV light will be weakened, making the exposed parts of the resist easily dissolved and removed by UV developer. Contrarily, for the negative photoresist, the long-chain polymers in the resist exposed to UV light will be strengthened, and the exposed parts of the resist remain after washing by UV developer. For the mesa patterning a positive photoresist Shipley 1805 (S1805) is used for the photolithography process, the step by step process of defining a mesa pattern is shown in figure 6.2. Through our fabrication process, combinations of photoresists are used in order to have a bilayer of resist like what will be done in the Ohmic contacts fabrication process.

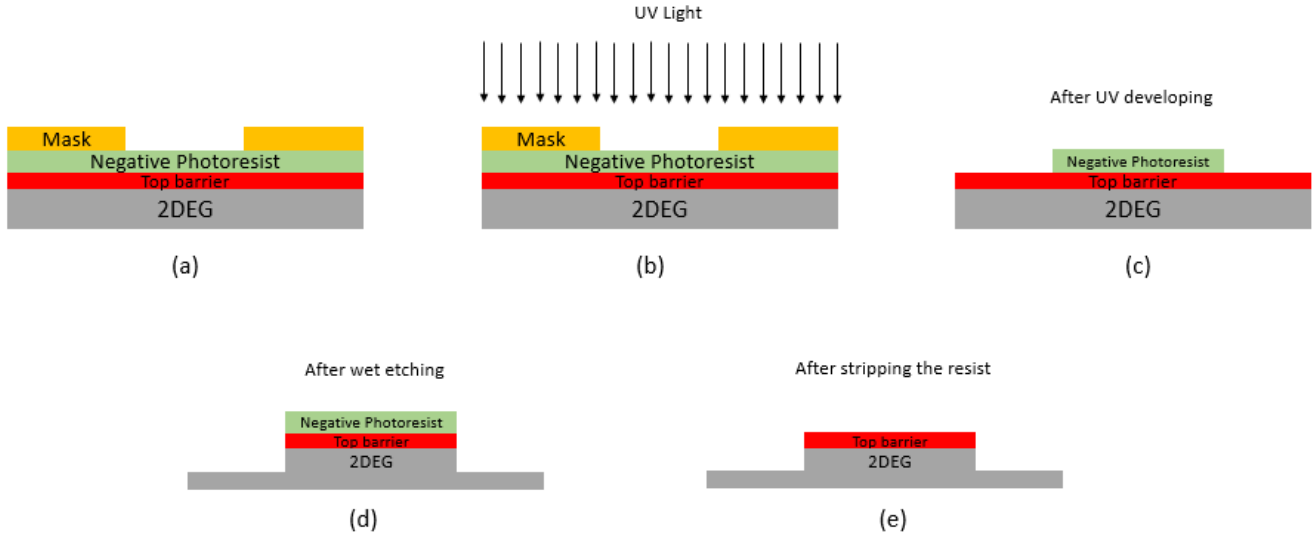

Figure 6.2: Mesa fabrication steps using photolithography and Wet etching processes (a) Spinning the photoresist (b) UV light exposure using photo mask (c) UV development (d) Wet Etching and (e) Strip resist.

6.2.3 Ohmic contacts

For Ohmic contacts, two positive photoresists (PMGI and S1805) are used to create a bilayer with a large undercut with a thickness of around 1.5 μm. PMGI photoresist is deposited first, followed by the S1805 photoresist because the lateral development rate of PMGI is faster than that of S1805. Therefore, the undercut will be formed once we put the sample in a UV developer for the same amount of developing time used for S1805 only. This large undercut allows the deposition of discontinuous metal for ohmic contacts. The ohmic contacts must have smooth metallic edges to avoid leakage or poor contact upon wiring the bonds and testing the sample. Therefore, by having this undercut during the liftoff process, the edges of the patterned Ohmics will be very smooth. Liftoff process is when the extra deposited material over the photoresist is removed by dissolving the resist beneath this material in the PG remover solvent. The Ohmic contacts fabrication steps are shown in figure 6.3.

In order to make good Ohmic contact with the buried quantum wells, a method of etching down is used. This method is known as Recessed ohmic contacts, the cap layer and top barrier are etched away to have direct contact with the quantum well using tilt metal deposition at 45°. The samples are transferred quickly to the E-beam evaporation

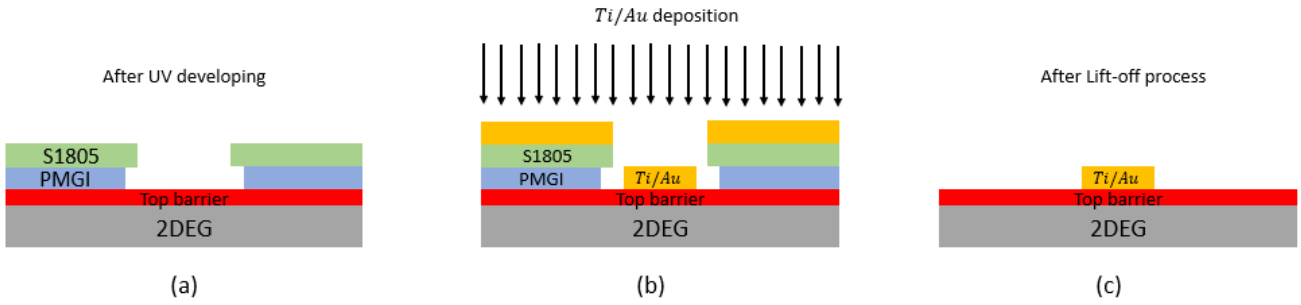

Figure 6.3: Ohmic contacts patterning steps. After the UV development of the sample (a) the undercut is shown in this step with a bilayer of photoresists. (b) Titanium/Gold (20nm/100nm) metal deposition using E-beam evaporator. (c) Liftoff process of removing the extra metal by stripping the resist using PG remover, resulting in discontinuous metal for ohmic contacts.

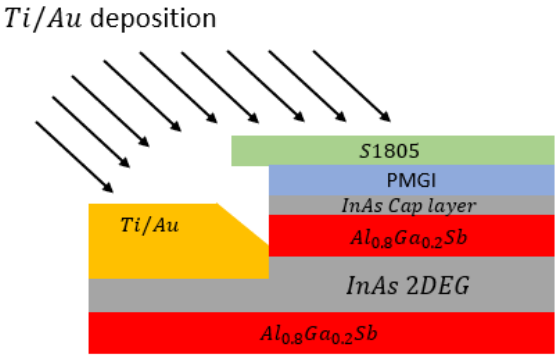

Figure 6.4: The schematic structure of Recessed ohmic contacts. Ti/Au is deposited with an angle of 45° using a rota-tilt, it makes good contact with the 2DEG. The undercut with the S1805 photoresist creates a suitable structure for lift-off.

chamber (Intlvac) directly after the wet etching to avoid any oxidation of the quantum well and having an oxide layer between the Ti/Au layer and the quantum well. The angular deposition of Ti/Au is shown in figure 6.4. It allows the metal to contact with the sidewall of the recessed area at the boundary of the Ohmic and depletes the quantum well.

6.2.4 Gated devices

Oxford PlasmaLab System 100 FlexAl Atomic Layer Deposition (ALD) is used to deposit the oxide layer HfO_2 for gated devices. The process starts with mesa patterning followed by the ohmic contacts process, as explained in the previous sections. HfO_2 is deposited at a temperature 150 ^oC, then photolithography is used to pattern the vias on the top of the Ti/Au ohmic contacts. After spinning a single layer of S1805 and UV exposure of the sample using a vias pattern in the photomask, the oxide layer within the vias is etched using BOE. Then, the resist used for the vias is washed away using a UV developer. Another single layer of S1805 photoresist is spun, then the patterns of bond pads and top gate in the photomask are used for the UV exposure. Ti/Au is deposited again for the bond pads, which will be connected to the ohmic contacts through these windows, and also this metal deposition is for the top gate. Bond pads are used to connect the ohmic contacts of the device to the pins of an external chip carrier off mesa using wire-bonding. Bond pads are designed to have large areas located off-mesa to avoid any damage to the conductive areas on-mesa of the device. The last step in the fabrication is the wire-bonding of the bond pads. Unfortunately, our gated devices did not work; they had a problem with the HfO_2. There was a leakage through the oxide layer, and later we discovered that the chamber of the HfO_2 has a problem with adjusting the temperature. The detailed fabrication process and the chemicals used are found in Appendix A.

Chapter 7

Quantum transport Measurements and Results

7.1 Introduction

Two-dimensional electron gas (2DEG) formed in quantum wells and at heterojunction interfaces have been investigated using Hall effect. Hall effect measurements have been used extensively to determine the majority carrier concentrations and their mobilities in bulk and thin-film materials. In order to observe this effect, both electric and magnetic fields have to be applied to the 2DEG. Quantum Hall effect appears in 2DEG at low temperatures typically at liquid Helium temperature (T=4.2 K), and high magnetic fields applied perpendicularly to the plane of the 2DEG. The Quantum Hall effect and its relation to fundamental physical constants were discovered in 1980 by Von Klitzing, for which he received a Nobel prize in 1985. When the de Broglie wavelength (λ_{dB}) of electrons is more than the size of the semiconductor structure, quantum mechanical treatment must be considered of the transport properties in nanostructures [46]. The observation of the quantum hall effect takes place when the thermal energy is less than the energy level separation ($K_B\mathrm{T} < \Delta\mathrm{E}$); that is why the measurements must be held at low temperatures because the room temperature corresponds to 25 meV. Scattering of electrons can affect the quantum effects. Therefore, the mean free path of electrons must be larger than the quantum well dimensions. When the mean free path of electrons is larger than the confinement dimensions, the ballistic transport regime dominates the transport of electrons. Mesoscopic physics came from this limit of quantum effects and carrier transport at which both particle-wave duality is exhibited [19].

7.2 Hall Measurements

7.2.1 Hall effect

The quality of a quantum well can be described by measuring the mobility from which the mean free path of electrons and momentum relaxation time (time between two successive collisions of electrons) can be determined. Upon applying the magnetic field to an electric current in a perpendicular direction within a semiconductor, the charge carriers of the current will experience a force called Lorentz force. The influence of this force on the motions of the electrons and holes with the applied electric and magnetic fields is shown in figure 7.1. As shown in the figure, the magnetic field is applied along the z-direction perpendicular to the electric current, followed along the x-axis. If the charge carriers are electrons, they will be deflected in the -y-direction under the influence of the Lorentz force at the y=0 surface. An electric field will be produced in the +y-direction due to the net charge. After the accumulation of charges on one direction which is known as steady-state, the net force is zero as the magnetic force is balanced by the electric force which is expressed as

$$\vec{F} = e(\vec{E} + v \times \vec{B}) \tag{7.1}$$

This equation gives

$$E_y = v_x B_z \tag{7.2}$$

where v_x is the charges drift velocity along the x-direction and E_y along the y-direction is known as Hall field. This Hall field produces a voltage across the width (W) of the sample expressed as

$$V_H = E_y W \tag{7.3}$$

where V_H is called the Hall voltage. The polarity of this voltage determines the type of charge carriers. By substituting equation 7.2 into equation 7.3 the Hall voltage will be

$$V_H = v_x B_z W \tag{7.4}$$

The drift velocity v_x can be written as

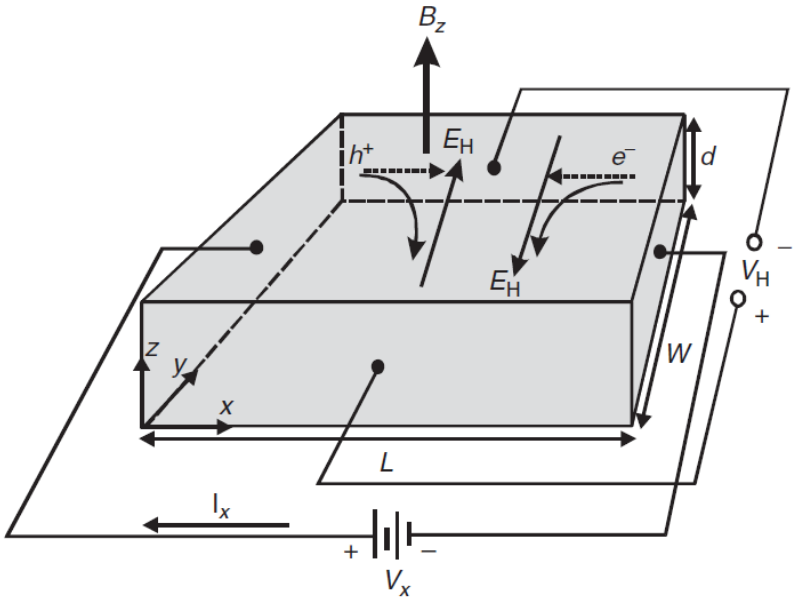

Figure 7.1: The structure of the hall bar under the influence of applied electric and magnetic fields.

$$v_x = -\frac{J_x}{en_H} = -\frac{I_x}{en_H W d} \tag{7.5}$$

where J_x is the current density flowing through the surface area of the sample at $x = L$ in figure 7.1, which is equal to the sample's width (W) multiplied by its thickness (d). n_H is the charge carrier density, for semiconductors like InAs, the conduction is not dominated by a single charge carrier. However, simultaneous contributions from both electrons and holes can be significantly involved in the semiconductor materials conduction. Therefore, the total charge carrier density here involves both electrons and holes. By substituting equation 7.5 into equation 7.4, then Hall voltage can be expressed as

$$V_H = \frac{I_x B_z}{edn_H} \tag{7.6}$$

As the current and Hall voltage can be measured experimentally across the width of the 2DEG, the charge density can be determined from equation 7.6 as

$$n_H = \frac{I_x B_z}{edV_H} \tag{7.7}$$

Then, the Hall mobility is determined from the total charge carrier density from this relation,

$$I_x = J_x W d = e n_H \mu E_x W d = \frac{e n_H \mu V_x W d}{L} \tag{7.8}$$

Therefore, from equation 7.8 the mobility μ is found from the total carrier density n_H, the applied voltage V_x across the length of the 2DEG as

$$\mu = \frac{I_x (L/W)}{e V_x n_H d} \tag{7.9}$$

Another parameter that is significant for Hall measurements is the Hall coefficient R_H which can be expressed as

$$R_H = \frac{r E_y}{J_x B_z} = -\frac{r}{n_H e} \tag{7.10}$$

where r is the Hall factor, it is very close to unity. For example, the r factor of InAs is in the range of 1.0 – 1.3. In general, we can say that the concentration and mobility results obtained from Hall effect measurements significantly depend on the geometry of the sample.

7.2.2 Magnetotransport and Quantum Hall effect

In small dimensional semiconductor systems, quantum transport offers the investigation of essential properties, like the quantum Hall effect (QHE), ballistic transport, and the Shubnikov-de Haas (SdH) effect. Upon applying a perpendicular magnetic field on a two-dimensional semiconductors systems, quantization of energy in a series of Landau levels takes place, which results in Hall resistance quantization [38]. The condition of wave-length in Quantum Hall effect (QHE) came from the Landau magnetic length L_H which is expressed as

$$L_H = \sqrt{\frac{\hbar}{eB}} \tag{7.11}$$

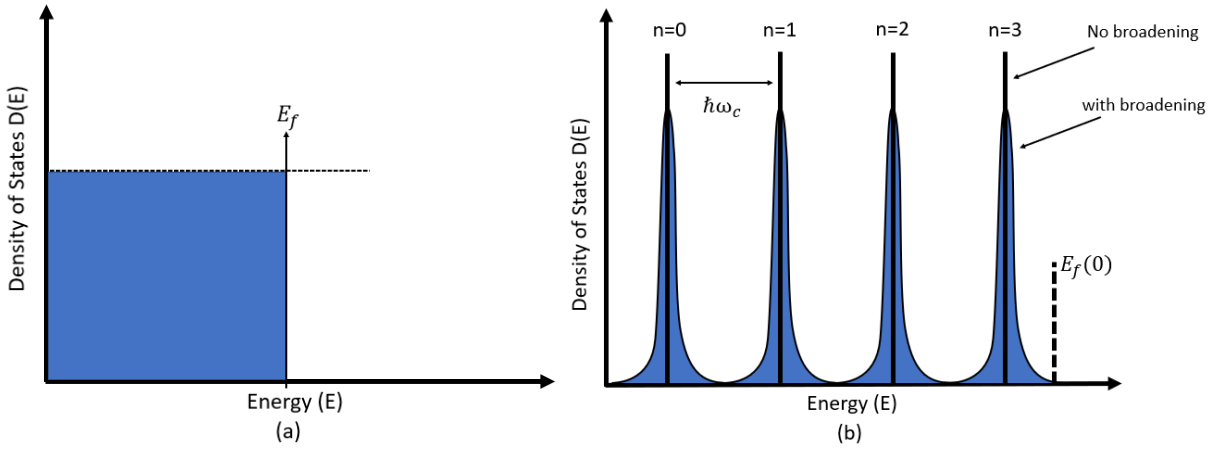

Figure 7.2: The 2-dimensional electron gas electronic density of states (a) with zero magnetic field, the states are filled up to the Fermi level which contains all allowed states. (b) Landau levels and Fermi level upon applying magnetic field, the broadening of Landau levels is due to different scattering mechanisms happens during transport.

which is also known as the cyclotron radius of the lowest Landau energy level. The 2DEG density of states is modified upon applying a magnetic field. With the zero magnetic field, the 2-dimensional density of states is a step function with the 2D confinement. Landau levels are the quantized energy eigenvalues occupied by electrons in the presence of the applied magnetic field. This 2D discretized density of states (Landau levels) is spaced by $\hbar\omega_c$ with no available states in between, where ω_c is the cyclotron frequency. Splitting of the electronic energy levels into the number of Landau levels occurs by applying a magnetic field with a separation of $\hbar\omega_c$. This phenomenon is shown in figure 7.2. Each Landau level has a density of states per unit area as [46]

$$\left(\frac{m^*}{2\pi\hbar^2}\right) \times (\hbar\omega_c) = \frac{\omega_c m^*}{2\pi\hbar} = \frac{eB_z}{h} \tag{7.12}$$

where B_z is the applied magnetic field along the z-direction, and 'h' is the Planck's constant. By applying the magnetic field along the perpendicular direction of 2DEG, the electrons are confined in the x-y plane within quantum wells and heterojunctions. Thus, each Landau level will have a delta function with a degeneracy of $(\frac{eB_z}{h})$, which is shown in figure 7.2 as the solid vertical lines with "no broadening" label [46]. However, the impurities, dislocations, interface roughness, and crystal defects will result in broadening this density of states delta function, as shown in figure 7.2 with the label "with broadening".

Quantum Hall effect (QHE) is an important result of the 2D density of states quantization into Landau levels, and the disorder of the sample has a significant role in measuring the Hall resistance. The Fermi level is shown as the dotted line in figure 7.2 will drop to the next Landau level once the Landau levels are depleted. To measure the quantum Hall resistance, disorder of the sample is essential as this disorder creates localized states as a result of the defects in the sample. Thus, the quantized Hall resistance is not found as an instantaneous data point in the measurements. These localized states are not involved in the transport, and their energy states lie between Landau levels. Thus, within the gap of these localized states, the Fermi energy level can be found. The depletion of these localized states takes place with increasing the magnetic field. However, the Hall resistance does not change because of there localized property that prevents them from being involved in the conductance of the device. Thus, the localized states depopulate and plateaus appear in the Hall resistance with the range of applied magnetic values, this Hall resistance of the plateau can be expressed as

$$R_{xy} = \frac{h}{e^2}\frac{1}{\nu} \tag{7.13}$$

where ν is the filling factor (ν=1,2,3,...) as this resistance plateau is related to an integer number of filled Landau levels.

7.2.3 Shubnikov-de Haas (SdH) oscillations

The SdH effect allows one to precisely measure the carrier concentrations formed at heterojunction interfaces. The oscillations observed in the resistivity ρ_{xx} are due to the sweeping of Landau levels across the Fermi levels with increasing the magnetic field. Landau levels have a constant density of states in two-dimensional systems, leads to the periodicity of the oscillations in ρ_{xx} as a function of $(1/B_z)$, from this periodicity the charge density of the 2DEG can be measured [46]. The definition of filling factor can be expressed as

$$\nu \equiv \frac{hn_s}{eB_z} \tag{7.14}$$

where n_s is the charge density in the 2DEG. With this definition of filling factor, the density of states is found to be minimum when the Fermi level lies between two Landau levels. In this case, the minimum resistivity is observed. Thus, the charge density is obtained from the magnetic field spacing of two successive minima in resistivity (adjacent Landau levels) from [46].

$$n_s = \frac{e}{h}\left(\frac{1}{\Delta(1/B_z)}\right) \tag{7.15}$$

For accurate measurement of charge density n_s, it is obtained at minimum spin splitting and large ν (small values of B_z).

7.3 Measurements setup and results

7.3.1 Measurements Setup

All the Hall measurements in this thesis were conducted by the Ph.D. student Annelise Bergeron and Associate Prof. Francois Sfigakis from Prof. Jonathan's Baugh group at the University of Waterloo. The base temperature of the Janis Cryostat used for measuring our Hall bars devices is 1.4 K. The measurements are performed with a range of temperatures from 1.4 K to 260 K by using the temperature controller equipped in our system. The superconducting magnet in the system allows a magnetic field range from -6 Tesla to 6 Tesla. Standard AC lock-in techniques with Stanford Research Systems SR830 lock-in amplifiers are used in all the measurements [6]. The chip carriers have 12 pins to allow the gated Hall bars connection. These chip carriers are found on the top of the transport probe, which has 24 twisted pair DC wires. The wires are connected to the top end of the probe, which is at room temperature. As said before, the measurements depend on the temperature; the thermometer attached to the probe near the sample allows the temperature measurement. From the wiring between the sample and the probe, the temperature set-point can be achieved by balancing the Helium flow rate and heater power. The sample resistance is saturated when the thermal equilibrium is achieved [6].

The Hall bar device geometry used for measuring carrier density and mobility is shown in figure 7.3. The end ohmic contacts (4 and 8) provides the current through our entire structure; they act as a current source and drain. The lateral ohmic contacts (1-3 and 5-7) are used as voltage probes for measuring different combinations of voltages across the length and width of the device. Hall voltage V_H, is measured by using these lateral ohmic contacts, across the 2DEG width. By using the V_H value, the charge density is calculated by using equation 7.7. The carrier mobility is then calculated from equation 7.9. As mentioned before, the Hall bar was designed to have (L/W) ratio equal to 8; this ratio is critical in order not to have an undesired longitudinal component in the Hall voltage as its equation assumes rectangular geometry [6]. After measuring the longitudinal voltage, V_x, the longitudinal resistivity $\rho_x x$ can be obtained from

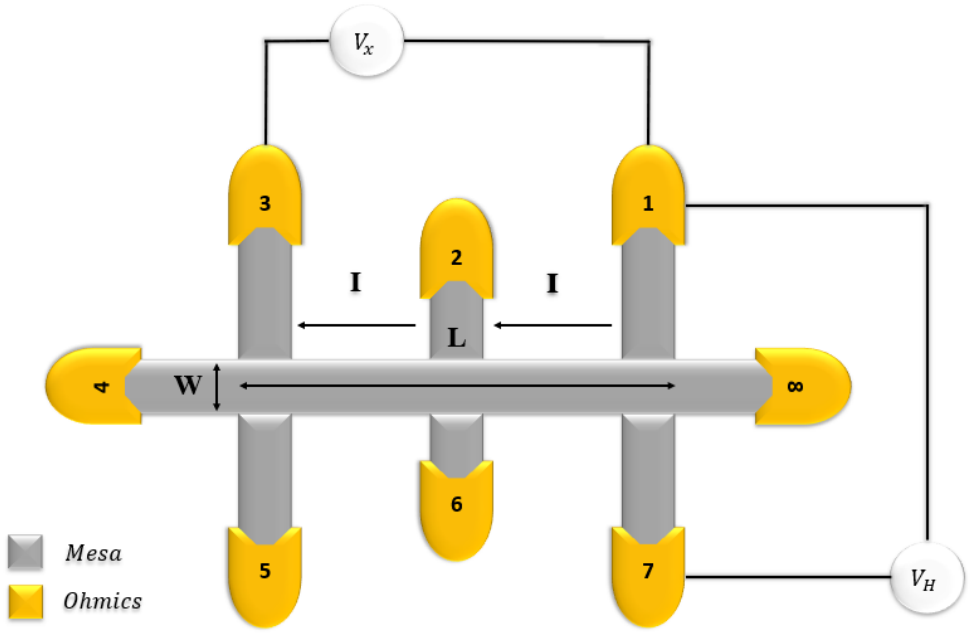

Figure 7.3: The device geometry used for quantum Hall effect and Shubnikov-de Haas measurements. Current source and drain are ohmic contacts found at the both ends (4 and 8). Voltage probes for different voltage combinations measurements V_x and V_H are the lateral ohmic contacts (1-3 and 5-7).

$$\rho_{xx} = \frac{W}{L}\frac{dV_x}{dI} \tag{7.16}$$

As discussed before in section 5.2.1, our Hall bar device has six lateral ohmic contacts instead of four, and it offers six different longitudinal voltage measurement combinations with the applied current at the end ohmic contacts. The uniformity of the devices can be checked by measuring the voltage drop across 1 and 2 ohmic contacts and voltage drop across 2 and 3 ohmic contacts, these voltage drops should be equal for uniform devices, and the voltage drop across ohmic contacts 1 and 3, should be equal to their summation. Additionally, the other side should also agree with the same three voltage measurements. The non-uniformity of the devices can be a result of poor photoresist adhesion, which leads to a significant problem in the wet etching of the mesa during the device fabrication. Various voltage probe measurements are performed for measuring the quantum Hall effect and SdH oscillations. The measuring of different combinations of longitudinal and transverse voltages is performed for a range of magnetic fields around 0

to 5 T, using a constant current AC 4-point measurement at a low frequency of 10 Hz. Our system has a 1 MΩ connected in series with the sample through which a one volt AC signal is sent. Therefore, the current will not change with the changes in the resistance of the sample. A reduction of the oscillations can happen during the quantum Hall effect and SdH oscillations measurements because of the increased temperature, so that the current is limited to less than or equal 1 μA in order to reduce the Joule heating effect.

7.3.2 Carrier mobility and density measurement Results

The quantum Hall effect and SdH oscillations measurements were taken for many samples having the same material structure shown in figure 4.1 but with a different Arsenic composition (y%) in the quaternary buffer. Table 7.1 shows the measured carrier mobility (μ) and carrier density (n_{2D}) of all measured InAs quantum well growths in order of increasing As concentration (y%) in the quaternary buffer. All the samples in this table have the same materials' structure except for G0702 and G0703 samples; they have InSb-like interfaces at the top and lower barriers. It has been shown in the literature that forced InSb-like transi-

Sample ID	μ (cm^2/Vs)	n_H (cm^{-2})	As composition (y)
G0585	44,200	5.84×10^{11}	2.3 %
G0600	97,000	6.30×10^{11}	6.0 %
G0603	73,000	8.82×10^{11}	7.6 %
G0661	100	1.0×10^{11}	11.6 %
G0679	92,000	4.38×10^{11}	5.5 %
G0681	122,000	5.23×10^{11}	5.3 %
G0683	–	–	5.4 %
G0695	–	–	9.9 %
G0702*	20,000	1.80×10^{11}	7.3 %
G0703*	1,700	2.40×10^{11}	6.4 %
G0732	–	–	10.2 %
G0737	–	–	9.4 %
G0738	–	–	7.5 %

Table 7.1: Carrier mobility and density of growths in order of increasing As percentage in the quaternary buffer. The * symbol denotes growths with InSb-like transitions at the quantum well and barrier layers interfaces. Carrier mobility and density were not calculated for some samples.

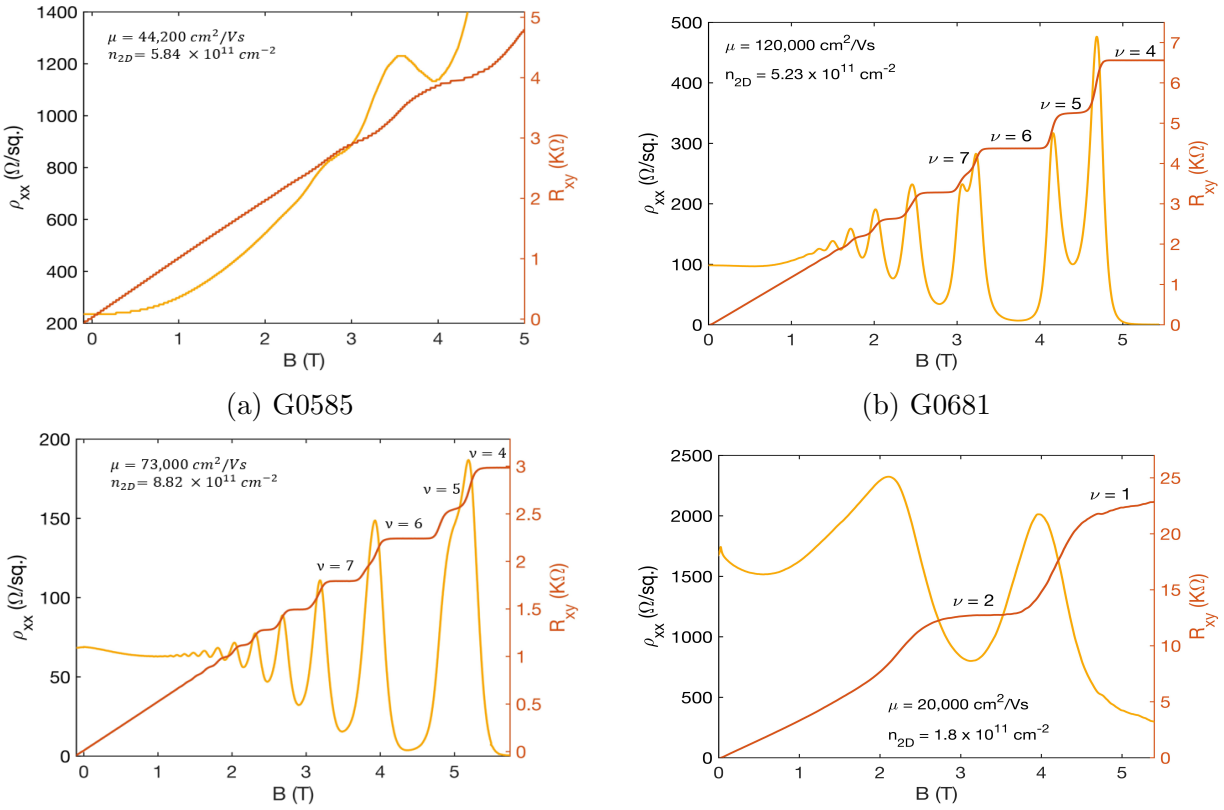

(a) G0585 (b) G0681

(c) G0603 (d) G0702

Figure 7.4: The magneto-transport for G0585 is shown in (a), which exhibits a significant parabolic background conductance. The improved transport data from G0681 is shown in (b) where the parabolic background in the SdH oscillations has been eliminated. Also seen in (b) is the onset of spin splitting at 4.5 T and no signs of parallel conduction. In (c) the magneto-transport data of G0603 is shown with no signs of parallel conduction present in the sample and the onset of spin splitting seen again at 5 T. All data was taken at 1.4 K. Figure (d) shows magneto-transport data of G0702 where the carrier concentration and mobility are indeed lowered.

tions at the AlGaSb/InAs interfaces can improve the mobility of InAs quantum wells [72]. Figure 7.4 shows the magneto-transport data for four different samples with the measured carrier mobility, density, and zero-field resistivity.

Discussion

The arsenic supply for samples G0585, G0681, G0679, and G0600 was below 7%. All growths with undersupplied arsenic in the quarternary buffer exhibited compressive strain. The arsenic supply in G0603, however, surpassed the target amount and yielded an arsenic supply of 0.076. Opposed to the other four growths, this growth exhibited tensile strain. The magneto-transport data for each of G0585, G0681, G0603, and G0702 samples are shown in figure 7.4. Similar magneto-transport data for other samples are shown in Appendix B. From the data set, it can be seen that the carrier density of the structure depends sensitively on the arsenic contribution of the quaternary buffer. The SdH oscillations of figure 7.4a show the oscillations of a low density (few oscillations) quantum well superimposed on a parasitic parabolic background from a parallel conducting channel in the structure. The SdH oscillations of figure 7.4b show oscillations of a high-density quantum well (many oscillations) with no parallel conduction as the SdH oscillations hit zero in resistance, the mobility of this sample was the highest mobility among all the other samples. The SdH oscillation of figure 7.4c also show oscillations of high-density quantum well with no obvious signs of parallel conduction, absence of parallel conduction was later confirmed by measuring the sample to a higher field in the 20 T dilution fridge which is shown in figure 7.5. The samples with good quality were also measured to a higher magnetic field to confirm the absence of parallel conduction.

Conclusion

In conclusion, lattice matching is achieved for an As composition of 7%. When As composition unintentionally moved away from 7%, there is roughly a factor of 2 drop-in carrier density. The samples that attained compressive strain with As composition range from 5.4% to 6.1% showed the highest carrier mobility among all other samples. However, for G0603 with a 7.6% of As, it suffers from tensile strain and has a moderate carrier density and mobility. The carrier density and mobility were significantly dropped with a very high As composition like G0661 sample with 11.6% of As. We concluded that the compressive strain in the samples does not affect the carrier density and mobility as much as the tensile strain does. It is clearly seen from comparing sample G0585 with sample G0661 that, both were moved away from the 7% As composition with around 4.7%. However, sample G0585 has a much better carrier density and mobility than sample G0661. This finding is supported by Nomarski pictures of both samples in figure 7.7; the surface roughness associated with crosshatches in G0661 is more than that in G0585. The surface roughness can induce different scattering mechanisms inside the InAs quantum well, reducing the carrier density and mobility.

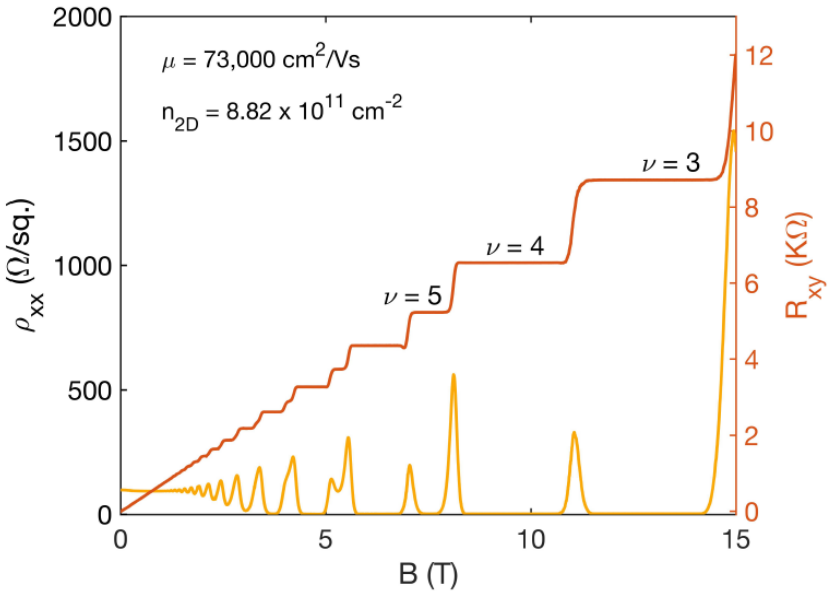

Figure 7.5: Magneto-Transport data of sample G0603 up to 15 T at 10 mK.

The most probable reason is the interface roughness scattering induced in the lower barrier due to the threading dislocations generated with the very high As composition of 11.6% in the quaternary buffer, as the lattice parameter is pushed away from being matched to the lower barrier ($Al_{0.8}Ga_{0.2}Sb$). In contrast, very low As composition of 2.3% will not induce the same amount of roughness scattering, because the lattice parameter is pushed towards being matched to the lower barrier. As explained in section 4.1.6, interface roughness scattering associated with lower barrier has a significant effect on the electron mobility within the InAs quantum well. The influence of As composition in the quaternary buffer on the carrier mobility within the InAs quantum well is shown in figure 7.6. As long as the As amount is between 5% to 7%, the highest mobilities will be achieved. If the As amount is unintentionally very high, the carrier mobility will be dramatically decreased.

We have learned in section 4.1.5, the forced InSb-like interfaces between the quantum well and lower barrier enhance the mobility. We have employed these InSb-like transitions for some of our samples. The magneto-transport date for two of these samples (G0702* and G0703*) are given in table 7.1. Unfortunately, a significant decrease in carrier concentration and mobility was observed in these samples. However, there was no noticeable improvement in the quality of the material structure. The growth of these interfaces is susceptible to the growth conditions as it needs lower substrate temperature, as previously mentioned. We

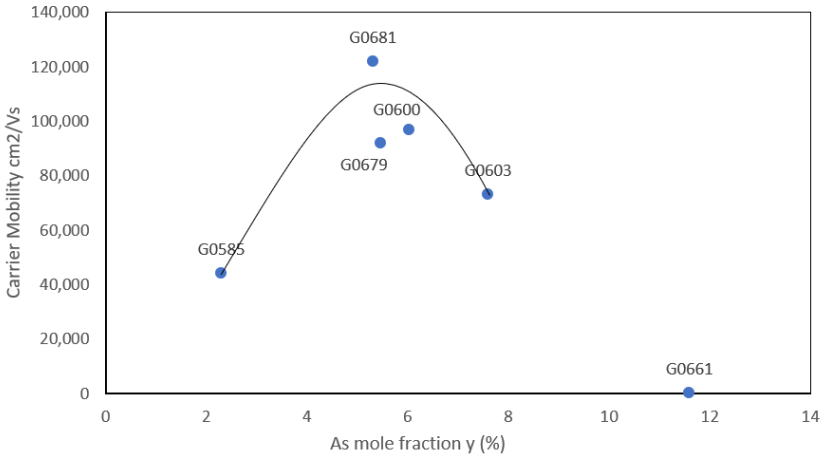

Figure 7.6: The influence of As composition in the quaternary buffer on the carrier mobility within the InAs Quantum well.

have made further attempts using the InSb-like transitions, but we did not have the chance to measure them because of the labs' shutdown due to COVID-19. We have investigated the reason behind this low carrier concentration and mobility of these samples. Most probably, during the long pause of temperature change for the growth of the InSb-like interface, the exposed $Al_xGa_{1-x}Sb$ surface absorbs residual impurities in the chamber which can affect the electron mobility. For the upper InSb-like interface, we did not introduce a pause time after closing the As valve to allow for more pumping. Arsenic that can be found in the chamber can intermix in the heterostructure inducing alloy scattering in the samples, which causes mobility reduction. We planned to solve these problems to have high-quality interfaces.

7.3.3 Temperature dependence of carrier density and mobility

The temperature dependence of the on-mesa and off-mesa resistances, as well as the carrier mobility and density, were tested for most of the samples fabricated. The temperature dependence data for G0603 are shown in figure 7.9. Moreover, temperature dependence data of G600 (on-mesa) is shown in figure 7.8

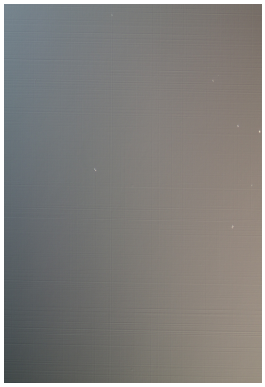

(a) G0585 at x5

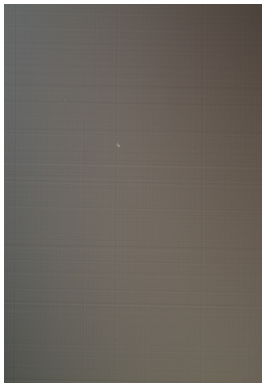

(b) G0585 at x40

(c) G0661 at x5

(d) G0661 at x40

Figure 7.7: The Nomarski pictures for G0585 and G0600 samples with different lenses.

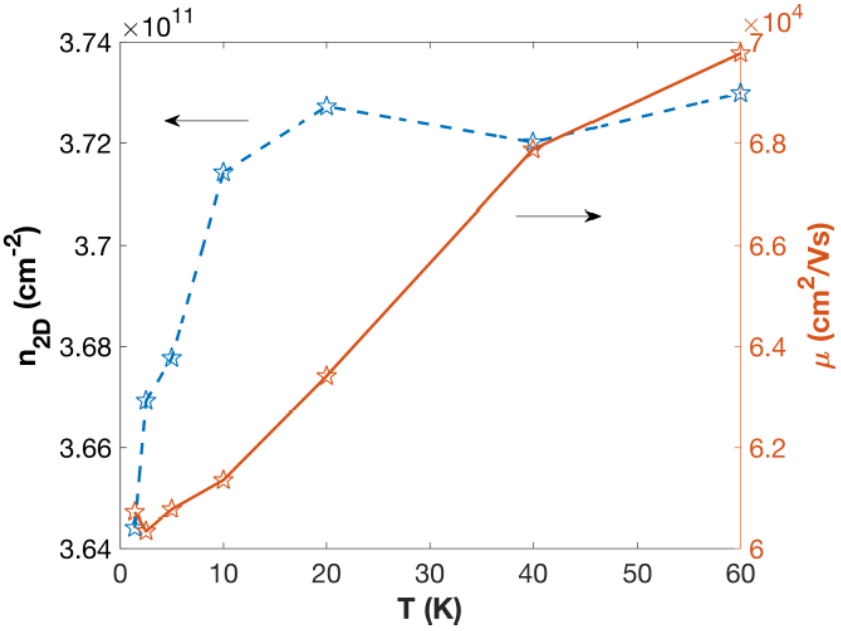

Figure 7.8: Temperature dependence of the 2DEG of G0600 sample (on-mesa). Carrier density (left-axis) and mobility (right-axis) are shown.

Discussion

Temperature dependence of the G0600 (on-mesa) in figure 7.8 shows behavior comparable to an insulator at higher temperatures, which suggests the buffer is beginning to dominate

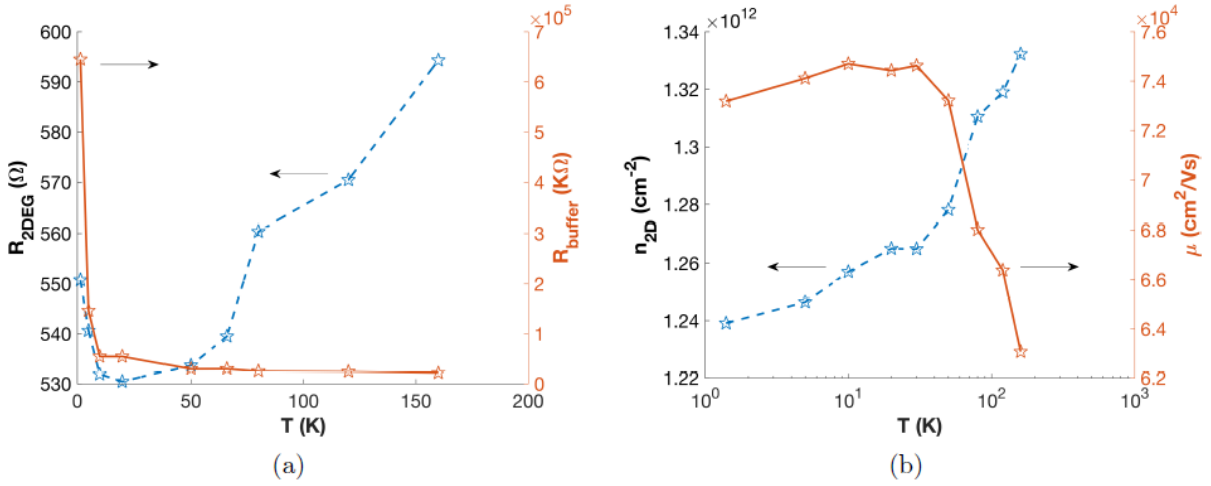

Figure 7.9: The temperature dependence of the on-mesa and off-mesa resistance (a) as well as the carrier mobility and density (b) of sample G0603.

transport at temperatures above 5 K. The temperature dependence of the carrier density and mobility of G0603 is shown in figure 7.9(a), behaves like a proper quantum well with the mobility increasing as a function of decreasing temperature until reaching a plateau from some limiting scattering mechanism in the structure. Additionally, in figure 7.9(b) the buffer goes highly insulating at temperatures below 10 K. Even though the off-mesa buffer resistance of G0603 at base temperature was only 675 KΩ which less than the 3.6

Sample ID	R_{QW}/R_{Buffer}
G0585	$\frac{1900\Omega}{0.5M\Omega} = 3.8 \times 10^{-3}$
G0600	$\frac{1122\Omega}{3.6M\Omega} = 3.12 \times 10^{-4}$
G0603	$\frac{550\Omega}{0.675M\Omega} = 8.14 \times 10^{-4}$

Table 7.2: The ratio of on-mesa to off-mesa resistance of the samples G0585, G0600 and G0603.

MΩ of G0600, it was still an improvement over G0585 which was less than 0.5 MΩ.

We concluded that the samples with the compressive strain (less than 7% of As) have larger off-mesa resistance than the samples with tensile strain. Considering G0603 has no parallel conduction like G0600 despite having an off-mesa resistance comparable to the significantly parallel conducting G0585 structure, a possible explanation may be that the ratio of on-mesa to off-mesa resistance may play a role. Table 7.2 shows that the ratio of on-mesa to off-mesa resistance of the samples differs by orders of magnitude between the parallel conducting and non-parallel conducting samples. Despite having significantly different off-mesa resistances, the ratios for G0600 and G0603 are comparable since G0603 has a less resistive 2DEG than G0600.

Chapter 8

Conclusion and Future work

8.1 Conclusion

The growth optimization of the two-dimensional electron gas (2DEG) in InAs quantum wells and magneto-transport data presented in this work gave us a chance to make progress on the challenges to develop material foundations for building a suitable platform for the realization of Majorana fermion devices.

Using the new approach developed for quaternary buffer growth, we succeeded in achieving the reproducibility of high-quality buffer layers with the 7% of As or even very close to this composition. It was found from the magneto-transport data that the variations of As compositions in the buffer layer affect the carrier charge density and mobility in InAs quantum wells. The electron density and mobility of the samples with As compositions much higher than 7% were significantly reduced. Therefore, samples with a quaternary buffer ($Al_xGa_{1-x}As_ySb_{1-y}$) with an As mole fraction (y) less than or equal to 7% has much better electron density and mobility than the ones with As mole fraction greater than 7%.

The calculations from the X-ray diffraction model was beneficial for achieving the 7% of As in the quaternary buffer $Al_xGa_{1-x}As_ySb_{1-y}$. The model introduced here for the lattice parameters, and As composition calculations of $Al_xGa_{1-x}As_ySb_{1-y}$ buffer using Reciprocal Space Maps was used for the first time. This model has very reproducible and accurate results for As composition and lattice parameters, compared to their values extracted directly from Omega-2Theta scans using Jordan Valley software. We also concluded that in order to have a quaternary buffer with a 7% As composition or even close to 7%, we have to sacrifice two or three growths before achieving the target due to varying growth

conditions in each growth. Using the XRD model with the new approach of quaternary buffer growth, we consistently achieved high-quality 2DEGs in InAs quantum wells grown on nearly lattice-matched GaSb substrates suitable for pursuing superconducting InAs devices on a path towards the realization of Majorana Fermions. Furthermore, our materials system structure outperforms even the highest quality InAs nanowires.

8.2 Future Work

- Optimization of the InSb-like interfaces between the barriers and InAs quantum well following the growth procedure mentioned in section 4.1.5.
- Changing the upper barrier for our materials' structure from $Al_xGa_{1-x}Sb$ to $In_xGA_{1-x}As$ which has lower bandgap and can be used for superconducting devices. Only one growth was performed using this upper barrier yet to be measured.
- The fabrication of superconducting InAs devices using E-beam lithography to pattern the superconducting Al metal deposited on our semiconductor materials structure. (Unfortunately, it has been delayed due to COVID-19 labs shutdown)
- Pursuing a new approach of in-situ Aluminium deposition using MBE on our semiconductor materials structure, it was proved to yield a high-quality Superconductor-Semiconductor system with uniform, transparent interfaces [61].

References

[1] Sadao Adachi. *Physical properties of III-V semiconductor compounds*. John Wiley & Sons, 1992.

[2] Sadao Adachi. *Properties of semiconductor alloys: group-IV, III-V and II-VI semiconductors*, volume 28. John Wiley & Sons, 2009.

[3] Sadao Adachi. Iii-v ternary and quaternary compounds. In *Springer Handbook of Electronic and Photonic Materials*, pages 1–1. Springer, 2017.

[4] G Almuneau, E Hall, S Mathis, and LA Coldren. Accurate control of sb composition in algaassb alloys on inp substrates by molecular beam epitaxy. *Journal of crystal growth*, 208(1-4):113–116, 2000.

[5] Neil W Ashcroft, N David Mermin, et al. Solid state physics [by] neil w. ashcroft [and] n. david mermin., 1976.

[6] Bergeron, Emma. Study of surface quantum wells in insb/alinsb heterostructures, university of waterloo., Master's Thesis, 2019.

[7] CR Bolognesi, H Kroemer, and JH English. Interface roughness scattering in inas/alsb quantum wells. *Applied physics letters*, 61(2):213–215, 1992.

[8] CR Bolognesi, H Kroemer, and JH English. Well width dependence of electron transport in molecular-beam epitaxially grown inas/alsb quantum wells. *Journal of Vacuum Science & Technology B: Microelectronics and Nanometer Structures Processing, Measurement, and Phenomena*, 10(2):877–879, 1992.

[9] D Keith Bowen and Brian K Tanner. *X-ray metrology in semiconductor manufacturing*. CRC Press, 2018.

[10] AS Bracker, MJ Yang, BR Bennett, JC Culbertson, and WJ Moore. Surface reconstruction phase diagrams for inas, alsb, and gasb. *Journal of crystal growth*, 220(4):384–392, 2000.

[11] Lawrence Bragg. The third clerk maxwell memorial lecture. the diffraction of short electromagnetic waves. *Journal of the British Institution of Radio Engineers*, 17(9):467–471, 1957.

[12] Auguste Bravais. Les systemes formes par des pointes distribues regulierement sur un plan ou dans l'espace. *J. Ecole. Polytech.*, pages 1–128, 1850.

[13] Auguste Bravais. *Abhandlung über die Systeme von regelmässig auf einer Ebene oder im Raum vertheilten Punkten*. Number 90. W. Engelmann, 1897.

[14] J-M Chauveau, Y Androussi, A Lefebvre, J Di Persio, and Y Cordier. Indium content measurements in metamorphic high electron mobility transistor structures by combination of x-ray reciprocal space mapping and transmission electron microscopy. *Journal of applied physics*, 93(7):4219–4225, 2003.

[15] Marvin L Cohen and James R Chelikowsky. *Electronic structure and optical properties of semiconductors*, volume 75. Springer Science & Business Media, 2012.

[16] Bernard Dennis Cullity. *Elements of X-ray Diffraction*. Addison-Wesley Publishing, 1956.

[17] Philippe Debray, SMS Rahman, J Wan, RS Newrock, M Cahay, Anh T Ngo, SE Ulloa, ST Herbert, Mustafa Muhammad, and M Johnson. All-electric quantum point contact spin-polarizer. *Nature Nanotechnology*, 4(11):759–764, 2009.

[18] Alan R Denton and Neil W Ashcroft. Vegard's law. *Physical review A*, 43(6):3161, 1991.

[19] Mildred Dresselhaus, Gene Dresselhaus, Stephen B Cronin, and Antonio Gomes Souza Filho. Two dimensional electron gas, quantum wells and semiconductor superlattices. In *Solid State Properties*, pages 247–274. Springer, 2018.

[20] M. Eckert. Max von laue and the discovery of x-ray diffraction. *Annalen der Physik*, 524(5):A83–A85, 1912.

[21] PP Ewald. A review of my papers on crystal optics 1912 to 1968. *Acta Crystallographica Section A: Crystal Physics, Diffraction, Theoretical and General Crystallography*, 35(1):1–9, 1979.

[22] Paul F Fewster. *X-ray Scattering from Semiconductors*. World Scientific, 2000.

[23] Helmut Foll. Semiconductors i, 5.1. 4 wavelength engineering. *Kiel University, Germany (accessed on Aug. 14, 2013)*.

[24] A Furukawa and S Ideshita. Origin of deep donors in alsb grown by molecular beam epitaxy. *Journal of applied physics*, 75(10):5012–5015, 1994.

[25] Frédéric Genty, Guilhem Almuneau, Laurent Chusseau, Arnaud Wilk, Serge Gaillard, Guilhem Boissier, Pierre Grech, and Joel Jacquet. Growth and characterization of vertical cavity structures on inp with gaassb/alassb bragg mirrors for 1.55 μm emission. *Journal of crystal growth*, 201:1024–1027, 1999.

[26] Anthony Michael Glazer. *A Journey Into Reciprocal Space: A Crystallographer's Perspective*. Morgan & Claypool Publishers, 2017.

[27] Michel F Gratton and John C Woolley. Phase diagram and lattice parameter data for the gaas y sb 1- y system. *Journal of Electronic Materials*, 2(3):455–464, 1973.

[28] Zheng-Cheng Gu, Hong-Chen Jiang, and G Baskaran. Emergence of p+ i p superconductivity in two-dimensional doped dirac systems. *Physical Review B*, 101(20):205147, 2020.

[29] AT Hatke, T Wang, C Thomas, GC Gardner, and MJ Manfra. Mobility in excess of 106 cm2/v s in inas quantum wells grown on lattice mismatched inp substrates. *Applied Physics Letters*, 111(14):142106, 2017.

[30] Mohamed Henini. *Molecular beam epitaxy: from research to mass production*. Newnes, Book, 2012.

[31] Marian A Herman and Helmut Sitter. *Molecular beam epitaxy: fundamentals and current status*, volume 7. Springer Science & Business Media, 2012.

[32] WE Hoke, TD Kennedy, and A Torabi. Simultaneous determination of poisson ratio, bulk lattice constant, and composition of ternary compounds: In 0.3 ga 0.7 as, in 0.3 al 0.7 as, in 0.7 ga 0.3 p, and in 0.7 al 0.3 p. *Applied Physics Letters*, 79(25):4160–4162, 2001.

[33] Hu, Yunong. Study of unintentional as incorporation into alsb and interfacial layers within inas/alsb superlattices, 2019.

[34] Harald Ibach and Hans Lüth. *Solid-state physics: an introduction to theory and experiment*. Springer Science & Business Media, 2012.

[35] Ayahiko Ichimiya, Philip I Cohen, and Philip I Cohen. *Reflection high-energy electron diffraction*. Cambridge University Press, 2004.

[36] BA Joyce and RR Bradley. A study of nucleation in chemically grown epitaxial silicon films using molecular beam techniques i.—experimental methods. *Philosophical Magazine*, 14(128):289–299, 1966.

[37] J Klem, R Fischer, TJ Drummond, H Morkoc, and AY Cho. Incorporation of sb in gaas1- xsbx (x¡ 0.15) by molecular beam epitaxy. *Electronics Letters*, 19(12):453–455, 1983.

[38] K v Klitzing, Gerhard Dorda, and Michael Pepper. New method for high-accuracy determination of the fine-structure constant based on quantized hall resistance. *Physical Review Letters*, 45(6):494, 1980.

[39] M Krieger, H Sigg, N Herres, K Bachem, and K Köhler. Elastic constants and poisson ratio in the system alas–gaas. *Applied physics letters*, 66(6):682–684, 1995.

[40] N Kuze, K Nagase, S Muramatsu, S Miya, T Iwabuchi, A Ichii, and I Shibasaki. Inas deep quantum well structures and their application to hall elements. *Journal of crystal growth*, 150:1307–1312, 1995.

[41] Eric C Larkins and James S Harris Jr. Quality gaas and aigaas. *Molecular beam epitaxy: applications to key materials*, page 114, 1995.

[42] Yanbo Li, Yang Zhang, and Yiping Zeng. Electron mobility in modulation-doped alsb/inas quantum wells. *Journal of Applied Physics*, 109(7):073703, 2011.

[43] Ikai Lo, WC Mitchel, and J-P Cheng. Electronic properties of al x ga 1- x sb/inas quantum wells. *Physical Review B*, 50(8):5316, 1994.

[44] Roman M Lutchyn, Erik PAM Bakkers, Leo P Kouwenhoven, Peter Krogstrup, Charles M Marcus, and Yuval Oreg. Majorana zero modes in superconductor–semiconductor heterostructures. *Nature Reviews Materials*, 3(5):52–68, 2018.

[45] Ettore Majorana. Teoria simmetrica dell'elettrone e del positrone. *Il Nuovo Cimento (1924-1942)*, 14(4):171, 1937.

[46] Mahmoud Omar Manasreh. *Introduction to nanomaterials and devices*. Wiley Online Library, 2012.

[47] Naidu S Mani. *Engineering Physics*. Pearson India, 2014.

[48] JW Matthews and AE Blakeslee. Defects in epitaxial multilayers: I. misfit dislocations. *Journal of Crystal growth*, 27:118–125, 1974.

[49] Takashi Mimura. The early history of the high electron mobility transistor (hemt). *IEEE Transactions on microwave theory and techniques*, 50(3):780–782, 2002.

[50] Chetan Nayak, Steven H Simon, Ady Stern, Michael Freedman, and Sankar Das Sarma. Non-abelian anyons and topological quantum computation. *Reviews of Modern Physics*, 80(3):1083, 2008.

[51] Chanh Nguyen, Berinder Brar, and Herbert Kroemer. Surface-layer modulation of electron concentrations in inas–alsb quantum wells. *Journal of Vacuum Science & Technology B: Microelectronics and Nanometer Structures Processing, Measurement, and Phenomena*, 11(4):1706–1709, 1993.

[52] Fabrizio Nichele, Asbjørn CC Drachmann, Alexander M Whiticar, Eoin CT O'Farrell, Henri J Suominen, Antonio Fornieri, Tian Wang, Geoffrey C Gardner, Candice Thomas, Anthony T Hatke, et al. Scaling of majorana zero-bias conductance peaks. *Physical review letters*, 119(13):136803, 2017.

[53] Michael A Nielsen and Isaac Chuang. Quantum computation and quantum information, 2002.

[54] Max Planck. *The theory of heat radiation*. Courier Corporation, 2013.

[55] Stefan Riedi, Christian Reichl, Matthias Berl, Luca Alt, Adrian Maier, and Werner Wegscheider. Electron gas quality at various (110)-gaas interfaces as benchmark for cleaved edge overgrowth. *Journal of Crystal Growth*, 455:37–42, 2016.

[56] George B Rybicki and Alan P Lightman. *Radiative processes in astrophysics*. John Wiley & Sons, 2008.

[57] Thomas Schäpers. Fabrication of superconductor/two-dimensional-electron-gas structures. *Superconductor/Semiconductor Junctions*, pages 21–30, 2001.

[58] E Selvig, BO Fimland, T Skauli, and R Haakenaasen. Calibration of the arsenic mole fraction in mbe grown gaasysb1- y and alxga1- xasysb1- y (y¡ 0.2). *Journal of crystal growth*, 227:562–565, 2001.

[59] AN Semenov, VS Sorokin, VA Solov'ev, B Ya Mel'tser, and SV Ivanov. Special features of sb 2 and sb 4 incorporation in mbe-grown algaassb alloys. *Semiconductors*, 38(3):266–272, 2004.

[60] J Shabani, AP McFadden, B Shojaei, and CJ Palmstrøm. Gating of high-mobility inas metamorphic heterostructures. *Applied Physics Letters*, 105(26):262105, 2014.

[61] Javad Shabani, Morten Kjærgaard, Henri J Suominen, Younghyun Kim, Fabrizio Nichele, Kiryl Pakrouski, T Stankevic, Roman M Lutchyn, Peter Krogstrup, R Feidenhans, et al. Two-dimensional epitaxial superconductor-semiconductor heterostructures: a platform for topological superconducting networks. *Physical Review B*, 93(15):155402, 2016.

[62] B Shojaei, ACC Drachmann, M Pendharkar, DJ Pennachio, MP Echlin, PG Callahan, S Kraemer, TM Pollock, Charles M Marcus, and CJ Palmstrøm. Limits to mobility in inas quantum wells with nearly lattice-matched barriers. *Physical Review B*, 94(24):245306, 2016.

[63] Scott A Speakman. Introduction to high resolution x-ray diffraction of epitaxial thin films. *MIT Center for Materials Science and Engineering, Cambridge*, 2012.

[64] Xiaoguang Sun, Shuling Wang, Jean S Hsu, Rubin Sidhu, Xiaoguang G Zheng, Xiaowei Li, Joe C Campbell, and Archie L Holmes. Gaassb: a novel material for near infrared photodetectors on gaas substrates. *IEEE Journal of selected topics in quantum electronics*, 8(4):817–822, 2002.

[65] Henri J Suominen, Morten Kjaergaard, Alexander R Hamilton, Javad Shabani, Chris J Palmstrøm, Charles M Marcus, and Fabrizio Nichele. Zero-energy modes from coalescing andreev states in a two-dimensional semiconductor-superconductor hybrid platform. *Physical review letters*, 119(17):176805, 2017.

[66] Man Chun Tam, Yinqiu Shi, Denise Gosselink, Marc Jaikissoon, and Zbig R Wasilewski. Temperature monitoring of narrow bandgap semiconductors. *Journal of Vacuum Science & Technology B, Nanotechnology and Microelectronics: Materials, Processing, Measurement, and Phenomena*, 35(2):02B102, 2017.

[67] C Thomas, AT Hatke, A Tuaz, R Kallaher, T Wu, T Wang, RE Diaz, GC Gardner, MA Capano, and MJ Manfra. High-mobility inas 2degs on gasb substrates: A platform for mesoscopic quantum transport. *Physical Review Materials*, 2(10):104602, 2018.

[68] Jeffrey Y Tsao. *Materials fundamentals of molecular beam epitaxy*. Academic Press, 2012.

[69] Thomas Tschirky. *MBE Growth of 6.1 Å Family Semiconductor Heterostructures*. PhD thesis, ETH Zurich, Phd Thesis, 2018.

[70] Thomas Tschirky, Susanne Mueller, Ch A Lehner, Stefan Fält, Thomas Ihn, Klaus Ensslin, and Werner Wegscheider. Scattering mechanisms of highest-mobility inas/al x ga 1- x sb quantum wells. *Physical Review B*, 95(11):115304, 2017.

[71] Gary Tuttle, Herbert Kroemer, and John H English. Electron concentrations and mobilities in alsb/inas/alsb quantum wells. *Journal of applied physics*, 65(12):5239–5242, 1989.

[72] Gary Tuttle, Herbert Kroemer, and John H English. Effects of interface layer sequencing on the transport properties of inas/alsb quantum wells: Evidence for antisite donors at the inas/alsb interface. *Journal of Applied Physics*, 67(6):3032–3037, 1990.

[73] LMK Vandersypen, H Bluhm, JS Clarke, AS Dzurak, R Ishihara, A Morello, DJ Reilly, LR Schreiber, and M Veldhorst. Interfacing spin qubits in quantum dots and donors—hot, dense, and coherent. *npj Quantum Information*, 3(1):1–10, 2017.

[74] Veeco systems Inc. *Arsenic Valved Cracker Mark V 500cc Manual*.

[75] Veeco systems Inc. *GEN 10 MBE SYSTEM, User Manual*.

[76] VV Voronkov. Structure of a crystal surface and kossel's model. In *Growth of Crystals*, pages 1–17. Springer, 1976.

[77] X Wallart, J Lastennet, D Vignaud, and F Mollot. Performances and limitations of in as/ in al as metamorphic heterostructures on inp for high mobility devices. *Applied Physics Letters*, 87(4):043504, 2005.

[78] Zhenghan Wang. *Topological quantum computation*. Number 112. American Mathematical Soc., 2010.

[79] Wang, Xueren. Inas/alsb based mid-infrared qcl growth and xrd simulation, 2016.

[80] Bertram Eugene Warren. *X-ray Diffraction*. Courier Corporation, 1990.

[81] XG Xu, J Hu, SP Watkins, N Matine, MW Dvorak, and CR Bolognesi. Metalorganic vapor phase epitaxy of high-quality gaas 0.5 sb 0.5 and its application to heterostructure bipolar transistors. *Applied physics letters*, 74(7):976–978, 1999.

[82] Tobias Zederbauer, Aaron Maxwell Andrews, Don MacFarland, Hermann Detz, Werner Schrenk, and Gottfried Strasser. Incorporation of sb and as in mbe grown gaasxsb1- x layers. *APL Materials*, 5(3):035501, 2017.

APPENDICES

Appendix A

Detailed fabrication process

A.1 Photolithography Recipes

- Single layer Shipley 1805 recipe for Mesa patterning
    1. Bake for 2 minutes at 150 ^oC.
    2. Direct transfer to spin coater and Spin S1805 (Speed 5000 rpm with ramp speed 1000 rpm/sec for 60 seconds).
    3. Bake for 90 seconds at 120 ^oC.
    4. Expose to UV light for 4.5 seconds on Channel 2 with soft contact.
    5. Develop for 45 seconds in MF319.
    6. ASH recipe 8 for 20 seconds.
- Bilayer for large undercut recipe PMGI/S1805 for ohmics and gates.
    1. Bake for 2 minutes at 180 ^oC.
    2. Quickly transfer to spin coater to be hot and Spin PMGI (Speed 5000 rpm with ramp speed 1000 rpm/sec for 60 seconds).
    3. Bake 5 minutes at 180 ^oC.
    4. Spin S1805 while the sample is hot (Speed 5000 rpm with ramp speed 1000 rpm/sec for 60 seconds).
    5. Bake for 90 seconds at 120 ^oC.

6. Expose to UV light for 4.5 seconds on Channel 2 with soft contact.
7. Develop for 45 seconds in MF319. If the undercut is less than 1.5 νm develope for 10 more seconds until it reaches 1.5 νm undercut.
8. ASH recipe 8 for 20 seconds.

A.2 Hall bar fabrication process

For the mesa pattern, single layer of S1805 is spun on the sample as illustrated in the previous section. The photoresist is spread using centrifugal force of the spin coater to achieve a thin uniform layer of the photoresist with a thickness around 600 nm. The samples are exposed to UV light using a Karl Suss MA6 Aligner, it has a resolution down to 1 micron size features. After UV development, the sample is checked by the optical microscope to make sure that the mesa pattern is good and the photoresist is in a good quality and the photoresist is removed from the mesa area. Next step is Ashing, by using recipe 8 from YES CV200-RFS O2 plasma asher, which is 20 seconds in O_2 plasma. Then, a reflow bake is performed at 120 ^oC for 2 minutes, to ensure that there is a good adhesion after ashing. Wet etching for the off-mesa areas is performed to a depth of 180 nm reaching the buffer layer. For our samples, $H_3PO_4 : H_2O_2$ solution is used for wet etching. Thus, the mesa region will be the only conductive area of the sample. The time of wet etching can differ each time, therefore we start with 15 seconds then checking the etching depth with dektak. If the depth is 180 nm or more, there is no need for more etching. If it is less than 180 nm, the etching rate is calculated and etching is performed again for a certain time. The mesa etch solution ratios is shown in table A.1. After checking the depth of etching using dektak, the resist is washed away using acetone and 2-propanol. Then, checking the mesa pattern using optical microscope, to ensure that there is no resist of the sample and the mesas are in a good shape.

The following step is Ohmic contacts. A 10 seconds dip of the sample in hydrofluoric acid (HF) is done, prior to photolithography process, for the native oxide removal and make the surface of the sample chemically suitable for a better photoresist quality and

Mesa etching solution
$H_3PO_4 : H_2O_2$ 38 : 2

Table A.1: Etching solution of InAs samples.

Recessed Ohmics etching solution
$H_3PO_4 : H_2O_2 : H_2O$ 38 : 2 : 120

Table A.2: Recessed Ohmic Etching solution.

adhesion. Bilayer photolithography process is performed according to the details illustrated above. The sample is exposed for 4.5 seconds 25 mW/cm2 of UV at 365nm-405nm with soft contact. The sample is developed in MF-319 developer for around 1.5 minutes and checking the bilayer thickness using optical microscope before proceeding to the next step. To ensure that the sample has large undercut to perform a successful lift-off process after metal deposition. Recessed Ohmic etching is performed before the metal deposition to make direct contact with the 2DEG. For this etching step, the same solution used for mesa will be used but diluted, the details are shown in table A.2. The target of this etching is to make direct contact with the 2DEG. Therefore, the etching must reach the surface of the 2DEG so the depth of etching must be around 25 nm. Another piece of the same growth is used to calculate the etching rate by etching it and measure the depth using dektak. Then, the time needed to etch 25 nm is calculated and the main sample is finally etched for the time calculated. Last step before metal deposition is a 10 seconds dip in HF to remove the native oxide and make a good ohmics contact. The sample is directly transferred to the Intlvac Nanochrome UHV-II system for metal deposition. 20 nm of titanium is deposited first followed by 80 nm of gold at a chamber pressure of 4×10^{-6} Torr. Finally, after metal deposition, PG remover is used to perform lift-off process, in which the sample is placed overnight. This is the end of fabrication process for the un-gated Hall bars.

Appendix B

Magneto-transport Data

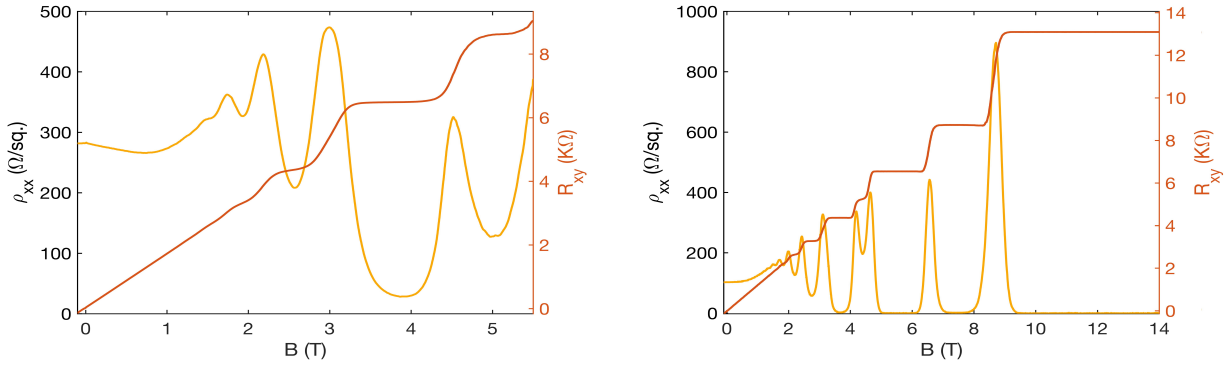

(a) G0600

(b) G0600 at higher magnetic field

Figure B.1: The magneto-transport for G0600 is shown in (a) where the SdH oscillations did not hit zero. Magneto-transport for G0600 at higher magnetic field (b) where the parabolic background in the SdH oscillations has been eliminated and the oscillations hit zero. The oscillations indicate a moderate carrier mobility of 97,000 cm^2/Vs.

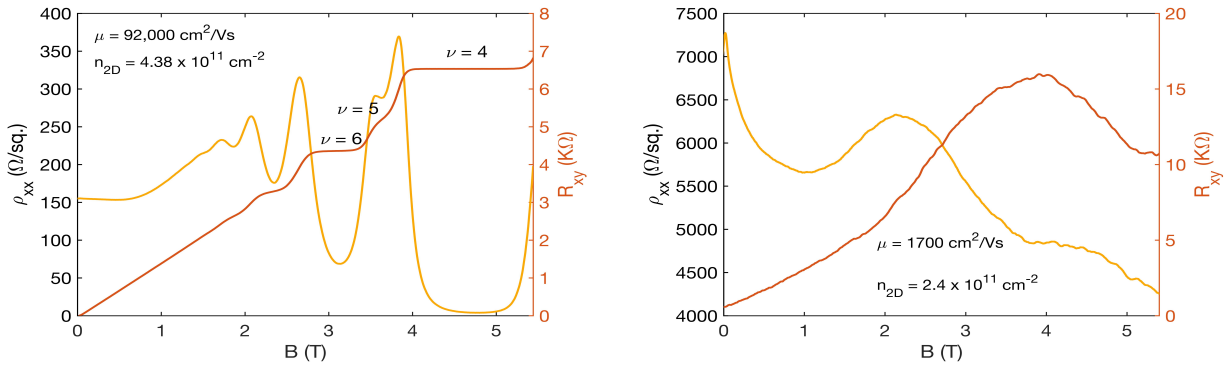

(a) G0679 (b) G0703

Figure B.2: The magneto-transport for G0679 is shown in (a) with mobility 92,000 cm^2/Vs at carrier density 4.38×10^{11} cm^2. Magneto-transport for G0703 is shown in (b) with very low mobility of 1,700 cm^2/Vs at carrier density 2.4×10^{11} cm^2